

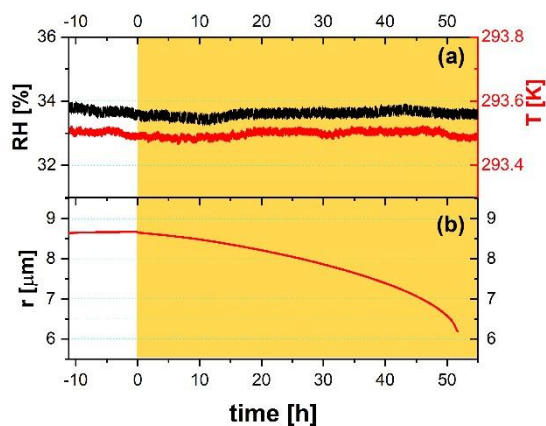
We thank the reviewer for such helpful comments and suggestions of our manuscript. We will answer the questions one by one below and list our planned changes to the manuscript as well.

Major comments:

Line 126-127: Figure 2 shows the data while irradiation, not while the particle is equilibrating. The data for this part of the experiment are shown over a much shorter time than the 10 h stated in the methods section. what is the magnitude of mass loss during the dark equilibration period?

The mass of the particle is quite stable during the dark equilibration period as soon as the RH and T in the trap are stable, since no chemistry happening in the dark. **An example is shown below.** Therefore, we only show a short dark period to indicate that the particle was stable before we turned on the light.

No change to the manuscript.



There are conclusions made in the abstract that did not come across very clearly upon examining the figures and the text. It is important that each major statement on observations in the manuscript is supported by the data analysis in the manuscript. The figures need to be re-made to make conclusions easier to see for connection with the abstract. For example, the conclusion in line 17 was for 10 micron particles over 24 hr, but the modeling results in Figure 13 were for 1 micron to nanometer particles, and their mass loss rate is different. Also, data in Figure 6 show less than 80% mass loss.

We thank the reviewer for pointing out that the reader needs to be more clearly informed which results are experimental observations and which are model results.

Fig. 2 shows that a single, levitated particle with a 12 μm radius loses about 80% of its mass to the gas-phase under the conditions of this particular experiment.

The purpose of Fig. 6 is to show that the PRAD model is able to simulate such experiments reasonably well. We show only the mass loss of the first 40 % here as eventually crystallization of iron citrate occurs within the particle, which is not treated in our model. However, we agree with the reviewer that it may help the reader to see the data of the subsequent mass loss to better understand our statement in lines 302-304:

“However, the model is not able to capture the full degree of acceleration of the degradation rate, as it does not attempt to include the complete multi-generational oxidation chemistry at the level of individual components after initial radical production.”

The reviewer is correct, that the model results of Fig. 13 cannot be directly compared to the experimental data shown for example in Fig. 2 as the irradiation conditions and the particles size is quite different. For estimating the effect on atmospheric aerosol particles, we developed the PRAD model.

Planned changes for a revised manuscript:

To avoid confusion between experimental data and modeling predictions, we will shift lines 17 to 20 of the abstract to directly follow the list of experimental techniques and only then introduces the PRAD model in the abstract so that there is a clear separation between experimental results and modeling predictions.

The figure below shows how the experiments of Fig. 6 evolve subsequently. We will put this figure in the appendix of the paper. And a comparison with PRAD modeling is shown in the same figure as well.

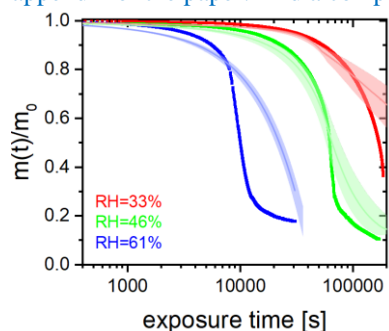


Figure A3. $\text{Fe}^{\text{III}}(\text{Cit})/\text{CA}$ (molar ratio 0.05) particle mass change with irradiation (log scale) at different RH: 33% (red), 46% (green), and 61% (blue). The irradiation wavelength was 375 nm, its intensity was 0.25 W cm^{-2} , and the experimental temperature was 293.5 K. Thick lines are EDB experimental data. Thin lines are PRAD model outputs (with $\pm 2\%$ RH uncertainty shown as shaded area).

In the abstract, the statement, “The PRAD model was tuned to reproduce all experimental results”: The mass loss data in Figure 2 does not show modeling results specific to the experimental setting to support this sentence. Also, model results in figures 7 and 11 are way off from the experimental data. So, it is not clear how this model reproduced the experimental data.

Planned changes for a revised manuscript (changes in bold):

We will rephrase the sentences in the abstract and add a sentence: “The PRAD model was tuned to **simultaneously** reproduce all experimental results as closely as possible and captured the essential chemistry and transport during irradiation. In particular, the photolysis rate of Fe^{III} , the re-oxidation rate of Fe^{II} , HO_2 production, and the diffusivity of O_2 in aqueous $\text{Fe}^{\text{III}}(\text{Cit})/\text{CA}$ system as function of relative humidity and $\text{Fe}^{\text{III}}(\text{Cit})/\text{CA}$ molar ratio could be constrained. **This led to satisfactory agreement within model uncertainty for most, but not all experiments performed.**”

It is not clear how the molar ratio of $\text{Fe}(\text{III})(\text{Cit})$ to citric acid (CA) was controlled. The manuscript shows that it was not fixed in the experiments, and the chemical composition was calculated. Section 2.1 does not describe solution preparation from which aqueous droplets were taken for the EDB measurements. The caption of the figures reported 0.01, 0.05, 0.07, and 1. How does these calculated molar ratios correlate with the solution prepared in the lab?

We agree with the reviewer and wish to make it more clear which mole ratio was used for each experiment and each PRAD model run. To summarize, the initial mole ratio was 0.05 for all EDB experiments shown in the manuscript. For all STXM/NEXAFS experiments, the initial mole ratio was 1.0. For all CWFT experiments, the initial mole ratio was 0.07. The PRAD model of these experiments used the same initial mole ratio, respectively. We performed one additional PRAD model simulation (Fig. 13) using a mole ratio of 0.01. **We have added an addition section (new section 2.1) that details our solution preparation:**

Citric acid ($\geq 99.5\%$) and Iron(III) citrate tribasic monohydrate (18–20% Fe basis) were purchased from Sigma-Aldrich. Iron(II) citrate ($\text{Fe}^{\text{II}}(\text{HCit})$) was purchased from Dr. Paul Lohmann GmbH KG. Dilute aqueous solutions of $\text{Fe}^{\text{III}}(\text{Cit})/\text{citric acid}$ and $\text{Fe}^{\text{II}}(\text{HCit})/\text{citric acid}$ were made in ultrapure water ($18 \text{ M } \Omega \text{ cm}^{-1}$, MilliQ). Since $\text{Fe}^{\text{III}}(\text{Cit})$ only dissolves slowly in water, citric acid solution with $\text{Fe}^{\text{III}}(\text{Cit})$ crystals inside has to be put in an ultrasonic bath for at least 24 hours, the same dissolving procedure was also applied to the $\text{Fe}^{\text{II}}(\text{HCit})$ powders. Note that all the procedures were done under red light illumination because $\text{Fe}^{\text{III}}(\text{Cit})$ is light sensitive. Molar ratio between $\text{Fe}^{\text{III}}(\text{Cit})$ and CA was different for each experimental methods used in this study. For EDB, STXM/NEXAFS and CWFT experiments, stock solutions were prepared with molar ratios of 0.05, 1.0 and 0.07, respectively.

What is the pH of the solution prepared in the lab and that calculated from the chemical composition model? What is the effect of pH on mass loss? Photochemical degradation of iron complexes is pH dependent, not only wavelength dependent. This is a major issue that is not addressed in the current version of the manuscript.

We thank the reviewer for pointing out and agree strongly with her/him about the importance of pH.

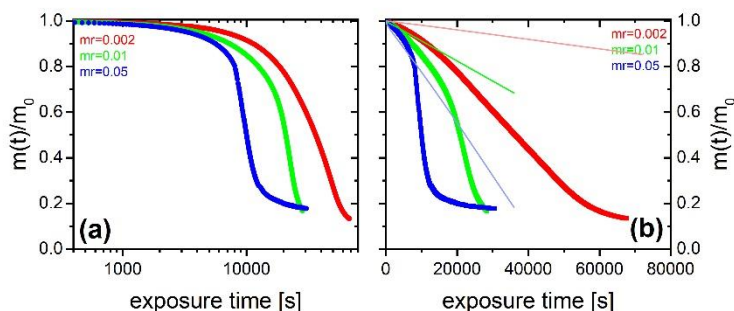
For all three kinds of experiments, CA is highly concentrated in the aqueous system at the relative humidities considered. Its presence dominates the pH (to values in the range of 1 – 2), i.e. the conditions considered in the paper are always acidic. We checked on pH changes predicted by the PRAD model, as it treats the relevant equilibria. According to model outputs, the pH value changes less than 5% during the whole photochemical processes under constant RH.

Planned changes for a revised manuscript (changes in bold):

We will add this clarification to the section of the PRAD model.

There was no experimental studies looking at the extent of mass loss as a function of molar ratio, as there was for particle radius and %RH (e.g., figure 13).

We did the experiments to look at the effect of molar ratio (thick lines), and compare the data with PRAD model (thin lines). However, the data was not taken into account when we were optimizing the model.



In addition, CWFT experiments were performed as a function of mole ratio and are included in our another manuscript, showing an increasing HO₂ production with the molar ratio of Fe^{III}(Cit) to CA, which is captured by PRAD model (Alpert et al., 2020).

Alpert, P. A., Dou, J., Corral Arroyo, P., Schneider, F., Xto, J., Luo, B., Peter, T., Huthwelker, T., Borca, C. N., Henzler, K. D., Herrmann, H., Raabe, J., Watts, B., Krieger, U. K., and Ammann, M.: Anoxic aerosol particles leads to preserved radicals, under review of Nature Communication, 2020.

Figure 10: per the mechanism in Figure 1, and the abstract line 4,5 “In the presence of O₂, ensuing radical chemistry leads to further decarboxylation, and the production of .OH, HO₂, peroxides, and oxygenated volatile organic compounds, contributing to particle mass loss”, I expected the opposite result for the ‘mass remaining’ data in the right axis: that the mass remaining for the particle recovered in O₂ for 45 min is lower than irradiating fresh particle under N₂ since the photolysis and loss of CO₂ is driven by the chemistry of dissolved O₂. I did not find an explanation in the text for this part of the figure.

We think the reviewer misunderstood Fig. 10. Fig. 9 is intended to illustrate the experimental procedure. We agree with the reviewer that the uptake of O₂ leads to further oxidation and thus more mass loss. However, both data sets (black and red) shown in Fig. 10 are mass loss due to photochemistry in N₂. The black one is for the irradiation of fresh particle, and the red one is for another irradiation of the particle after recovery in O₂ in the dark for 45 min, which shows less mass loss due to less photochemically reactive Fe(III) contained in the particle than it initially had.

Planned changes for a revised manuscript (changes in bold):

We need to stress stronger that the data shown in Fig. 10 are due to loss in a nitrogen atmosphere where only the decarboxylation is occurring with no further chemistry. We will rephrase the corresponding section.

Minor comments:

Line 418: The reference Duo et al 2020 is not published. The sentence citing this reference does not refer to unknown information. There are book chapters and numerous review articles on this topic, which should be cited.

We thank the reviewer for the suggestion, and change the reference to:

George, C., D'Anna, B., Herrmann, H., Weller, C., Vaida, V., Donaldson, D. J., Bartels-Rausch, T., and Ammann, M.: *Emerg-605ing areas in atmospheric photochemistry*, in: *Topics in Current Chemistry*, vol. 339, pp. 1–53, Springer, Berlin, Heidelberg, https://doi.org/10.1007/128_2012_393, 2012.

George, C., Ammann, M., D'Anna, B., Donaldson, D. J., and Nizkorodov, S. A.: *Heterogeneous photochemistry in the atmosphere*, *Chem. Rev.*, 115, 4218–4258, <https://doi.org/10.1021/cr500648z>, 2015.

Figure 2: for consistency with the text, change the y-axis to hours instead of seconds for time since rates and time discussed in the text are expressed in hours.

In the text, we discussed in both seconds and hours.

We change the upper x-axis to hours:

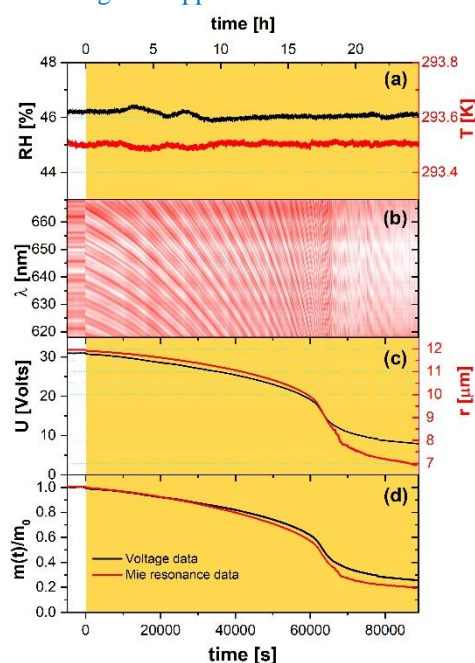


Figure 3: there are two shaded areas in dark and light green, and only the light green is described in the legend. There seems to be a missing compound that describes the dark green shaded area. Also, it is not clear why there are references in the caption? Were some of the spectra shown adapted from these references?

We will change the caption in Fig. 3 to be easier to understand and referenced correctly. First, we clarify that there is only green shading and blue shading. We do not have different shades of green shading.

We will change the caption to be:

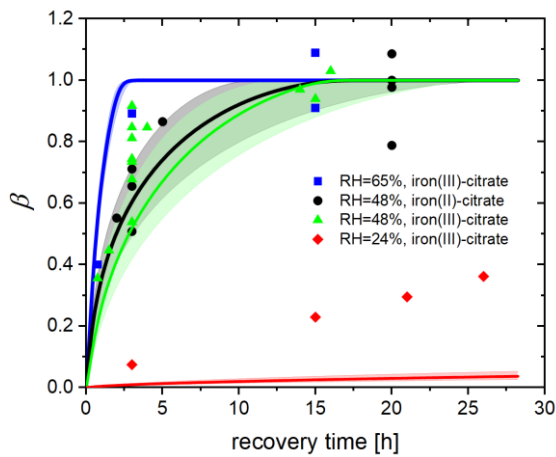
Figure 3. Iron L-edge NEXAFS spectra of Fe^{III}(Cit)/CA particles before and after irradiation with UV light shown as orange and red, respectively. The previously recorded spectrum from mixed xanthan gum (XG) and FeCl₂ particles exposed to ozone is shown as the purple line, and a spectrum from FeCl₂ particles is shown as the blue line (Alpert et al., 2019). FeCl₂ and FeCl₃ spectra from Moffet et al. (2012) are shown as the blue and green shading, respectively. The vertical dashed lines indicate peak X-ray absorption at 707.9 eV shifted to 708.3 eV for Fe^{II} and 709.6 eV shifted to 710.0 eV for Fe^{III}.

Figure 6: the color description for RH does not match the actual colors of the markers. For example: in the figure, data for RH=33% is red, and in the caption it is mentioned as '(black)'. In be, there are markers and lines, for experimental data and model results. Modify the legend to reflect that to avoid confusion which is which.

We thank the reviewer for pointing out this mistake. The color descriptions in the caption have been corrected.

Figure 11: use different marker shapes for different RH, chemicals. Take into account that this figure might be printed on a black and white printer and will be hard to read as is. Why is here more than one data point at t~3 min for the RH = 48%? Same at t~ 15 min and 20 min for 48% and 65% for iron(II) and iron (III) citrate?

We use different marker shapes but also keep different colors to indicate model simulations under corresponding conditions.



The reason for more than one data point is that we repeated the same procedure several times to be confident of the experimental results.

Figure 12: add a legend defining the markers and lines

Adapted accordingly.

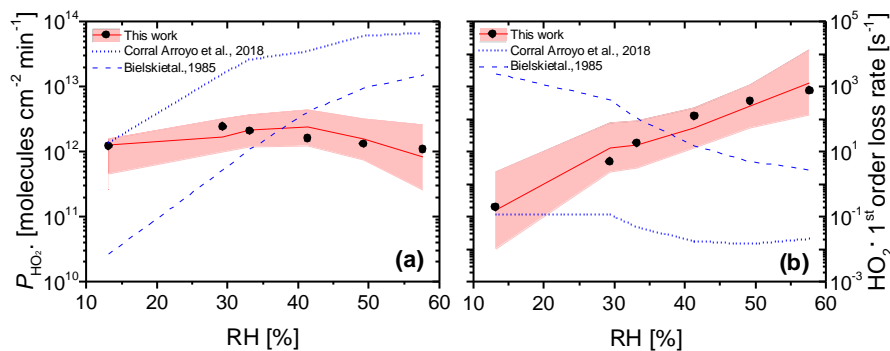
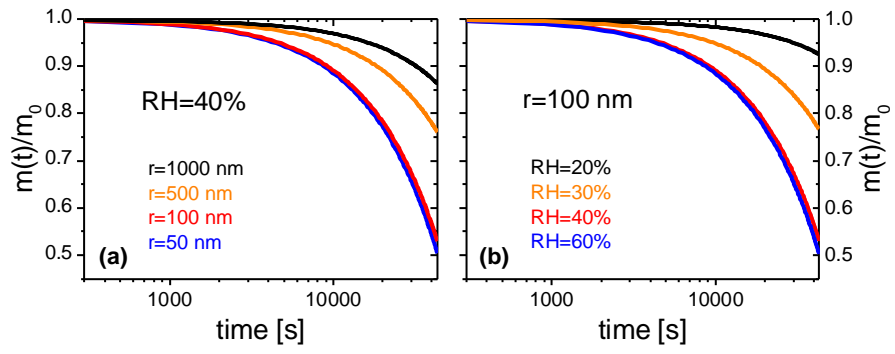


Figure 13: add 'RH=40%' to legend in (a), and '100 nm' to legend in (b).

Adapted accordingly.



1 Reviewer 2 comments and replies

1. PRAD model: The PRAD model appears to be a novel model to describe chemistry within a single droplet. The manuscript would be improved by providing some additional context identifying the distinct aspects of the PRAD model relative to existing models (e.g. KM-GAP, Kinetiscope) which appear to operate under similar principles. In addition, the authors indicate that the model is manually tuned. The authors should clarify how they minimized the possibility of tuning to a local minimum. Moreover, in discussing the number of parameters tuned and the fraction of parameters that are poorly known, the authors should also provide some indication about the sensitivity of the model to these parameters. This is discussed a bit on pages 21 and 22, but additional detail would strengthen the manuscript.

The KM-GAP model (Shiraiwa et al., 2012) and the PRAD model rely on the same kinetic model framework for aerosol surface chemistry and gas-particle interactions (Pöschl et al., 2007). Numerically, the PRAD model uses a Euler forward step method, while KM-Gap solves coupled differential equations. Of course, the PRAD model presented here uses a chemistry scheme targeted for the particular model system of this work. In contrast, Kinetiscope does not integrate sets of coupled differential equations to predict the time history of a chemical system. Instead, it uses a general stochastic algorithm to propagate a reaction. The algorithm executes a random walk through event space, where an event is an individual reaction or diffusion step, rather than physical space, to generate a fully accurate time history of the system (Houle et al., 2015).

We will add to the beginning of section 2.5: “Conceptually, the PRAD model relies on the kinetic model framework for aerosol surface chemistry and gas-particle interactions (Pöschl et al., 2007), similar as for example the KM-GAP model (Shiraiwa et al., 2012). Numerically, the PRAD model uses a Euler forward step method as explained in detail below, while KM-Gap solves coupled differential equations. In passing, there are alternative approaches, for example Kinetiscope (Houle et al., 2015) does not integrate sets of coupled differential equations to predict the time history of a chemical system. Instead, it uses a general stochastic algorithm to propagate a reaction.”

We completely agree with the reviewer that our manual tuning cannot ensure finding the global minimum. To better explain our procedure we will add the following paragraph to the end of section 2.5:

“We restricted our tuning of the parameters to reach satisfactory agreement with all experimental data simultaneously. The equilibrium constants and rate coefficients that were tuned are indicated in Table 2. These parameters were adjusted in a wide and acceptable range until a good representation of our data could be obtained. For example, the fraction of iron(III) in a photoactive complex (equilibrium E5 in Table 2) must have been high enough to reproduce STXM/NEXAFS observations that iron could be reduced to low levels as seen in Fig. 7. In comparison, E7 must have been much lower than E5 so that the amount of iron(III) in a non-photoactive complex was small compared to being in complex with citrate. As another example, oxidation of Fe^{2+} (R6-R8 in Table 2) is fairly well-referenced, and therefore, we adjusted the rate of reaction R9 until the model reoxidation rates matched those observed. Tuning of individual bulk diffusion coefficients for all species was not attempted. Instead, we simplified the representation of diffusion coefficients using a parameterization as function of molar mass described in appendix A1. The 2 constants in Eqn (A8) and 2 constants in Eqn (A3) were tuned resulting in the absolute diffusion coefficients shown in Fig. A1. Henry’s law coefficients for gasses were tuned, however purposefully set at values higher than expected for pure water or highly dilute aqueous solution. This was inspired by previous studies regularly reporting solubility of e.g. O_2 and CO_2 higher in a variety organic liquids than water (Fogg, 1992; Battino et al., 1983).”

As discussed in the answers to question by the other reviewers, we have strengthened the statement that individual parameters which have been tuned should be used with care by adding the following text.

“It is important to note that the result of this tuning does not mean that we found the global minimum in the parameter space, see e.g. (Berkemeier et al., 2017). A thorough search for a global minimum for our model with 16 tuning parameters for chemistry, 4 tuning parameters (and our parameterization) for diffusion and 9 tuning parameters for solubility is computationally very expensive and beyond the scope of this paper. However, for our purpose here, namely modeling typical timescales of photochemical degradation of organic aerosol under atmospheric conditions (see Sec. 3.5) the PRAD model framework should allow sufficiently accurate predictions. In other words, we expect similar mass degradation in atmospheric particles due to the fact that many other relevant iron-carboxylate compounds undergo LMCT similarly as to our model system. Additionally, if a system requires parameter values that significantly different that ours, the PRAD model framework itself may still be valid. Note, that careful evaluation is needed when picking a single parameter of the PRAD model for use in another context. Comparison of the refined model with our experimental data are shown in the next section.”

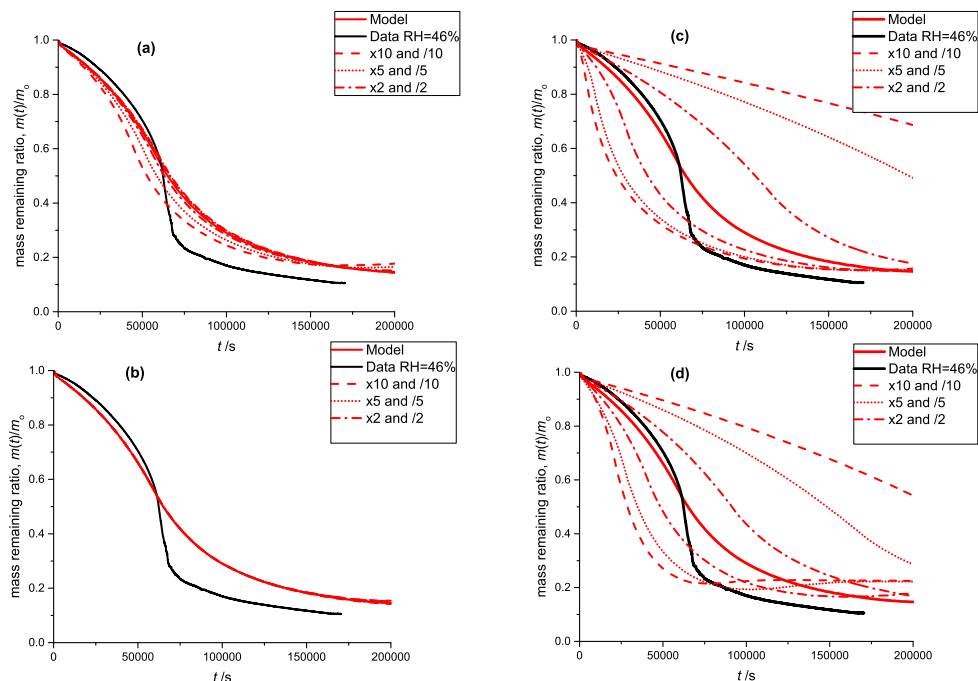


Figure 1. Black: mass remaining data versus time of the photo-degradation experiment discussed in section 3.1; RH 46 %. Red lines: model outputs obtained by varying a single parameter with factors: 10 and 0.1 (dashed), 5 and 0.2 (dotted), 2 and 0.5 (dash-dotted), 1 (solid). In panel (a) equilibrium constant of E8 is varied, in panel (b) equilibrium constant of E5 is varied, panel (c) shows the sensitivity to reaction constant R10 (see Table 2) and panel (d) the sensitivity to oxygen diffusivity (Table 1).

To allow the reader gaining a better feeling for the sensitivity of the model to various parameters we will add an additional appendix showing model results for increasing and decreasing single parameters of the model by up to one order of magnitude:

As discussed in section 2.5 we performed manual tuning of the PRAD model parameters to reach satisfactory agreement with all experimental data simultaneously. To show the sensitivity of the PRAD model results to a few of its parameters Fig. 1 shows again the data of the photocatalytic degradation experiment at 46 % RH described in section 3.1. In addition we show the output of the model as well as model outputs obtained by varying one of the parameters by the indicated factors with keeping all parameters constant. Clearly, the sensitivities of the model output to varying these parameters are very different: while the model output is quite sensitive to varying the rate constant of for the oxidation of $\text{Fe}^{\text{II}}(\text{HCit})$ (R10 in Table 2) as well as to oxygen diffusivity, the sensitivity to the equilibrium constant E8: $\text{Fe}^{2+} + \text{HCit}^{2-} \rightleftharpoons \text{Fe}^{\text{II}}(\text{HCit})$ is significantly smaller and the model is basically insensitive to the equilibrium constant E5: $\text{Fe}^{3+} + \text{Cit}^{3-} \rightleftharpoons \text{Fe}^{\text{III}}(\text{Cit})$. In other words, this experiment alone allows to constrain R10 or oxygen diffusivity as long as the other parameter is known, but does not allow constraining the constants for both equilibria.

2. Page 12, line 247: In this line, the number of molecules is defined as N_n , whereas on the previous page (line 221), the number of moles is defined as N_i . Although the discussion for each revolves around different portions of the particle (n representing the outermost layer; i representing inner layers), the authors should ensure that terms are consistently used throughout the manuscript. Moreover, on page 12, line 270, $n^*\text{Cit}$, $n\text{Cit}$ and $n\text{FeCit}$ do not appear to be defined. Presumably these refer to molarity, in which case should not the appropriate term be c (as defined on page 9, line 205)?

We thank the reviewer for pointing this out. We will define N_n as the moles of molecules in the outermost shell to ensure consistence. We will change 'n*Cit, nCit and nFeCit' to 'N*Cit, NCit and NFeCit' to represent the moles of each species.

3. *Figure 6 caption: The colours listed in the caption do not match those in the figure.*

70 We thank the reviewer for pointing out this mistake. The color descriptions in the caption have been corrected.

4. *Page 17, line 329 ("within about 6 hours"): This is not shown experimentally in Fig. 8. Experimental data at 60 % RH only extend to ~3 h. The model extends to 6 h, but this is not an observation.*

75 We will render this sentence to be more precise: "While particles were observed to re-oxidize to 70 % within 2 hours at 60 % RH and expected to be completely re-oxidized within about 6 hours according to PRAD model simulations, no significant re-oxidation occurred on this timescale for the particles exposed to only 40 % RH."

2 Reviewer 3 comments

1) The PRAD model was developed (presumably) for modeling iron degradation but the framework can be used in other particle/gas reaction systems. Some discussion on how general this model is/can be and which systems it could be successfully applied to would be good. It would also be helpful to add statements about what this model does well, like which parameters are known with the most certainty or which conclusions are the strongest, to help the reader understand the PRAD model's place among other similar models (both those already existing and those yet to be developed).

We are very happy about the reviewer's suggestion that our model framework could be applied in other systems. We will provide a more detailed discussion of this aspect as indicated by the reviewers suggestion. We first note, we have already chosen a system of interest (an organic aerosol particle with a dust inclusion, (see section 3.5, first paragraph) that is more general than $\text{Fe}^{\text{III}}(\text{Cit})$. In order to expand the applicability of this system, we make a simple comparison of mass loss for this system on the order of 20% over 5 hours with ambient mass accumulation measured in the field. As a modest estimate, the results in Fig. 13 of our manuscript indicate this is equal to a mass loss rate of about $0.4 \mu\text{g m}^{-3} (\text{air}) \text{hr}^{-1}$ for an aerosol population with an organic mass of $\sim 10 \mu\text{g m}^{-3} (\text{air})$ undergoing iron-carboxylate photochemistry. This is much larger than observed organic mass accumulation in ambient air masses due to photochemical aging during atmospheric transport at about $0.06 \mu\text{g m}^{-3} (\text{air}) \text{hr}^{-1}$ or $6 \mu\text{g m}^{-3} (\text{air})$ over 4 days (Zaveri et al., 2012; Moffet et al., 2012). This implies, that the mass loss rates are fast enough to affect the balance between aerosol mass accumulation and loss.

The generality of the PRAD model lies in the choice of physical and chemical constants, such as diffusion coefficients, Henry's law constants, reaction rate coefficients and equilibrium constants. If another system were to be investigated, constants could be replaced appropriately to represent decarboxylation, molecular transport and solubility of another iron-carboxylate complex. Another generality is that diffusion coefficients of CO_2 and H_2O are known with great certainty (Dou et al., 2019). Since citric acid is regarded as an proxy for atmospheric secondary organic aerosol compounds in terms of being highly oxygenated and having a representative viscosity, we have some confidence to expand our system to apply to mass loss of atmospheric particles. Finally, we consider iron re-oxidation rates as reliable (Figs. 8, 10 and 11), as this occurs on the same scales as mass loss rates.

Model improvements would involve a representation of peroxy radical chemistry, since photochemical decarboxylation steps of other iron(III)-carboxylate complexes may not immediately result in HO_2 production. By adding more reactions it would make our model more general in its scope, which will be the focus of future work. Additionally, reaction rate coefficients of the two competitive reactions of O_2 with either organic radicals or with iron(II)-carboxylate complexes are not yet well constrained. We have stated at the end of section 2.5 that a different combination of reaction rate coefficients, diffusion coefficients and Henry's Law constants may yield a satisfactory representation of our data. See also Appendix A5. Although, our experimental results and model constrains overall loss rates, it cannot constrain parameters individually.

Finally, we note that the radical production predicted with the PRAD model is reliable. Since re-oxidation and mass loss is tied to the production of radicals, then radical production is also a reliable and generalizable model output. This is a focus of another paper currently in review and will only briefly be mentioned in our revised manuscript.

Changes to the manuscript: We will split section 3.5 into two paragraphs.

We will begin the section by adding the following sentence.

"The PRAD model was developed to also be used in more general particle systems. After establishing . . ."

On line 425 we will add the following discussion:

"To better understand the importance of mass loss in this generalized system, we make a simple and modest comparison of mass loss in Fig. 13 on the order of 20% over 5 hours with ambient mass accumulation measured in the field. Our results are equal to a mass loss rate of about $0.4 \mu\text{g m}^{-3} (\text{air}) \text{hr}^{-1}$ assuming an aerosol population with an organic mass of $\sim 10 \mu\text{g m}^{-3} (\text{air})$ undergoing iron-carboxylate photochemistry. This is much larger than observed organic mass accumulation in ambient air masses due to photochemical aging during atmospheric transport at about $0.06 \mu\text{g m}^{-3} \text{hr}^{-1}$ or $6 \mu\text{g m}^{-3}$ over 4 days (Zaveri et al., 2012; Moffet et al., 2012). This implies, that the mass loss rates are fast enough to affect the balance between aerosol mass accumulation and loss."

And we will add the following sentences to the conclusion section:

"Although a systematic study exploring the whole range of atmospheric conditions was beyond the scope to this work, there are some aspects of the PRAD model and certain parameters that we argue are reliable and pertainate to atmospheric

125 aerosol photochemistry. First, coefficients in the PRAD model framework can be changed to predict mass loss rates of a
 different iron-carboxylate complex system. We are fairly confident that diffusion coefficients of CO₂ and H₂O can be used
 for atmospheric aerosol particles as these were obtained in a more targeted study (Dou et al., 2019). Mass loss rates in general
 are fairly reliable to be used in atmospheric particles as these are linked to photochemical reaction rates which have been
 characterized (Weller et al., 2013, 2014). Finally, reoxidation rates and production of radicals are also reliable, as the system
 is largely reacto-diffusion limited (see appendix A4) and these occur on the same scales as observed mass loss rates. In our
 130 companion paper (Alpert et al., 2020, under review), we show a detailed analysis of radical concentrations in ambient aerosol
 particles for a range of atmospheric conditions and iron content. However, our model still needs major improvements, such as
 including peroxy radical chemistry and better constraints on individual parameters such as diffusion coefficients and reaction
 rate constants. The overall rate may be well-constrained by our experimental studies, however more targeted observations may
 be necessary for an accurate representation of O₂ chemistry, solubility and molecular transport independently of each other
 135 within aerosol particles.”

2) *Some additional discussion about the sensitivity that the manual tuning of certain parameters in the PRAD model has
 would be useful. Quantifying the sensitivity would be excellent but at least something to help the reader gauge the effect that a
 slight mistuning might have. In a similar vein, adding a column to table 1 showing the uncertainties in each of these parameters
 (if they're available) would be good.*

140 This point has been raised by reviewer 2 as well. We refer to our answers related to the sensitivity to those given in reply
 to reviewer 2. As our experiments do not allow to constrain all parameters of the PRAD model individually, we restrain from
 giving uncertainties in Table 1 and Table 2.

3) *Line 322-323 and Figure 7 shows a statistical agreement with 95% confidence between the model and the data, but it is
 just on the edge of significance. Even though a 95% confidence level is commonly used, it is ultimately arbitrary. A sentence
 145 or two giving some extra context or how the estimate could improve would be helpful in making the conclusion (that jcalc is a
 good estimator for jobs) more robust.*

We agree with the reviewer that some context would help explain why we made such an estimate of the photochemical
 reaction rate and help to explain how this could be improved. In Fig. 7 the calculated value of j used in the model yield more
 reduction than observed. This represents a single UV-fiber setup. In Fig. 8, the fiber was setup an addition 2 times, once for
 150 experiments at RH=40% and another time for experiments at RH=50-60%. Still, we see that the reduction of iron very soon
 (minutes) after UV light was switched off is still in agreement with observed values of β . In order to better quantify this
 uncertainty and any possible systematic errors, we should repeat UV-fiber setup procedures and measurements of β , however,
 the time to use the X-ray beam allotted to us was highly limited and our estimated uncertainty was already good enough. As
 recommended by the reviewer, we will add in a few sentences to explain this.

155 *Minor comments*

Line 45: “humic like” should be hyphenated Line 57: “time resolved” should be hyphenated

Agreed and changed

*Line 72: The chemical formula of iron(III) citrate is FeC6H5O7 but the structural formula written shows an incorrect number
 of Carbon and Hydrogen atoms. Please revise the structural formula.*

160 Agreed and changed to Fe^{III}(OOCCH₂)₂C(OH)(COO)

Line 99: reword: “The PRAD model allows to simulate”

Sentence rephrased as: “In addition, we will use the PRAD model to simulate photochemical aging processes under atmo-
 spheric conditions.”

*Line 201: The denominator in the expanded version of equation (4) uses “r” as a subscript, it shows “0.5(rr+1 – ri-1)”
 165 should it read “0.5(ri+1 – ri-1)” instead? Also why use 0.5(ri+1 – ri-1) instead of (ri+1 – ri)?*

We thank the reviewer for noticing, yes, the equation should read:

$$f_i = -4\pi r_i^2 D_1 \left. \frac{dc}{dr} \right|_{r=r_i} = -4\pi r_i^2 D_1 \frac{c_{i+1} - c_i}{0.5(r_{i+1} - r_{i-1})}; \quad \forall i \in \{1, 2, \dots, n-1\}, \quad (1)$$

To represent the **average** distance for molecules to be transported between two adjacent shells we use $0.5(r_{i+1} - r_{i-1})$ instead
 of $(r_{i+1} - r_i)$.

170 *Line 209: Shouldn't the radius should be squared in equation (6) as part of the sphere surface area equation? This continues through equations (8), (9), (13), (14), and (16). A brief clarification would help.*

In the outermost shell n , the flux into the gas phase is given by:

$$f_i = -4\pi r_n^2 D_d \left. \frac{dc}{dr} \right|_{r=r_n} = -4\pi r_n^2 D_g \frac{c_g - c_g^*}{r_n} = -4\pi r_n^2 D_g \frac{p_{\text{partial}} - p_{\text{vapor}}}{r_n RT}; \quad (2)$$

To clarify we will change eq. (6) accordingly.

175 *Line 248: If cn is molar concentration (as defined in line 205), then Nn should be the number of moles, not the number of molecules.*

We thank the reviewer for pointing this out. We will define N_n as the moles of molecules in the outermost shell to ensure consistence.

180 *Line 270: Because concentration was defined as a subscripted "c" (i.e. cn in line 205) replace the $nCit$ values with $cCit$ for consistency.*

We will change n_{Cit}^* , n_{Cit} and n_{FeCit} to N_{Cit}^* , N_{Cit} and N_{FeCit} to represent the moles of each species.

Figure 6: The caption colors do not correspond to the figure colors.

We thank the reviewer for pointing out this mistake. The color descriptions in the caption have been corrected.

185 *Line 304: "The degradation progresses..." should be "The degradation processes..."*

Agreed and changed

3 Reviewer 4 comments

My main critique involves how applicable this system is issues of a global scale, as the paper attempts to address in the conclusions. How important are organic-Fe particles globally? Are they so abundant that they are expected to measurably affect the organic aerosol burden? How representative is the Fe citrate system of globally distributed aerosol iron?

190 In response to the reviewer comments, we would like to include more details in the introduction and discussion section about the global relevance of iron-carboxylate complexes, in general, and the applicability of the specific iron(III)-citrate system to atmospheric iron-carboxylate compounds. First, organic-Fe particles impact many global processes, such as, determining iron solubility in the atmosphere and deposition in the oceans (Hamilton et al., 2019). Second, auto-oxidation of SO₂ is a well-known chemical process in fog and cloud water as the result of the interaction of carboxylates and iron to produce sulfate and impact aerosol inorganic mass (Grgić et al., 1998, 1999; Grgić, 2009). Additionally, iron photochemical cycling produces a significant amount of radicals (Fang et al., 2020) that can subsequently react with other organics in particles, fog droplets and clouds water affecting the formation of aqueous phase secondary organic aerosol (aqSOA) (Bianco et al., 2020). Also, photochemical reactions with iron-organic complexes should not be neglected when considering the loss of (aqSOA) in aerosol particles (Weller et al., 2014; Herrmann et al., 2015). Finally, researchers have only shown recently that soluble iron is largely 200 complexed with carboxylates in ambient aerosol particles (Tapparo et al., 2020; Tao and Murphy, 2019). Iron is certainly abundant in the atmosphere, however, a global estimate and uncertainty of how iron-organic complexes affect the organic aerosol burden has not yet been realized. The first photochemical model of iron carboxylate complexes and organic aerosol mass loss, to our knowledge, is present in our manuscript. We encourage future work to quantify this effect.

Atmospheric iron(III) carboxylate photochemistry has been established as important using a slew of different carboxylate 205 compounds (Weller et al., 2014, 2013; Herrmann et al., 2015). All iron complexes with carboxylates, such as pyruvate, glyoxalate, malonate, oxalate, succinate, tartronate, tartrate and citrate undergo ligand-to-metal charge transfer and decarboxylation (Cieśła et al., 2004; Weller et al., 2013, 2014). Furthermore, citric acid is regarded as an excellent proxy for atmospheric secondary organic aerosol compound in terms of being highly oxygenated and having a similar viscosity (Lienhard et al., 2015; Reid et al., 2018). Therefore, it is highly justified to claim that iron(III)-citrate photochemistry is a system relevant to 210 atmospheric aerosol particles and cloud droplets.

We will include this discussion on lines 73-76 with the following text.

“Our Fe^{III}(Cit) system undergoes LMCT reaction in the same way as countless other iron(III)-carboxylate compounds (Cieśła et al., 2004; Weller et al., 2013, 2014). Its photochemical reaction scheme is well established. . . water diffusivity and viscosity being well studied (Lienhard et al., 2012, 2014, 2015; Song et al., 2016). For these reasons, it is a valid and reliable 215 proxy for atmospheric iron-carboxylate photochemical processes.”

On line 44, we will also discuss the global importance more effectively.

“Quantifying iron atmospheric processing and solubility is of global importance, especially for nutrient input into the World's oceans (Hamilton et al., 2019; Kanakidou et al., 2018). Heterogeneous chemistry involving particulate iron and SO₂ can result in sulfate formation and increase aerosol loading (Grgić et al., 1998, 1999; Grgić, 2009). Additionally, iron photochemical 220 processing in aerosol particles, fog droplets and cloud water is an important radical source (Bianco et al., 2020; Abida et al., 2012) and sink for organic compounds (Weller et al., 2014, 2013; Herrmann et al., 2015).” And we will add to the end of the paragraph: “Field studies have confirmed that soluble iron is mostly in complexes with carboxylate functions (Tapparo et al., 2020; Tao and Murphy, 2019).”

My specific comments are as follows:

225 *Line 20: I suggest adding a brief description of the type of parameters used to “tune” the model.*

This comment was also asked by other reviewers, and as a result we have added new text to detail the tuning of the PRAD model. Briefly, we marked the equilibrium constants and rate coefficients which were tuned in Table 2 and added detailed text on tuning parameters at the end of section 2.5. Briefly, all parameters were adjusted in a wide and acceptable range until a good representation of our data could be obtained. Tuning of individual bulk diffusion coefficients for all species was highly 230 impractical and therefore a parameterization was made as a function of molar mass in appendix A1. Parameterization constants were tuned resulting in the absolute diffusion coefficients shown in Fig. A1. Henry's law coefficients for gasses were tuned, however purposefully set at values higher than expected for pure water or highly dilute aqueous solution. This was inspired by

previous studies regularly reporting solubility of e.g. O₂ and CO₂ higher in a variety organic liquids than water (Fogg, 1992; Battino et al., 1983).

235 *Line 119: It is stated that refractive index is assumed not to change. Shouldn't the refractive index change with the amount of water on the particle? If the RH changes, so will the refractive index. Was this accounted for? Refractive indices for both dry and aqueous phases should be available and used to show this is a good assumption. If its not a good assumption, how might it affect results and conclusions?*

240 We completely agree with the reviewer that any compositional change will lead to a change in the refractive index. However note, that all our EDB experiments have been at constant RH and temperature, so that compositional change occurs through the photochemical reactions. The data shown in Fig. 2(d) allow us to observe this effect. If density and refractive index of the particle would indeed stay constant during photochemistry, the mass to initial mass ratio obtained by the mass measurement (compensation of gravitational force by the DC-voltage) should agree with the one obtained from sizing. Up to a mass loss of about 20% this seems to be an excellent approximation as the two curves almost overlap. Later they deviate from each other with progressing chemical evolution, indicative of a change in density and refractive index. This means that initially the refractive index and density is strongly dominated by that of the major compound, citric acid. Therefore, we restrict ourselves to the initial mass loss (about 20%, when comparing model simulations and experiment later, cp. Fig. 6 and corresponding discussion.

245 *Line 125: Molar absorptivities are stated, and will affect reaction rates. How likely is it for side products to be formed that have different optical properties?*

250 We agree with the reviewer that the side products participating in the photochemistry (given as R10 to R14 in Table 2) will have different molar absorptivities or absorption cross sections. As can be seen in the Table 2 we take those as unknown tuning parameters. At least partly, these products may be responsible for the observed acceleration of the photochemical degradation. However, as our chemical scheme neglects other products like peroxy radicals and we do not have any detailed information on these compounds but rather treat them in a lumped manner, we cannot deduce any reliable cross sections for these compounds.

255 *Line 126: I find the term "O2 gas phase" and "oxygen atmosphere" ambiguous and confusing. Are these atmospheres of pure O2? I think it would be best to spell this out.*

Yes, they both refer to pure O₂. To avoid confusion we will write "pure O₂ gas phase" in the revised manuscript.

Line 190: Change "devides" to "divides"

260 Typo corrected

Line 329: Change "dryer" to "drier"

Typo corrected

265 *Figure13: How representative are these sizes of Fe containing particles? Also, if it is dust, how applicable are the results obtained on the iron citrate system which is homogeneously mixed and all soluble? Also, panel B is for a 200 nm diameter particle. Why not increase the particle size for a more reasonable Fe containing particle size?*

We believe to cover the important size range in Fig. 13(a) for iron containing particles (100 nm to 2 μm), see Moffet et al. (2012). While larger particles may contain a larger fraction of iron, there is clear evidence that particles of 200 nm size contain iron. Larger particles will need longer times for reaching the same relative mass loss compared to smaller particles, but panel (b) is meant to illustrate the humidity dependence.

270 *Line 425: How applicable are the EDM experiments to smaller particles? Is it possible to have a size dependent photolysis rate for reasons beyond that described in the PRAD model? What about small particle optical effects?*

The reviewer raises an interesting question. For example nano-focusing could conceptually change photochemical rates. We were not able to study such effects in our setup and could only speculate here. However, taking all other uncertainties into account we are convinced that such effects are of secondary importance. But we agree with the reviewer that experiments looking into such effects are desirable to be performed in the future.

References

- Abida, O., Kolar, M., Jirkovsky, J., and Mailhot, G.: Degradation of 4-chlorophenol in aqueous solution photoinduced by Fe(III)–citrate complex, *Photochem. Photobiol. Sci.*, 11, 794–802, <https://doi.org/10.1039/c2pp05358f>, 2012.
- 280 Alpert, P. A., Dou, J., Corral Arroyo, P., Schneider, F., Xto, J., Luo, B., Peter, T., Huthwelker, T., Borca, C. N., Henzler, K. D., Herrmann, H., Raabe, J., Watts, B., Krieger, U. K., and Ammann, M.: ~~Anoxic aerosol particles leads to preserved radicals~~ [Photolytic radical persistence due to anoxia in viscous Aerosol particles](#), in preparation for *Nature Nat. Commun.*, 2020, under review.
- Battino, R., Rettich, T. R., and Tominaga, T.: The Solubility of Oxygen and Ozone in Liquids, *Journal of Physical and Chemical Reference Data*, 12, 163–178, <https://doi.org/10.1063/1.555680>, <https://doi.org/10.1063/1.555680>, 1983.
- 285 Berkemeier, T., Ammann, M., Krieger, U. K., Peter, T., Spichtinger, P., Pöschl, U., Shiraiwa, M., and Huisman, A. J.: Technical note: Monte Carlo genetic algorithm (MCGA) for model analysis of multiphase chemical kinetics to determine transport and reaction rate coefficients using multiple experimental data sets, *Atmospheric Chemistry and Physics*, 17, 8021–8029, <https://doi.org/10.5194/acp-17-8021-2017>, <https://acp.copernicus.org/articles/17/8021/2017/>, 2017.
- Bianco, A., Passananti, M., Brigante, M., and Mailhot, G.: Photochemistry of the Cloud Aqueous Phase: A Review, *Molecules*, 25, 423, <https://doi.org/10.3390/molecules25020423>, 2020.
- 290 Cieśla, P., Kocot, P., Mytych, P., and Stasicka, Z.: Homogeneous photocatalysis by transition metal complexes in the environment, *J. Mol. Catal. A-Chem.*, 224, 17–33, <https://doi.org/10.1016/j.molcata.2004.08.043>, 2004.
- Dou, J., Luo, B., Peter, T., Alpert, P. A., Corral Arroyo, P., Ammann, M., and Krieger, U. K.: Carbon dioxide diffusivity in single, levitated organic aerosol particles, *J. Phys. Chem. Lett.*, 10, 4484–4489, <https://doi.org/10.1021/acs.jpcclett.9b01389>, 2019.
- Fang, T., Lakey, P. S. J., Rivera-Rios, J. C., Keutsch, F. N., and Shiraiwa, M.: Aqueous-Phase Decomposition of Isoprene Hydroxy Hydroperoxide and Hydroxyl Radical Formation by Fenton-like Reactions with Iron Ions, *J. Phys. Chem. A*, 124, 5230–5236, <https://doi.org/10.1021/acs.jpca.0c02094>, 2020.
- 295 Fogg, P. G. T., ed.: *Carbon Dioxide in Non-Aqueous Solvents At Pressures Less Than 200 KPa*, vol. 50, Pergamon Press, Oxford, <https://doi.org/10.1016/C2009-0-00247-5>, 1992.
- Grgič, I.: *Metals in Aerosols*, chap. 5, pp. 117–139, John Wiley & Sons, Ltd, <https://doi.org/10.1002/9781444305388.ch5>, 2009.
- 300 Grgič, I., Dovžan, A., Berčič, G., and Hudnik, V.: The effect of atmospheric organic compounds on the Fe-catalyzed S(IV) autoxidation in aqueous solution, *J. Atmos. Chem.*, 29, 315–337, <https://doi.org/10.1023/A:1005918912994>, 1998.
- Grgič, I., Poznič, M., and Bizjak, M.: S(IV) autoxidation in atmospheric liquid water: The role of Fe(II) and the effect of oxalate, *J. Atmos. Chem.*, 33, 89–102, <https://doi.org/10.1023/A:1006141913681>, 1999.
- Hamilton, D. S., Scanza, R. A., Feng, Y., Guinness, J., Kok, J. F., Li, L., Liu, X., Rathod, S. D., Wan, J. S., Wu, M., and Mahowald, N. M.: Improved methodologies for Earth system modelling of atmospheric soluble iron and observation comparisons using the Mechanism of Intermediate complexity for Modelling Iron (MIMI v1.0), *Geosci. Model Dev.*, 12, 383–3862, <https://doi.org/10.5194/gmd-12-3835-2019>, 2019.
- 305 Herrmann, H., Schaefer, T., Tilgner, A., Styler, S. A., Weller, C., Teich, M., and Otto, T.: Tropospheric Aqueous-Phase Chemistry: Kinetics, Mechanisms, and Its Coupling to a Changing Gas Phase, *Chem. Rev.*, 115, 4259–4334, <https://doi.org/10.1021/cr500447k>, 2015.
- 310 Houle, F. A., Hinsberg, W. D., and Wilson, K. R.: Oxidation of a model alkane aerosol by OH radical: the emergent nature of reactive uptake, *Phys. Chem. Chem. Phys.*, 17, 4412–4423, <https://doi.org/10.1039/C4CP05093B>, 2015.
- Kanakidou, M., Myriokefalitakis, S., and Tsigaridis, K.: Aerosols in atmospheric chemistry and biogeochemical cycles of nutrients, *Environ. Res. Lett.*, 13, 063 004, <https://doi.org/10.1088/1748-9326/aabccb>, 2018.
- Lienhard, D. M., Bones, D. L., Zuend, A., Krieger, U. K., Reid, J. P., and Peter, T.: Measurements of thermodynamic and optical properties of selected aqueous organic and organic-inorganic mixtures of atmospheric relevance, *J. Phys. Chem. A*, 116, 9954–9968, <https://doi.org/10.1021/jp3055872>, 2012.
- 315 Lienhard, D. M., Huisman, A. J., Bones, D. L., Te, Y.-F., Luo, B. P., Krieger, U. K., and Reid, J. P.: Retrieving the translational diffusion coefficient of water from experiments on single levitated aerosol droplets, *Phys. Chem. Chem. Phys.*, 16, 16 677–16 683, <https://doi.org/10.1039/C4CP01939C>, 2014.
- 320 Lienhard, D. M., Huisman, A. J., Krieger, U. K., Rudich, Y., Marcolli, C., Luo, B. P., Bones, D. L., Reid, J. P., Lambe, A. T., Canagaratna, M. R., Davidovits, P., Onasch, T. B., Worsnop, D. R., Steimer, S. S., Koop, T., and Peter, T.: Viscous organic aerosol particles in the upper troposphere: diffusivity-controlled water uptake and ice nucleation?, *Atmos. Chem. Phys.*, 15, 13 599–13 613, 2015.
- Moffet, R. C., Furutani, H., Rödel, T. C., Henn, T. R., Sprau, P. O., Laskin, A., Uematsu, M., and Gilles, M. K.: Iron speciation and mixing in single aerosol particles from the Asian continental outflow, *J. Geophys. Res.*, 117, D07 204, <https://doi.org/10.1029/2011JD016746>, 2012.
- 325 Pöschl, U., Rudich, Y., and Ammann, M.: Kinetic model framework for aerosol and cloud surface chemistry and gas-particle interactions - Part 1: General equations, parameters, and terminology, *Atmospheric Chemistry and Physics*, 7, 5989–6023, <https://doi.org/10.5194/acp-7-5989-2007>, <https://acp.copernicus.org/articles/7/5989/2007/>, 2007.

- Reid, J. P., Bertram, A. K., Topping, D. O., Laskin, A., Martin, S. T., Petters, M. D., Pope, F. D., and Rovelli, G.: The viscosity of atmospherically relevant organic particles, *Nat. Commun.*, 9, 956, <https://doi.org/10.1038/s41467-018-03027-z>, 2018.
- 330 Shiraiwa, M., Pfrang, C., Koop, T., and Pöschl, U.: Kinetic multi-layer model of gas-particle interactions in aerosols and clouds (KM-GAP): linking condensation, evaporation and chemical reactions of organics, oxidants and water. *Atmospheric Chemistry and Physics*, 12, 2777–2794, <https://doi.org/10.5194/acp-12-2777-2012>, <https://acp.copernicus.org/articles/12/2777/2012/>, 2012.
- Song, Y. C., Haddrell, A. E., Bzdek, B. R., Reid, J. P., Bannan, T., Topping, D. O., Percival, C., and Cai, C.: Measurements and predictions of binary component aerosol particle viscosity, *J. Phys. Chem. A*, 120, 8123–8137, <https://doi.org/10.1021/acs.jpca.6b07835>, 2016.
- 335 Tao, Y. and Murphy, J. G.: The Mechanisms Responsible for the Interactions among Oxalate, pH, and Fe Dissolution in PM_{2.5}, *ACS Earth Space Chem.*, 3, 2259–2265, <https://doi.org/10.1021/acsearthspacechem.9b00172>, 2019.
- Tapparo, A., Di Marco, V., Badocco, D., D’Aronco, S., Soldà, L., Pastore, P., Mahon, B. M., Kalberer, M., and Giorio, C.: Formation of metal-organic ligand complexes affects solubility of metals in airborne particles at an urban site in the Po valley, *Chemosphere*, 241, 125 025, <https://doi.org/10.1016/j.chemosphere.2019.125025>, 2020.
- 340 Weller, C., Horn, S., and Herrmann, H.: Photolysis of Fe(III) carboxylate complexes: Fe(II) quantum yields and reaction mechanisms, *J. Photochem. Photobiol. A Chem.*, 268, 24–36, <https://doi.org/10.1016/j.jphotochem.2013.06.022>, 2013.
- Weller, C., Tilgner, A., Bräuer, P., and Herrmann, H.: Modeling the impact of iron-carboxylate photochemistry on radical budget and carboxylate degradation in cloud droplets and particles, *Environ. Sci. Technol.*, 48, 5652–5659, <https://doi.org/10.1021/es4056643>, 2014.
- Zaveri, R. A., Shaw, W. J., Cziczo, D. J., Schmid, B., Ferrare, R. A., Alexander, M. L., Alexandrov, M., Alvarez, R. J., Arnott, W. P., Atkinson, D. B., Baidar, S., Banta, R. M., Barnard, J. C., Beranek, J., Berg, L. K., Brechtel, F., Brewer, W. A., Cahill, J. F., Cairns, B., Cappa, C. D., Chand, D., China, S., Comstock, J. M., Dubey, M. K., Easter, R. C., Erickson, M. H., Fast, J. D., Floerchinger, C., Flowers, B. A., Fortner, E., Gaffney, J. S., Gilles, M. K., Gorkowski, K., Gustafson, W. I., Gyawali, M., Hair, J., Hardesty, R. M., Harworth, J. W., Herndon, S., Hiranuma, N., Hostetler, C., Hubbe, J. M., Jayne, J. T., Jeong, H., Jobson, B. T., Kassianov, E. I., Kleinman, L. I., Kluzek, C., Knighton, B., Kolesar, K. R., Kuang, C., Kubátová, A., Langford, A. O., Laskin, A., Laulainen, N., Marchbanks, R. D., Mazzoleni, C., Mei, F., Moffet, R. C., Nelson, D., Obland, M. D., Oetjen, H., Onasch, T. B., Ortega, I., Ottaviani, M., Pekour, M., Prather, K. A., Radney, J. G., Rogers, R. R., Sandberg, S. P., Sedlacek, A., Senff, C. J., Senum, G., Setyan, A., Shilling, J. E., Shrivastava, M., Song, C., Springston, S. R., Subramanian, R., Suski, K., Tomlinson, J., Volkamer, R., Wallace, H. W., Wang, J., Weickmann, A. M., Worsnop, D. R., Yu, X.-Y., Zelenyuk, A., and Zhang, Q.: Overview of the 2010 Carbonaceous Aerosols and Radiative Effects Study (CARES), *Atmos. Chem. Phys.*, 12, 7647–7687, <https://doi.org/10.5194/acp-12-7647-2012>, 2012.

Photochemical degradation of iron(III)-citrate/citric acid aerosol quantified with the combination of three complementary experimental techniques and a kinetic process model

Jing Dou¹, Peter A. Alpert², Pablo Corral Arroyo^{2*}, Beiping Luo¹, Frederic Schneider², Jacinta Xto³, Thomas Huthwelker³, Camelia N. Borca³, Katja D. Henzler³, Jörg Raabe⁴, Benjamin Watts⁴, Hartmut Herrmann⁵, Thomas Peter¹, Markus Ammann², and Ulrich K. Krieger¹

¹Institute for Atmospheric and Climate Science, ETH Zürich, 8092 Zürich, Switzerland

²Laboratory of Environmental Chemistry, Paul Scherrer Institute, 5232 Villigen, Switzerland

³Laboratory for Synchrotron Radiation and Femtochemistry, Paul Scherrer Institute, 5232 Villigen, Switzerland

⁴Laboratory for Synchrotron Radiation-Condensed Matter, Paul Scherrer Institute, 5232 Villigen, Switzerland

⁵Atmospheric Chemistry Department (ACD), Leibniz-Institute for Tropospheric Research (TROPOS), 04318 Leipzig, Germany

* now at: Department of Chemistry and Applied Biosciences, ETH Zürich, 8093 Zürich, Switzerland

Correspondence: Jing Dou (jing.dou@env.ethz.ch) and Ulrich K. Krieger (ulrich.krieger@env.ethz.ch)

Abstract.

Iron(III) carboxylate photochemistry plays an important role in aerosol aging, especially in the lower troposphere. These complexes can absorb light over a broad wavelength range, inducing the reduction of iron(III) and the oxidation of carboxylate ligands. In the presence of O₂, ensuing radical chemistry leads to further decarboxylation, and the production of ·OH, HO₂, peroxides, and oxygenated volatile organic compounds, contributing to particle mass loss. The ·OH, HO₂, and peroxides in turn re-oxidize iron(II) back to iron(III), closing a photocatalytic cycle. This cycle is repeated resulting in continual mass loss due to the release of CO₂ and other volatile compounds. In a cold and/or dry atmosphere, organic aerosol particles tend to attain highly viscous states. While the impact of reduced mobility of aerosol constituents on dark chemical reactions has received substantial attention, studies on the effect of high viscosity on photochemical processes are scarce. Here, we choose iron(III)-citrate (Fe^{III}(Cit)) as a model light absorbing iron carboxylate complex that induces citric acid (CA) degradation to investigate how transport limitations influence photochemical processes. Three complementary experimental approaches were used to investigate kinetic transport limitations. The mass loss of single, levitated particles was measured with an electrodynamic balance, the oxidation state of deposited particles was measured with X-ray spectromicroscopy, and HO₂ radical production and release into the gas phase was observed in coated wall flow tube experiments. **We observed significant photochemical degradation, with up to 80 % mass loss within 24 hours of light exposure. Interestingly, we also observed that mass loss always accelerated during irradiation, resulting in an increase of the mass loss rate by about a factor of 10. When we increased relative humidity, the observed particle mass loss rate also increased. This is consistent with strong kinetic transport limitations for highly viscous particles.** To quantitatively compare these experiments and determine important physical and chemical parameters, a numerical multi-layered photochemical reaction and diffusion (PRAD) model that treats chemical reactions and transport of various species was developed. ~~We observed significant photochemical degradation, with up to 80 % mass~~

loss within 24 hours of light exposure. Interestingly, we also observed that mass loss always accelerated during irradiation, resulting in an increase of the mass loss rate by about a factor of 10. When we increased relative humidity, the observed particle mass loss rate also increased. This is consistent with strong kinetic transport limitations for highly viscous particles. The PRAD model was tuned to [simultaneously reproduce all experimental results as closely as possible](#) and captured the essential chemistry and transport during irradiation. In particular, the photolysis rate of Fe^{III} , the re-oxidation rate of Fe^{II} , HO_2 production, and the diffusivity of O_2 in aqueous $\text{Fe}^{\text{III}}(\text{Cit})/\text{CA}$ system as function of relative humidity and $\text{Fe}^{\text{III}}(\text{Cit})/\text{CA}$ molar ratio could be constrained. [This led to satisfactory agreement within model uncertainty for most, but not all experiments performed.](#) Photochemical degradation under atmospheric conditions predicted by the PRAD model shows that release of CO_2 and re-partitioning of organic compounds to the gas phase may be very significant to accurately predict organic aerosol aging processes.

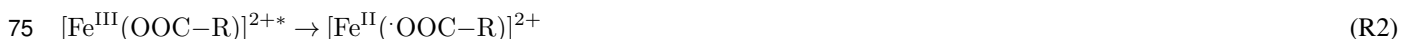
1 Introduction

Photochemistry in the atmosphere (either in the gas phase or in the particle phase) plays an important role in aerosol aging processes. Photochemically produced free radicals in the gas phase (mainly $\cdot\text{OH}$) can be taken up by aerosol particles, inducing multi-phase chemistry. However, uptake is limited by the collision rate and condensed phase molecular transport when diffusion coefficients are sufficiently low, which restricts chemical reactions to the near-surface region of the particle. In contrast, photochemically generated radicals in aerosol particles would be present throughout their bulk due to light penetrating their whole volume. Direct photochemical reaction induced radical production occurs when the energy of light quanta is high enough (mostly the UV part of the solar spectrum) to cause bond cleavage or rearrangement in a molecule. In the lower troposphere where UV light intensity is low, indirect photochemistry initiated by visible radiation may become significant. Important indirect photochemical processes are transition metal complex photochemistry and photosensitized processes (Corral Arroyo et al., 2018; George et al., 2015). This work focuses on iron carboxylate catalyzed photochemistry due to its abundance and reactivity in the atmosphere.

Iron is the most abundant transition metal in the earth's crust. Wind erosion is the main source of iron in the atmosphere, but anthropogenic activities such as industrial processes, traffic and combustion processes can also potentially release iron in particulate form (Deguillaume et al., 2005). Depending on parameters such as temperature, pH value, ionic strength and concentration of involved substances, iron can combine with inorganic or organic ligands to form complexes (Deguillaume et al., 2005; Faust and Hoigné, 1990; Kieber et al., 2005). Iron can be found complexed with low molecular weight inorganic species such as the hydroxide anion (OH^-), sulfate (SO_4^{2-}) and sulfite (SO_3^{2-}) (Brandt and van Eldik, 1995; Hofmann et al., 1991; Weschler et al., 1986). [Quantifying iron atmospheric processing and solubility is of global importance, especially for nutrient input into the World's oceans \(Hamilton et al., 2019; Kanakidou et al., 2018\). Heterogeneous chemistry involving particulate iron and \$\text{SO}_2\$ can result in sulfate formation and increase aerosol loading \(Grgić et al., 1998, 1999; Grgić, 2009\). Additionally, iron photochemical processing in aerosol particles, fog droplets and cloud water is an important radical source \(Bianco et al., 2020; Abida et al., 2012\) and sink for organic compounds \(Weller et al., 2014, 2013; Herrmann et al., 2015\).](#)

Organic compounds are a major component in atmospheric aerosol particles and have received more and more attention as potential ligands for iron(III) complexation. For instance, ~~humic-like~~humic-like substances derived from water soluble organic compounds, have been reported to be strong chelating ligands with iron(III) (Dou et al., 2015; Kieber et al., 2003; Okochi and Brimblecombe, 2002; Willey et al., 2000). Oxalate and other carboxylates have been identified to be important ligands for iron(III) because they are available in sufficient amounts (Chebbi and Carlier, 1996; Kahnt et al., 2014; Kawamura et al., 1985), and the carboxylate groups are acidic enough to dissociate and chelate with iron(III) at atmospheric pH values (Okochi and Brimblecombe, 2002). ~~Field studies have confirmed that soluble iron is mostly in complexes with carboxylate functions~~ (Tapparo et al., 2020; Tao and Murphy, 2019).

In atmospheric aqueous phases, iron normally exists in oxidation states (II) and (III), and they can convert into each other via redox cycling. The ratio between iron(II) and iron(III) in aerosol particles is quite variable, which depends on several factors such as the presence of light, oxidizing compounds, and ligands. For example, ~~Grgić et al. (1999) reported that the concentration ratio of Fe(II) to Fe(III) varied between 0.9 and 3.1 in urban aerosol particles with size range 0.4 – 1.6 μm.~~ ~~iron(III) carboxylate~~Iron(III) carboxylate complexes $[\text{Fe}^{\text{III}}(\text{OOC}-\text{R})]^{2+}$ are well-known photoactive compounds (Wang et al., 2012; Weller et al., 2013, 2014). They can easily get excited by light in the UV-VIS range, inducing ligand-to-metal charge transfer (LMCT) (Cieřla et al., 2004), which is an inner sphere electron transfer (i.e., the electron transfer occurs via a covalently bound bridging ligand) from the carboxylate group to the iron. Investigations using ~~time-resolved~~time-resolved transient spectroscopy reported the formation of long lived radical complexes, $[\text{Fe}^{\text{II}}(\cdot\text{OOC}-\text{R})]^{2+}$, with lifetimes of the order of a millisecond, followed by the dissociation to the organic radical $\text{R}-\text{COO}\cdot$ and an Fe^{II} aquacomplex (Feng et al., 2007; Glebov et al., 2011; Pozdnyakov et al., 2009; Zhang et al., 2009):



$\text{R}-\text{COO}\cdot$ will decarboxylate almost instantaneously ($k_{\text{R3}} \approx 10^9 - 10^{12} \text{ s}^{-1}$) (Abel et al., 2003; Bockman et al., 1997; Hilborn and Pincock, 1991):



The alkyl radical $\text{R}\cdot$ will react rapidly with dissolved O_2 , producing a peroxy radical with $k_{\text{R4}} \approx 2 \times 10^9 \text{ M}^{-1} \text{ s}^{-1}$ (von Sonntag and Schuchmann, 1991):



Subsequent reactions of $R\cdot$ and RO_2 are specific depending on the type of ligand and its substitution.

85 In this work we investigated iron(III)-citrate ($Fe^{III}(OOCCH_2)_3C(OH)[Fe^{III}(OOCCH_2)_2C(OH)(COO)]$), in short $Fe^{III}(Cit)$, as a model species to better understand iron carboxylate photochemistry in atmospheric aerosol particles. Our $Fe^{III}(Cit)$ system undergoes LMCT reaction in the same way as countless other iron(III)-carboxylate compounds (Cieřla et al., 2004; Weller et al., 2013, 2014). Its photochemical reaction scheme is well established in both solution (Abida et al., 2012; Faust and Zepp, 1993; Pozdnyakov et al., 2012) and solid states (Abrahamson et al., 1994). Citric acid (CA) is an established proxy
90 for oxygenated atmospheric organic matter, with its thermodynamic properties, water diffusivity and viscosity being well studied (Lienhard et al., 2012, 2014; Song et al., 2016). For these reasons, it is a valid and reliable proxy for atmospheric iron-carboxylate photochemical processes.

As schematically described in Fig. 1, $Fe^{III}(Cit)$ absorbs light up to 500 nm, inducing LMCT, followed by immediate decarboxylation of the central carboxyl group, since the hydroxyl group adjacent to a carboxyl group facilitates decarboxylation
95 (Weller et al., 2013). In the presence of O_2 , oxidants such as HO_2 and H_2O_2 will be produced, which can oxidize Fe^{II} back to Fe^{III} via Fenton reactions (Fenton, 1894), with additional production of oxidants. Fe^{III} then combines with another citric acid in this aqueous system, closing the photocatalytic cycle, in which iron acts as a catalyst for CA degradation. In addition, the generation of reactive oxygen species (ROS) and peroxy radicals leads to further decarboxylation and more production of oxygenated volatile organic compounds (OVOCs) (e.g., acetone) (Pozdnyakov et al., 2008; Wang et al., 2012). Therefore, this
100 photodegradation process is potentially an important sink of carboxylate groups in the troposphere.

We expect that continuing chemistry subsequent to initial photochemical reaction steps in the aerosol phase will be significantly altered by diffusion limitations when $Fe^{III}(Cit)$ particles mixed with CA attain a high viscosity. As viscosity increases, molecular diffusion coefficients tend to decrease (Koop et al., 2011) and therefore, photochemical cycling will also be slow. Increasing water content is expected when RH increases and will effectively plasticize particles (Koop et al., 2011) leading to
105 a more well mixed conditions and faster photochemical cycling when compared with lower RH. However, these effects have been investigated in dark systems but not in photochemical systems (Berkemeier et al., 2016; Shiraiwa et al., 2011; Shiraiwa and Seinfeld, 2012; Steimer et al., 2015a). In order to better understand this system and how it reacts to RH, we used a triad of photochemical experiments including electrodynamic balance (EDB), scanning transmission X-ray microscopy coupled with near edge absorption fine structure (STXM/NEXAFS) spectroscopy, and a coated wall flow tube (CWFT) to investigate how
110 particle size, mass, and indicators of chemical composition change during photochemical processes. In this work we mostly focus on the humidity dependence of this photochemical degradation, while Alpert et al. (2020, under review) focus on the impacts on ROS species and the fate of free radicals during this photochemical degradation.

To perform quantitative comparison of these experiments and determination of relevant properties, a numerical multi-layered photochemical reaction and diffusion (PRAD) model that treats chemical reactions and transport of various species
115 was developed. The PRAD model allows to simulate photochemical aging processes under atmospheric conditions. In addition, we will use the PRAD model to simulate photochemical aging processes under atmospheric conditions. In the following we briefly discuss our experimental approaches in Sect. 2, and include a detailed explanation of the PRAD model in section 2.5.

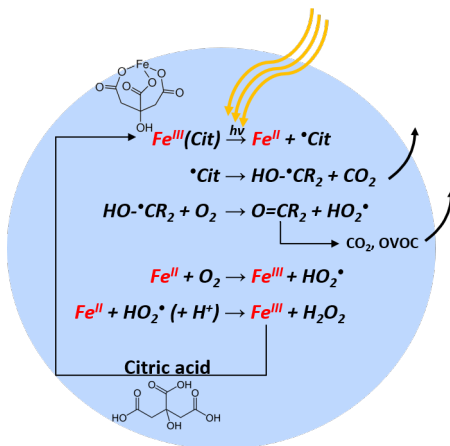


Figure 1. Photocatalytic cycle of $\text{Fe}^{\text{III}}(\text{Cit})$ complex in an aqueous particle containing citric acid, with explicit charge balance given in Table 2. R corresponds to the carboxylate side chain $-\text{CH}_2\text{COO}^-$.

A comparison between experimental results and the PRAD model is presented in Sect. 3. Finally, we discuss the impact and atmospheric importance of kinetic limitations to photochemical degradation in Sect. 4.

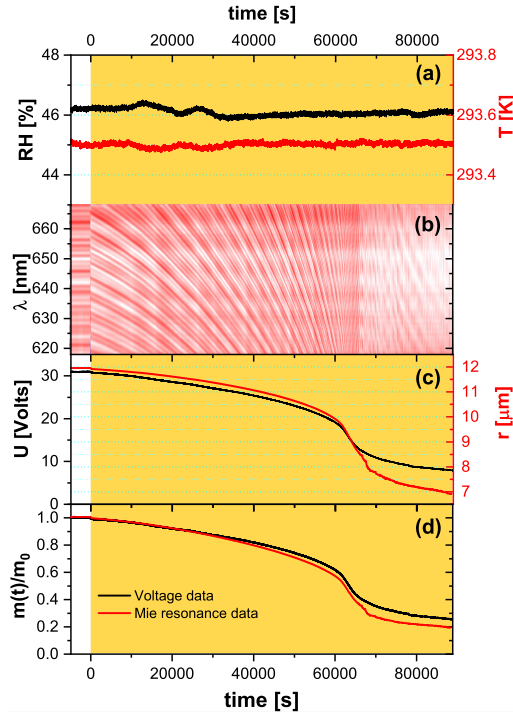
120 2 Methods

2.1 Solution preparation

Citric acid ($\geq 99.5\%$) and Iron(III) citrate tribasic monohydrate (18 – 20 % Fe basis) were purchased from Sigma-Aldrich. Iron(II) citrate ($\text{Fe}^{\text{II}}(\text{HCit})$) was purchased from Dr. Paul Lohmann GmbH KG. Dilute aqueous solutions of $\text{Fe}^{\text{III}}(\text{Cit})/\text{citric}$
 125 acid and $\text{Fe}^{\text{II}}(\text{HCit})/\text{citric}$ acid were made in ultrapure water ($18 \text{ M } \Omega \text{ cm}^{-1}$, MilliQ). Since $\text{Fe}^{\text{III}}(\text{Cit})$ only dissolves slowly in water, citric acid solutions with suspended $\text{Fe}^{\text{III}}(\text{Cit})$ crystals inside were sonicated for at least 24 hours and the same dissolving procedure was also applied to the $\text{Fe}^{\text{II}}(\text{HCit})$ powders. Note, that all the procedures were done under red light illumination because $\text{Fe}^{\text{III}}(\text{Cit})$ is light sensitive. The molar ratio between $\text{Fe}^{\text{III}}(\text{Cit})$ and CA was different for each experimental method used in this study. For EDB, STXM/NEXAFS and CWFT experiments, stock solutions were prepared with molar ratios of
 130 0.05, 1.0 and 0.07, respectively.

2.2 Bulk property measurements by EDB

We used an electrodynamic balance (EDB) to measure the mass loss in single, levitated particles under irradiation. The experimental setup has been described previously (Steimer et al., 2015b). In short, an electrically charged aqueous particle (radius $\sim 10 \mu\text{m}$) is injected into an EDB. The balance is of the double ring design (Davis et al., 1990) with a high AC voltage applied



135 to the two-parallel electrode rings and a DC voltage across hyperbolic endcaps. The DC field compensates the gravitational force of the particle and is used as a measure for the mass of the particle. The EDB is placed in a three wall glass chamber, with a cooling liquid (ethanol) pumped through the two inner walls and an insulation vacuum between two outer walls, to control the temperature (T) at the location where the particle levitates. The relative humidity (RH) within the chamber is regulated by adjusting the ratio of a dry and humidified gas flow through the chamber. In the experiments described in this work, we used a
 140 typical total flow of 40 sccm and set the total pressure inside the cell at 8×10^4 Pa.

The spherical particles were characterized by two Mie resonance spectroscopy based methods: (i) A narrow bandwidth tunable diode laser (TDL, tuning range 765–781 nm) was used to determine the refractive index and radius simultaneously with high precision (Steimer et al., 2015b). (ii) Simultaneously, a broad-band LED centered around 640 nm was used to illuminate the particle. And the backscatter signal from the LED is recorded using a spectrograph with a slow scan back-illuminated
 145 CCD (charge-coupled device) array detector, to follow the resonance wavelength shift of the particle (Zardini et al., 2006). If we assume refractive index stays constant during the experiment, the radius change of a particle is easily calculated from this resonance wavelength shift:

$$\frac{r(t)}{r_0} = \frac{\lambda_0 + \Delta\lambda(t)}{\lambda_0} = 1 + \frac{\Delta\lambda(t)}{\lambda_0}. \quad (1)$$

We illuminated particles to induce photochemical reaction with either a cw diode laser emitting at 375 nm (LuxX 375-20, Omicron Laserage) or a frequency doubled diode laser emitting at 473 nm (gem 473, Laser Quantum). At the wavelength of
 150

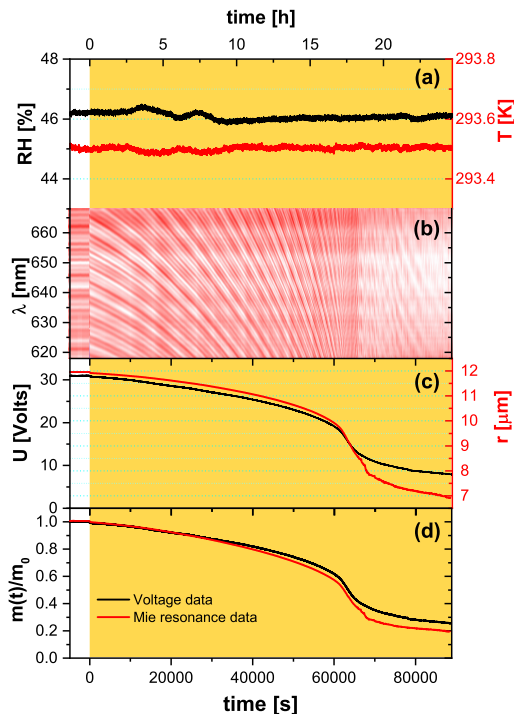


Figure 2. Raw EDB experimental data for a $\text{Fe}^{\text{III}}(\text{Cit})/\text{citric acid}$ (molar ratio of 0.05) particle. (a) Relative humidity (left axis, black) and temperature (right axis, red) of the droplet. (b) Intensity map of low resolution Mie resonance spectra. (c) Black line: DC voltage that compensates gravitational force; Red line: radius of the droplet, with the initial value of the particle radius determined using high resolution Mie resonance spectroscopy (not shown), and the change in radius determined from low resolution Mie resonance data given in (b). (d) Normalized mass remaining ratio deduced from DC voltage (black), and from Mie resonance shift (red) - assuming constant density. Yellow shaded region in panels (a), (c), and (d) indicate the time of laser irradiation with 0.25 W cm^{-2} at 375 nm.

375 and 473 nm, $\text{Fe}^{\text{III}}(\text{Cit})$ is reported to have a molar absorptivity of 796 and $60.7 \text{ M}^{-1}\text{cm}^{-1}$, respectively (Pozdnyakov et al., 2008).

In a typical EDB experiment, we let the particle equilibrate to RH and T in a pure O_2 gas phase for up to 10 hours in the dark before irradiation. Exemplary raw data of an experiment at 46 % RH and 293.5 K is shown in Fig. 2. The measured DC voltage compensating the gravitational force, as well as the radius of the particle deduced from Mie-resonance spectroscopy decreased dramatically during illumination in the first 18 hours, with more than half of the initial mass lost to the gas phase. Note, that the radius and mass loss rates increased as seen in Fig. 2(c). We assumed refractive index and density of the particle did not change upon photochemistry and therefore, the mass loss calculated from the DC voltage could be directly compared with size change by calculating the particle mass remaining ratio,

$$160 \quad \frac{m(t)}{m_0} = \left\{ \frac{r(t)}{r_0} \right\}^3, \quad (2)$$

where m_0 is the particle mass prior to irradiation. Mass loss derived from both ways independently is shown in Fig. 2(d) and reveal that there is a little difference between the mass loss up to $t \approx 65000$ s, corresponding to when $\frac{m(t)}{m_0} < 0.4$. Therefore, the refractive index and density are mostly governed by those of aqueous citric acid up until the half the particle mass is lost. The total mass loss over 24 hours irradiation is more significant and drops by 80 % for the particular experiment shown in
165 Fig. 2. In addition, we observed the mass loss rate initially was ~ 1.3 % h^{-1} and increased to ~ 14 % h^{-1} when 40 % to 60 % of the initial mass was lost. This mass loss acceleration is discussed further in detail with the help of the PRAD model simulations in the section 3.1. At $t \approx 65000$ s, the mass loss slowed down considerably when we observed a distortion in the Mie-resonance pattern (Fig. 2(b) and video in the Supplement). The distortion may be attributable to partial crystallization of iron citrate in the particle, which would explain the slowing photochemical degradation.

170 2.3 Chemical characterization by STXM/NEXAFS

STXM/NEXAFS measurements were performed at the PolLux endstation located at the Swiss Light Source (SLS) to obtain the Fe oxidation state of particles between 0.2-2 μm in diameter (Flechsig et al., 2007; Frommherz et al., 2010; Raabe et al., 2008). Particles containing $\text{Fe}^{\text{III}}(\text{Cit})/\text{CA}$ were nebulized from aqueous solution with a mole ratio between $\text{Fe}^{\text{III}}(\text{Cit}):\text{CA}$ of 1:1. They were dried in air at $RH < 30$ % and impacted onto silicon nitride membranes mounted in portable sample holders. The
175 sample holders were transported to the endstation in an evacuated container and shielded against ambient light. Once there, they were mounted in the PolLux environmental microreactor (Huthwelker et al., 2010), and kept under a total pressure of 1.5×10^4 Pa, $T = 293.5\text{K}$, $RH = 40, 50$ or 60 %, with a controlled gas flow. Further details of sample preparation are provided in previous literature (Alpert et al., 2019; Huthwelker et al., 2010; Steimer et al., 2014). The microreactor was mounted into a vacuum chamber for in situ STXM/NEXAFS analysis. When desired, the microreactor could operate in vacuum conditions
180 without a gas flow. The transmission of X-ray photons through the particles were measured and converted to optical density, $\text{OD} = -\ln(I/I_0)$, where I and I_0 are the transmitted and incident photon flux as a function of X-ray energy. The Fe L-edge absorption was probed over the X-ray energy range of 700 – 735 eV. Figure 3 shows an example of NEXAFS spectra of $\text{Fe}^{\text{III}}(\text{Cit})/\text{CA}$ particles before (orange) and after (red) irradiation with UV light. X-ray energy calibration was consistently performed using FeCl_2 and compared with previous literature for FeCl_2 and FeCl_3 salts (Moffet et al., 2012) and a mixture
185 of xanthan gum and FeCl_2 oxidized by O_3 (Alpert et al., 2019). The peak absorption for iron(II) and iron(III) are at X-ray energies of 708.3 and 710.0 eV. We were capable of resolving peaks separated by 0.4 eV at the Fe L-edge. Ferrous and ferric iron peaks are separated by 1.7 eV and thus, clearly distinguishable. Following a previous procedure (Alpert et al., 2019), we imaged particles at these two energies to determine the OD ratio between them. Then the fraction of Fe^{III} out of total Fe, β , was determined using the parameterization from Moffet et al. (2012). It is important to note that the X-ray energies absorption peaks
190 observed for FeCl_2 and FeCl_3 were identical for FeCl_2 mixed with xanthan gum either unexposed or exposed to O_3 (Alpert et al., 2019). However, we have found that these peaks shifted by about +0.4 eV, possibly due to the strong complexation with CA. Small shifts in energy can occur depending on the chemical environment surrounding Fe atoms (Garvie et al., 1994; Moffet et al., 2012). In agreement with Alpert et al. (2019), the peak absorption energies for our particles were independent of RH from 0 % to 60 % within ± 0.2 eV. When calculating β , we always imaged particles at at 708.3 and 710.0 eV.

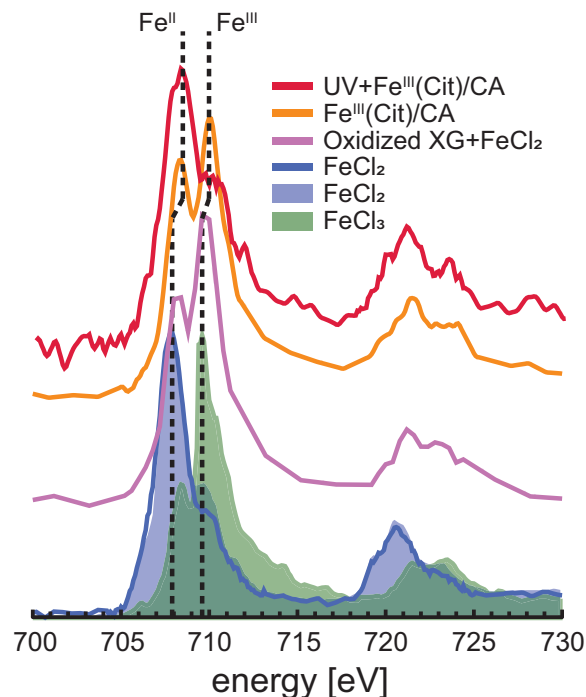


Figure 3. Iron L-edge NEXAFS spectra of $\text{Fe}^{\text{III}}(\text{Cit})/\text{CA}$ particles before and after irradiation with UV light shown as orange and red, respectively. Spectra from mixed xanthan gum (XG) and FeCl_2 particles exposed to ozone and from FeCl_2 particles are purple and blue lines, respectively, in Alpert et al. (2019). FeCl_2 and FeCl_3 are blue and green shading, respectively, in Moffet et al. (2012). The previously recorded spectrum from mixed xanthan gum (XG) and FeCl_2 particles exposed to ozone is shown as the purple line, and a spectrum from FeCl_2 particles is shown as the blue line (Alpert et al., 2019). FeCl_2 and FeCl_3 spectra from Moffet et al. (2012) are shown as the blue and green shading, respectively. The vertical dashed lines indicate peak X-ray absorption at 707.9 shifted to 708.3 eV for Fe^{II} and 709.6 eV shifted to 710.0 eV for Fe^{III} .

195 2.4 HO_2 production determined by CWFT

The HO_2 release upon irradiation of a $\text{Fe}^{\text{III}}(\text{Cit})/\text{CA}$ thin film was measured by scavenging HO_2 with an excess of NO in a coated wall flow tube (CWFT) reactor (Duran glass, inside diameter 1.2 cm, long 50 cm). The film was composed of $\text{Fe}^{\text{III}}(\text{Cit})/\text{CA}$, and deposited inside the tubular glass flow tube with a thickness between 0.15 – 0.2 μm and an error of about 20 %. Details of the film preparation are described previously (Corral Arroyo et al., 2018; González Palacios et al., 200 2016). Seven UV lamps (UV-A range, Philips Cleo Effect) were mounted surrounding the glass reactor held at 298.15 K. The total light output between 300 – 590 nm was 210 W m^{-2} . The flows of N_2 , O_2 , and NO passing through the reactor were controlled. The NO concentration during CWFT photochemical experiments was in excess ($> 10^{13}$ molecules cm^{-3}) to efficiently scavenge 99 % of HO_2 produced by the film. The concentration of NO was tracked by a chemiluminescence detector (Ecophysics CLD 77 AM). In an example CWFT experiment at $RH = 29.3$ %, a clear NO loss was observed when

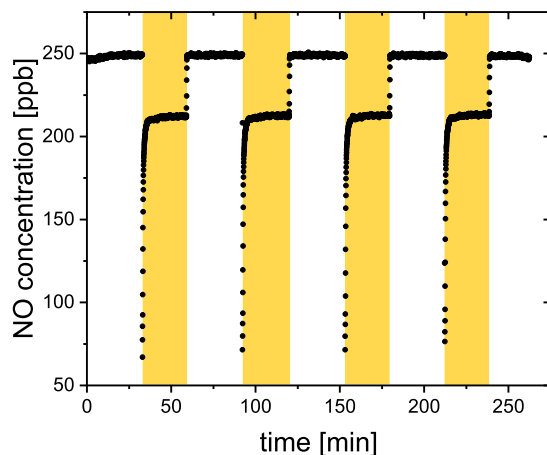


Figure 4. NO concentration raw data from CWFT film containing $\text{Fe}^{\text{III}}(\text{Cit})/\text{CA}$ (molar ratio of 0.07) with lamps on (yellow shaded region) and off at 29.3 % RH and 298.15 K.

205 UV lights were switched on as shown in Fig. 4, which was due to the release of HO_2 radicals into the gas phase and reaction of NO with HO_2 forming NO_2 and $\text{OH}\cdot$. $\text{OH}\cdot$ is then scavenged by NO producing HONO. The production of HONO was routinely checked as described in González Palacios et al. (2016). Therefore, the production rate of HO_2 , P_{HO_2} , was calculated from the loss rate of NO assuming a 2:1 ratio to HO_2 conversion:

$$P_{\text{HO}_2} = \frac{[\text{NO}] \times \text{flow}}{2S_{\text{film}}}, \quad (3)$$

210 where $[\text{NO}]$ is the loss of gas-phase concentration of NO in molecules cm^{-3} , flow is the volumetric gas flow in the CWFT in $\text{cm}^3 \text{s}^{-1}$, and S_{film} is the surface area of the film in cm^2 .

2.5 Development of the PRAD model

We developed a photochemical reaction and diffusion (PRAD) model to interpret our experiments and to understand any feed-backs between transport limitations and photochemistry, especially under low *RH* conditions, corresponding to high viscosity
 215 of the particle phase. The PRAD model consists of two modules: a detailed chemical process module, treating equilibria and chemical reactions, and a transport module handling the physical transport of all species (including diffusion in the aqueous phase as well as gas-particle phase partitioning). Conceptually, the PRAD model relies on the kinetic model framework for aerosol surface chemistry and gas-particle interactions (Pöschl et al., 2007), similar as for example the KM-GAP model (Shiraiwa et al., 2012). Numerically, the PRAD model uses a Euler forward step method as explained in detail below, while
 220 KM-Gap solves coupled differential equations. In passing, there are alternative approaches, for example KineticScope (Houle et al., 2015) does not integrate sets of coupled differential equations to predict the time history of a chemical system. Instead, it uses a general stochastic algorithm to propagate a reaction.

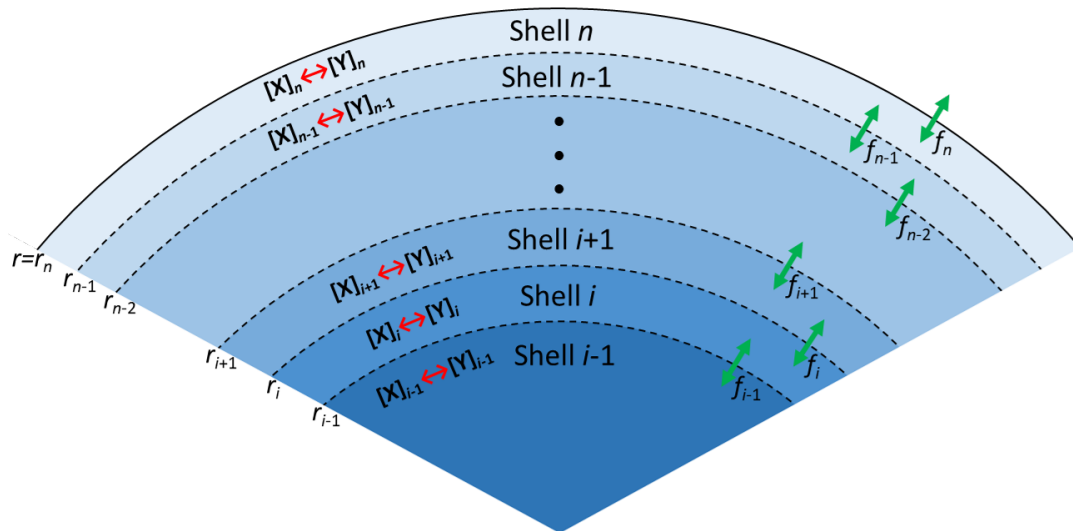


Figure 5. Schematic illustration of the PRAD model. Shells, transport fluxes (green arrows), and chemical processes (red arrows) of each species. The particle is radially symmetric with the surface of the particle marked as r_n .

As illustrated in Fig. 5, the PRAD model divides a spherical droplet into a number of shells, n , which exchange molecules after each chemical time step. Shell thickness and numbers of shells were adjusted to enable the resolution of steep concentration gradients within a reasonable computation time. The volume of each shell was constant instead of the thickness and the shells become thinner and thinner from the center to the surface of the particle. For each shell and at each time step, we first calculated the composition using the thermodynamic equilibria of the $\text{Fe}^{\text{III}}(\text{Cit})/\text{CA}$ system, as listed in Table 2. Then the Newton-Raphson method (Burden and Faires, 2011) was used to calculate the turnover and the concentration of products and reactants over time for the chemical reactions listed also in Table 2 with a fixed time step of 0.2 s. After each time step diffusion of all species between the shells and the evaporation of products (or condensation of the reactant O_2) were computed. The time step, Δt , for physical transport processes was determined dynamically to ensure both numerical stability and computational efficiency.

For each species, the molar flux from shell i to the next shell $i + 1$ was calculated as

$$f_i = -4\pi r_i^2 D_1 \left. \frac{dc}{dr} \right|_{r=r_i} = -4\pi r_i^2 D_1 \frac{c_{i+1} - c_i}{0.5(r_{i+1} - r_{i-1})}; \quad \forall i \in \{1, 2, \dots, n-1\}, \quad (4)$$

where D_1 is the liquid phase diffusion coefficient of the corresponding species. Shell i extends from r_{i-1} to r_i , while shell $i + 1$ extends from r_i to r_{i+1} , with r being the distance from the particle center. In Eq. (4), c is the molar concentration in each shell of the aqueous particle, defined as

$$c_i = \frac{N_i}{V_i}; \quad \forall i \in \{1, 2, \dots, n\}, \quad (5)$$

where N_i is moles of a particular species in shell i , and V_i is the total volume of a shell i .

240 At the outermost shell n , the gas-particle phase partitioning of each species was determined by the modified Raoult's law.

The flux from shell n into the gas phase, f_n , was calculated to be

$$f_i = -4\pi r_n^2 D_g \frac{dc}{dr} \Big|_{r=r_n} = -4\pi r_n^2 D_1 \frac{c_g - c_g^*}{r_n} = -4\pi r_n D_g \frac{p_{\text{partial}} - p_{\text{vapor}}}{RT}; \quad (6)$$

where D_g is the gas phase diffusion coefficient of the corresponding species, and R is the gas constant. p_{partial} is the partial pressure of the species in the gas phase at infinite distance from the particle. Based on Henry's law, vapor pressure of the

245 species p_{vapor} is defined as

$$p_{\text{vapor}} = \frac{c_n}{H}, \quad (7)$$

where c_n is the molar concentration in the outermost shell n , and H is the Henry's law coefficient. Substituting Eq. (7) into Eq. (6) leads to

$$f_n = -4\pi r_n D_g \left(\frac{p_{\text{partial}}}{RT} - \frac{c_n}{HRT} \right). \quad (8)$$

250 We calculated the partial pressure of H_2O from RH , and took the partial pressure of O_2 based on the total pressure and the fraction of O_2 gas flow used in experiments. For other species, p_{partial} is negligible and assumed to be zero. So for all species other than H_2O and O_2 , f_n simplifies to

$$f_n = -4\pi r_n D_g \left(0 - \frac{c_n}{HRT} \right) = 4\pi r_n D_g \frac{c_n}{HRT}. \quad (9)$$

Based on the calculated fluxes, the change in moles, ΔN_i , of each species in Δt was given by

$$255 \Delta N_i = (f_{i-1} - f_i) \Delta t; \quad \forall i \in \{1, 2, \dots, n\}, \quad (10)$$

from which the concentration and corresponding shell thickness using the molar volume of each species were recalculated for the next time step.

The chemical loss rate of O_2 was treated in the liquid phase diffusion module instead of in the chemical module, since the loss can be very fast and its life time can be smaller than 10^{-6} s. If O_2 loss due to reaction was determined in the chemical
260 module, a chemical time step of 10^{-6} s would result in extensive computational time beyond what is reasonable for this study. Therefore, within each liquid phase diffusion time step, in addition to the physical transport, the chemical loss of O_2 molecules was calculated in each shell

$$\frac{dN_i}{dt} = -k_{\text{O}_2} N_i; \quad \forall i \in \{1, 2, \dots, n\}. \quad (11)$$

Integration yields

$$265 N_i = N_i e^{-k_{\text{O}_2} \Delta t}; \quad \forall i \in \{1, 2, \dots, n-1\}, \quad (12)$$

where k_{O_2} is total chemical reaction rate of O_2 . In the outermost shell n , O_2 molar concentration is assumed to be at steady state all times, meaning that the chemical loss of O_2 is always compensated by the condensation of O_2 from the gas phase:

$$-k_{\text{O}_2} N_{n, \text{O}_2} = -4\pi r_n D_g \left(\frac{p_{\text{partial}, \text{O}_2}}{RT} - \frac{c_n}{H_{\text{O}_2} RT} \right). \quad (13)$$

Substituting Eq. (5) in Eq. (13), we calculate the moles of O₂ in this shell, N_{n,O_2} , as

$$270 \quad N_{n,O_2} = \frac{P_{\text{partial},O_2}}{k_{O_2}RT/(4\pi r_n D_g) + 1/(H_{O_2} V_n)}. \quad (14)$$

where H_{O_2} is Henry's law coefficient of O₂.

All iron containing compounds and all free ions are considered not to evaporate from the particle phase. All other species have Henry's law coefficients given in Table 2. If the evaporation rate of some species is fast enough, then their concentration in the outermost shell n can always be at steady state, which means

$$275 \quad f_{n-1} = f_n, \quad (15)$$

that is,

$$-4\pi r_{n-1}^2 D_1 \frac{c_n - c_{n-1}}{0.5(r_n - r_{n-2})} = 4\pi r_n D_g \frac{c_n}{HRT}. \quad (16)$$

From Eq. (16), c_n can be deduced to be

$$c_n = c_{n-1} \frac{1}{1 + 0.5(r_n - r_{n-2})r_n D_g / (HRT r_{n-1}^2 D_1)}. \quad (17)$$

280 And the number of molecules moles of the volatile species in the outermost shell N_n as

$$N_n = c_n V_n. \quad (18)$$

We have parameterized aqueous and gas phase diffusion coefficients, D_1^j and D_g^j , respectively, for all species j given in Appendix A1 and A2. There are several other assumptions and approximations made to adapt this model to the aqueous Fe^{III}(Cit)/CA system:

- 285
1. We set water activity in the particle phase always in equilibrium with the gas phase, since the RH of the gas phase did not change during each experiment.
 2. The bulk accommodation coefficients of all species were assumed to be 1.
 3. Neglecting the influence of Fe^{III}(Cit), the water activity was taken from that of CA (a_w^{CA}), which has been determined from the mass fraction of CA, W_{CA} , by Lienhard et al. (2012)

$$290 \quad a_w^{\text{CA}} = \frac{1 - W_{\text{CA}}}{1 + q \cdot W_{\text{CA}} + r \cdot W_{\text{CA}}^2}, \quad (19)$$

with

$$q = -3.16761 + 0.01939T - 4.02725 \times 10^{-5}T^2, \quad (20)$$

and

$$r = 6.59108 - 0.05294T + 1.06028 \times 10^{-4}T^2, \quad (21)$$

295 The water activity of citrate (a_w^{Cit}) was calculated using the same equation

$$a_w^{\text{Cit}} = \frac{1 - W_{\text{Cit}}}{1 + q \cdot W_{\text{Cit}} + r \cdot W_{\text{Cit}}^2}, \quad (22)$$

where the mass fraction of citrate W_{Cit} was treated in two fractions: citrate without Fe and citrate containing Fe. The water activity of an aqueous 1 M $\text{Fe}^{\text{III}}(\text{Cit})$ solution was determined using a water activity meter (AquaLab water, Model 3B, Decadon Device, USA) at room temperature. We found this water activity corresponds to that of a 0.81 M aqueous CA solution. Therefore, for calculating water activity, all iron containing citrate complexes (no matter Fe^{II} or Fe^{III}) were treated with a reduced concentration: namely with a factor of 0.81 of the corresponding citrate molarity. Hence, the overall amount of citrate was calculated as

$$\mathcal{N}_{\text{Cit}}^* = \mathcal{N}_{\text{Cit}} + 0.81\mathcal{N}_{\text{FeCit}}, \quad (23)$$

accordingly and W_{Cit} was determined following

$$W_{\text{Cit}} = \frac{M_{\text{Cit}} \cdot \mathcal{N}_{\text{Cit}}^*}{M_{\text{Cit}} \cdot \mathcal{N}_{\text{Cit}}^* + M_{\text{H}_2\text{O}} \cdot \mathcal{N}_{\text{H}_2\text{O}}}, \quad (24)$$

where M_{Cit} and $M_{\text{H}_2\text{O}}$ are the molar mass of CA and water, respectively. For other species j , the contribution to the water activity is proportional to their molar volume (MV_j), so that in total,

$$a_w = a_w^{\text{CA}} \times a_w^{\text{Cit}} \times \frac{MV_{\text{H}_2\text{O}}}{MV_{\text{H}_2\text{O}} + \sum_j MV_j}. \quad (25)$$

4. $\text{Fe}^{\text{III}}(\text{Cit})$ photolysis, decarboxylation and oxidation of the alcohol group in presence of O_2 yields the compounds $\text{O}=\text{C}(\text{CH}_2\text{COO})_2^{2-}$ or $\text{O}=\text{C}(\text{CH}_2\text{COOH})_2$, which are C_5 species. We assumed that half of C_5 species undergoes photochemical reactions to produce CO_2 and compounds with 2 – 4 carbon atoms, C_4 , C_3 and C_2 (see reactions R10–R14 shown in Table 2), all of which are capable of being released to the gas phased depending on their solubility.

5. We estimated the quantum yield in reactions R1 and R2 in Table 2, as $\Phi = 1.0$ at $\lambda = 375$ nm and $\Phi = 0.002$ at $\lambda = 473$ nm (Dou et al., 2019), and we parameterized Φ as a function of wavelength, λ :

$$\Phi = \frac{e^{-0.145(\lambda-430)}}{1 + e^{-0.145(\lambda-430)}}. \quad (26)$$

In total, the PRAD model includes 13 equilibria and 17 chemical reactions among 32 species, as well as their condensed phase diffusivities and Henry's law coefficients. Some of these parameters are known from previous studies (see Tables 1 and 2 for references), while others are not known and difficult to estimate. For instance, even though absorption spectra of $\text{Fe}^{\text{III}}(\text{Cit})$ has been measured in aqueous solution (Pozdnyakov et al., 2012), the corresponding quantum yield has not, which leaves the photolysis rate of $\text{Fe}^{\text{III}}(\text{Cit})$, j , unknown. Also, there are no data reported of the diffusivity of O_2 in aqueous citric acid solutions, and the chemical reaction rate of the oxidation of the Fe^{II} -citrate complex by O_2 is quite uncertain (Gonzalez et al., 2017). In order to find the optimal parameter set, we compared experimental data of the three setups taken under well-controlled conditions with model predictions and tuned the unknown parameters manually.

We restricted our tuning of the parameters to reach satisfactory agreement with all experimental data simultaneously. The equilibrium constants and rate coefficients that were tuned are indicated in Table 2 (the sensitivity of the PRAD model results to a few of its parameters is shown in appendix A5). The parameters were adjusted in a wide and acceptable range until a good representation of our data could be obtained. For example, the fraction of iron(III) in a photoactive complex (equilibrium E5 in Table 2) must have been high enough to reproduce STXM/NEXAFS observations that iron could be reduced to low levels as seen in Fig. 7 described later. In comparison, E7 must have been much lower than E5 so that the amount of iron(III) in a non-photoactive complex was small compared to being in complex with citrate. As another example, oxidation of Fe^{2+} (R5-R8 in Table 2) is fairly well-referenced, and therefore, we adjusted the rate of reaction R9 until the model reoxidation rates matched those observed. Tuning of individual bulk diffusion coefficients for all species was not attempted. Instead, we simplified the representation of diffusion coefficients using a parameterization as function of molar mass described in appendix A1. The 2 constants in Eqn (A8) and 2 constants in Eqn (A3) were tuned resulting in the absolute diffusion coefficients shown in Fig. A1. Henry's law coefficients for gasses were tuned, however purposefully set at values higher than expected for pure water or highly dilute aqueous solution. This was inspired by previous studies regularly reporting solubility of, e.g. O_2 and CO_2 higher in a variety organic liquids than water (Fogg, 1992; Battino et al., 1983). It is important to note that the result of this tuning does not mean that we found the global minimum in the parameter space, see e.g. (Berkemeier et al., 2017). A thorough search for a global minimum for our model with 16 tuning parameters for chemistry, 4 tuning parameters (and our parameterization) for diffusion and 9 tuning parameters for solubility is computationally very expensive and beyond the scope of this paper. However, for our purpose here, namely modeling typical timescales of photochemical degradation of organic aerosol under atmospheric conditions (see Sec. 3.5), the PRAD model framework should allow sufficiently accurate predictions. In other words, we expect similar mass degradation in atmospheric particles due to the fact that many other relevant iron-carboxylate compounds undergo LMCT similarly as to our model system (Weller et al., 2013, 2014). Additionally, if a particular system requires parameter values that significantly differ than ours, the PRAD model framework itself should still be valid. Note, that careful evaluation is needed when picking a single parameter of the PRAD model for use in another context. Comparison of the refined model with our experimental data are shown in the next section.

Table 1. Liquid phase diffusivity factors (normalized to water) and Henry’s law coefficients (Sander, 2015) of major species in $\text{Fe}^{\text{III}}(\text{Cit})$ photochemistry system.

number	name	formula	l_i^\ddagger	H_0 (M atm^{-1}) [†]	Q^\ddagger
1	water	H_2O	1	1	1
2	cit total	-	-	-	-
3	ferric (Fe^{III}) total	-	-	-	-
4	ferrous (Fe^{II}) total	-	-	-	-
5	citric acid (CA)	$(\text{CH}_2\text{COOH})_2\text{C}(\text{OH})(\text{COOH})/\text{H}_3\text{Cit}$	1.20×10^{-6}	infinite	10000
6	dihydrogen citrate	$(\text{CH}_2\text{COOH})_2\text{C}(\text{OH})(\text{COO})^-/\text{H}_2\text{Cit}^-$	1.20×10^{-6}	infinite	10000
7	hydrogen citrate	$(\text{CH}_2\text{COOH})\text{C}(\text{OH})(\text{CH}_2\text{COO})(\text{COO})^{2-}/\text{HCit}^{2-}$	1.20×10^{-6}	infinite	10000
8	citrate	$\text{C}(\text{OH})(\text{CH}_2\text{COO})_2(\text{COO})^{3-}/\text{Cit}^{3-}$	1.20×10^{-6}	infinite	10000
9		$\text{Fe}^{\text{III}}(\text{Cit})(\text{OH})^-$	3.92×10^{-7}	infinite	10000
10		$\text{Fe}^{\text{III}}(\text{HCit})^+$	5.04×10^{-7}	infinite	10000
11	ferrous citrate	$\text{Fe}^{\text{II}}(\text{HCit})$	5.04×10^{-7}	infinite	10000
12	ferric citrate	$\text{Fe}^{\text{III}}(\text{Cit})$	5.04×10^{-7}	infinite	10000
13	ferric ion	Fe^{3+}	3.78×10^{-5}	infinite	10000
14		$\text{Fe}^{\text{III}}(\text{OH})^{2+}$	1.18×10^{-5}	infinite	10000
15	ferrous ion	Fe^{2+}	3.78×10^{-5}	infinite	10000
16	hydrogen ion	H^+	-	-	-
17	hydroxide ion	OH^-	-	-	-
18	hydroperoxyl radical	HO_2	1.13×10^{-4}	4×10^4	5900
19	superoxide radical	O_2^-	-	-	-
20		$\text{OH}-\text{C}(\text{CH}_2\text{COO})_2^- + \text{OH}-\text{C}(\text{CH}_2\text{COOH})_2$	2.69×10^{-6}	infinite	10000
21	radicals				
22	hydroxyl radical	$\cdot\text{OH}$	-	-	-
23	hydrogen peroxide	H_2O_2	1.07×10^{-4}	8.3×10^5	7400
24	oxygen	O_2	1.20×10^{-4}	3.5×10^{-2}	1500
25	carbon dioxide	CO_2	depends on a_w and T	3.4×10^{-1}	2400
26	acetone	CH_3COCH_3	1.18×10^{-5}	30	4600
27	unk prod C_4	C_4	5.30×10^{-6}	1×10^5	6000
28		$\text{O}=\text{C}(\text{CH}_2\text{COO})_2^- + \text{O}=\text{C}(\text{CH}_2\text{COOH})_2$	1.95×10^{-6}	infinite	8000
29	acetic acid	CH_3COOH	3.23×10^{-5}	4.1×10^3	6300
30		$\text{Fe}^{\text{II}}[\text{O}=\text{C}(\text{CH}_2\text{COO})_2]$	7.22×10^{-7}	infinite	10000
31	unk prod C_5	C_5	2.69×10^{-6}	1×10^7	8000
32	unk prod C_5	C_{5_stable}	2.69×10^{-6}	5×10^8	8000

[†] l_i^\ddagger is a factor of the diffusion coefficient of each species j normalized to that of water.

[‡] Henry’s law is described as a function of temperature T : $H = H_0 e^{\frac{Q}{T} - \frac{Q}{T_0}}$.

Table 2. Compilation of equilibria, chemical reactions, and corresponding rate constants in $\text{Fe}^{\text{III}}(\text{Cit})$ photochemistry system.

number	reactions	$K_{eq}/k_r/\sigma$	sources
E1	$\text{H}_2\text{O} \rightleftharpoons \text{OH}^- + \text{H}^+$	$1 \times 10^{-14} \text{ M}$	
E2	$\text{H}_3\text{Cit} \rightleftharpoons \text{H}_2\text{Cit}^- + \text{H}^+$	$7.5 \times 10^{-4} \text{ M}$	Martell and Smith (1982)
E3	$\text{H}_2\text{Cit}^- \rightleftharpoons \text{HCit}^{2-} + \text{H}^+$	$1.7 \times 10^{-5} \text{ M}$	Martell and Smith (1982)
E4	$\text{HCit}^{2-} \rightleftharpoons \text{Cit}^{3-} + \text{H}^+$	$4.0 \times 10^{-7} \text{ M}$	Martell and Smith (1982)
E5	$\text{Fe}^{3+} + \text{Cit}^{3-} \rightleftharpoons \text{Fe}^{\text{III}}(\text{Cit})$	$1.58 \times 10^{13} \text{ M}^{-1}$	tuning parameter
E6	$\text{Fe}^{3+} + \text{Cit}^{3-} + \text{H}_2\text{O} \rightleftharpoons \text{Fe}^{\text{III}}(\text{Cit})(\text{OH})^- + \text{H}^+$	$8.35 \times 10^7 \text{ M}^{-1}$	tuning parameter
E7	$\text{Fe}^{3+} + \text{HCit}^{2-} \rightleftharpoons \text{Fe}^{\text{III}}(\text{HCit})^+$	$2.51 \times 10^7 \text{ M}^{-1}$	tuning parameter
E8	$\text{Fe}^{2+} + \text{HCit}^{2-} \rightleftharpoons \text{Fe}^{\text{II}}(\text{HCit})$	$1.935 \times 10^{10} \text{ M}^{-1}$	tuning parameter
E9	$\text{Fe}^{3+} + \text{H}_2\text{O} \rightleftharpoons \text{Fe}^{\text{III}}(\text{OH})^{2+} + \text{H}^+$	$4.57 \times 10^{-3} \text{ M}$	Smith and Martell (1976)
E10	$\text{O}_2^- + \text{H}^+ \rightleftharpoons \text{HO}_2$	$6.3 \times 10^4 \text{ M}^{-1}$	Bielski et al. (1985)
E11	$\text{Fe}^{2+} + \text{O}=\text{C}(\text{CH}_2\text{COO})_2^{2-} \rightleftharpoons \text{Fe}^{\text{II}}[\text{O}=\text{C}(\text{CH}_2\text{COO})_2]$	$2 \times 10^3 \text{ M}^{-1}$	tuning parameter
E12	$2\text{H}^+ + \text{OH}-\text{C}(\text{CH}_2\text{COO})_2^{2-} \rightleftharpoons \text{OH}-\cdot\text{C}(\text{CH}_2\text{COOH})_2$	$1.5 \times 10^6 \text{ M}^{-2}$	tuning parameter
E13	$2\text{H}^+ + \text{O}=\text{C}(\text{CH}_2\text{COO})_2^{2-} \rightleftharpoons \text{O}=\text{C}(\text{CH}_2\text{COOH})_2$	$1.5 \times 10^6 \text{ M}^{-2}$	tuning parameter
R1	$\text{Fe}^{\text{III}}(\text{Cit}) + h\nu \rightarrow \text{Fe}^{2+} + \text{OH}-\cdot\text{C}(\text{CH}_2\text{COO})_2^- + \text{CO}_2$	3.0×10^{-18} (at 375 nm) or	Pozdnyakov et al. (2012)
R2	$\text{Fe}^{\text{III}}(\text{Cit})(\text{OH})^- + h\nu \rightarrow \text{Fe}^{2+} + \text{OH}-\cdot\text{C}(\text{CH}_2\text{COO})_2^{2-} + \text{OH}^- + \text{CO}_2$	2.3×10^{-19} (at 473 nm) cm^2	
R3	$\text{OH}-\cdot\text{C}(\text{CH}_2\text{COO})_2^- + \text{O}_2 \rightarrow \text{O}=\text{C}(\text{CH}_2\text{COO})_2^- + \text{O}_2^- + \text{H}^+$	$1 \times 10^6 \text{ M}^{-1} \text{ s}^{-1}$	Hug et al. (2001)
R4	$\text{OH}-\cdot\text{C}(\text{CH}_2\text{COO})_2^- + \text{O}_2 \rightarrow \text{O}=\text{C}(\text{CH}_2\text{COO})_2^- + \text{O}_2^- + \text{H}^+$	$1 \times 10^6 \text{ M}^{-1} \text{ s}^{-1}$	Hug et al. (2001)
R4	$\text{HO}_2 + \text{HO}_2 \rightarrow \text{H}_2\text{O}_2 + \text{O}_2$	$2.5 \times 10^7 \text{ M}^{-1} \text{ s}^{-1}$ depends on a_w	tuning parameter
R5	$\text{Fe}^{2+} + \text{O}_2^- (+2\text{H}^+) \rightarrow \text{Fe}^{3+} + \text{H}_2\text{O}_2$	$1 \times 10^7 \text{ M}^{-1} \text{ s}^{-1}$	Rush and Bielski (1985)
R6	$\text{Fe}^{2+} + \text{HO}_2(+\text{H}^+) \rightarrow \text{Fe}^{3+} + \text{H}_2\text{O}_2$	$1.2 \times 10^6 \text{ M}^{-1} \text{ s}^{-1}$	Rush and Bielski (1985)
R7	$\text{Fe}^{2+} + \text{H}_2\text{O}_2 \rightarrow \text{Fe}^{3+} + \cdot\text{OH} + \text{OH}^-$	$76 \text{ M}^{-1} \text{ s}^{-1}$	Walling (1975)
R8	$\text{Fe}^{2+} + \cdot\text{OH} \rightarrow \text{Fe}^{\text{III}}(\text{OH})^{2+}$	$4.3 \times 10^8 \text{ M}^{-1} \text{ s}^{-1}$	Christensen and Sehested (1981)
R9	$\text{Fe}^{\text{II}}(\text{HCit}) + \text{O}_2 \rightarrow \text{Fe}^{\text{III}}(\text{Cit}) + \text{HO}_2$	$0.05 \text{ M}^{-1} \text{ s}^{-1}$	tuning parameter
R10	$\text{C}_3 + h\nu \rightarrow \text{C}_3 + 2\text{CO}_2$	$1 \times 10^{-21} \text{ cm}^2$	tuning parameter
R11	$\text{C}_4 + h\nu \rightarrow \text{C}_3 + \text{CO}_2$	$1 \times 10^{-20} \text{ cm}^2$	tuning parameter
R12	$\text{C}_5 + h\nu \rightarrow \text{C}_2 + \text{C}_3$	$1 \times 10^{-22} \text{ cm}^2$	tuning parameter
R13	$\text{C}_4 + h\nu \rightarrow \text{C}_2 + \text{C}_2$	$1 \times 10^{-21} \text{ cm}^2$	tuning parameter
R14	$\text{C}_5 + h\nu \rightarrow \text{C}_4 + \text{CO}_2$	$1 \times 10^{-20} \text{ cm}^2$	tuning parameter
R15	C_{5_stable} fraction	0.5	tuning parameter
R16	radical self reaction	0	tuning parameter

3 Comparisons between experimental measurements and model simulations

3.1 The effect of RH on photocatalytic degradation efficiency

350 We performed experiments with single, levitated particles under continuous UV irradiation (375 nm) in an O_2 -atmosphere pure O_2 at different RH to access the effects of RH on the photocatalytic cycle shown in Fig. 1, and tested the model performance under these conditions. Qualitatively, a continuous decrease of particle mass and size is expected to occur due to evaporation of volatile products, as shown in Fig. 2. Figure 6 shows the fraction of particle mass remaining with the irradiation time at three different RH , calculated from resonance wavelength shifts (Eqs. (1) and (2)). Clearly, particle mass was lost to the gas phase with time due to the evaporation of photochemical products and similar to Fig. 2, all data show a very significant acceleration of mass loss with time. After tuning some of the parameters of the model as discussed further below, the PRAD model simulations reproduces our data with a very similar trend and magnitude over all, which gives us confidence that the PRAD model captures the essential chemistry and transport during irradiation. (How particle mass evolves subsequently until 80 % mass loss in both experiments and models is shown in Fig. A4.) However, the model is not able to capture the full degree of acceleration of the degradation rate, as it does not attempt to include the complete multi-generational oxidation chemistry at the level of individual components after initial radical production. The degradation progresses processes were faster at higher RH . At lower RH , the particle was expected to be more viscous, diffusion coefficients were expected to be lower, products were generated at a lower rate, and volatile products moved more slowly to the surface to evaporate. More importantly, O_2 taken up by the particle from the gas phase diffused more slowly into the bulk of the particle at lower RH , thus less HO_2 and H_2O_2 formed and less Fe^{II} could be re-oxidized from the surface to the center of the particle. The observed gradient in Fe^{III} fraction, β , and the modelled gradients in O_2 and ROS in the particle have been shown with radial profiles in Alpert et al. (2020, under review). This resulted in fewer photochemically active Fe^{III} complexes available for photocatalytic degradation. The characteristic degradation time shortened by a factor of 5.5 when RH increased from 46 % and 61 %, which demonstrates that photochemical cycling is highly sensitive to the microphysical conditions. The diffusivity of O_2 must have significantly impacted re-oxidation reaction rates. In addition, the diffusion coefficients of both Fe^{II} and Fe^{III} species increases with RH . Therefore, the molecular transport between both iron and oxygen reactants increases causing a highly non-linear trend in increasing mass loss with increasing RH .

3.2 Determination of iron(III) reduction rate and iron(II) re-oxidation rate by STXM/NEXAFS

In STXM/NEXAFS experiments, the freshly prepared $Fe^{III}(Cit)$ mixed with CA at $x = 1.0$ particles were irradiated to determine the $Fe^{III}(Cit)$ photolysis rate, as shown in Fig. 7. Each experimental data point is the average Fe^{III} fraction from 16 – 36 individual particles. Fitting an exponential function, $\beta = \beta_0 e^{j_{obs}t}$, yields $\beta_0 = 0.93 \pm 0.09$ and a first order decay rate of $j_{obs} = 0.08 \pm 0.01 \text{ s}^{-1}$. The LED power at the sample was measured to be $5.9 \pm 0.6 \text{ mW}$ in total and had a Gaussian spectral profile between 361–374 nm at full width-half max. When mounting the UV fiber optics and collimator lens for multiple samples, the illuminated area had a circle equivalent diameter of $5 \pm 1.5 \text{ mm}$. Using the absorption cross section calculated from the molar attenuation coefficient (Pozdnyakov et al., 2008), $\Phi = 1.0$ and propagating all uncertainties yields a photochemical

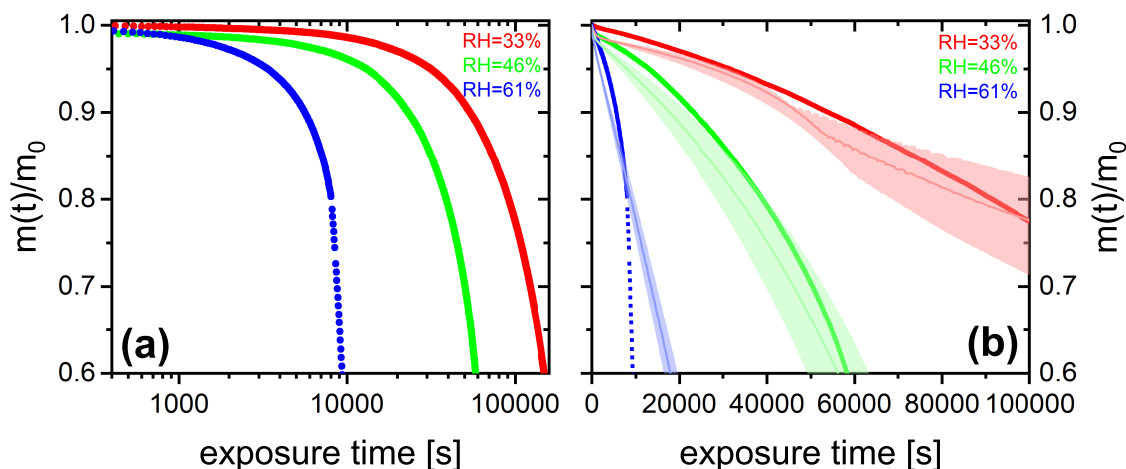


Figure 6. (a) $\text{Fe}^{\text{III}}(\text{Cit})/\text{CA}$ (molar ratio 0.05) particle mass change with irradiation time (log scale) at different RH: 33 % (blackred), 46 % (redgreen), and 61 % (blue). The irradiation wavelength was 375 nm, its intensity was 0.25 W cm^{-2} , and the experimental temperature was 293.5 K. (b) EDB experimental data in (a) with PRAD outputs at corresponding RH (with ± 2 % RH uncertainty shown as shaded area) as a function of irradiation time (linear scale).

reaction rate of $j_{\text{calc}} = 0.20 \pm 0.12 \text{ s}^{-1}$, which is in agreement with j_{obs} . This implies that assuming a quantum yield of 1 at these UV wavelengths is reasonable. This calculated value for the photochemical reaction rate was used in the PRAD model for analyzing the STXM/NEXAFS experiments shown in Fig. 7. We note that our estimate of the photochemical reduction rate and agreement with data is based on the reproducibility of setting up our optical system in the X-ray vacuum chamber. In Fig. 8 (discussed below), this setup procedure was performed for RH=40% and RH=50-60% independently, and still, iron reduction was in agreement with model predictions in the first minutes after UV light was switched off. The width of the red shading in Fig. 7 is large, and likely the UV-fiber setup was the largest source of error for j . A better estimate would require repeat measurements as a function of RH e.g. to elucidate any systematic uncertainty on iron reduction reactions due to viscosity changes. However, this was not possible as usage of the X-ray beam for STXM/NEXAFS experiments was limited to a few days to complete all experiments.

In a different set of experiments, we irradiated particles using much lower power setting having $j = 2.2 \times 10^{-3} \text{ s}^{-1}$ in a mixed He and O_2 atmosphere and at a fixed RH for 15 min to reduce Fe^{III} to Fe^{II} . The UV light was then switched off to allow re-oxidation in the dark while measuring β over time. Figure 8 shows β as a function of time at RH = 40, 50, and 60 %. Clearly, the Fe^{III} fraction increased significantly slower with time at dryer conditions. While particles were observed to re-oxidize to 70 % within 2 hours at 60 % RH and expected to be completely re-oxidized within about 6 hours according to PRAD model simulations, no significant re-oxidation occurred on this timescale for the particles exposed to only 40 % RH. Modelling the re-oxidation with the PRAD model yields very satisfactory agreement, indicating that the diffusivity parameterizations of the model are capturing the RH dependence of the molecular transport in the viscous matrix.

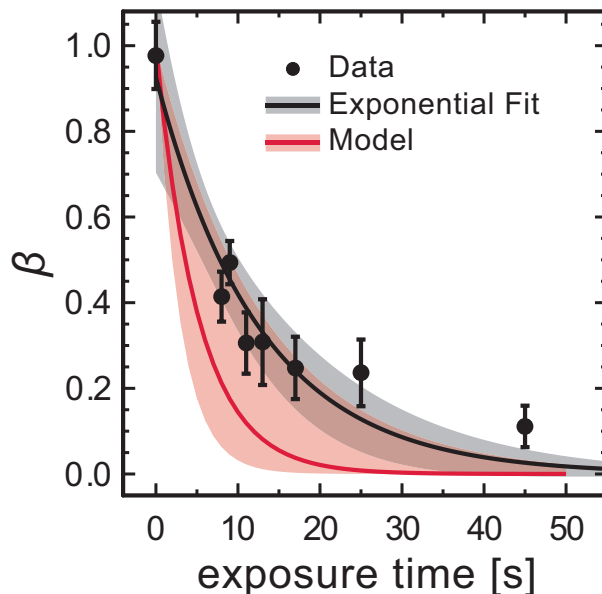


Figure 7. Loss of Fe^{III} in $\text{Fe}^{\text{III}}(\text{Cit})/\text{CA}$ (molar ratio of 1) particles as a function of light exposure time determined using STXM/NEXAFS at 293.5 K. Each data point is the average Fe^{III} fraction over about 16 – 36 individual particles. An exponential fit, $\beta = \beta_0 e^{j_{\text{obs}} t}$, yields for the initial condition is $\beta_0 = 0.93 \pm 0.09$ and a first order decay rate of $j_{\text{obs}} = 0.08 \pm 0.01 \text{ s}^{-1}$. The black shading indicates 95 % confidence on the exponential fit. The PRAD model prediction and uncertainty are given as red solid line and shading, respectively, and uses a calculated decay rate of $j_{\text{calc}} = 0.20 \pm 0.12 \text{ s}^{-1}$.

3.3 Determination of iron(II) re-oxidation rate with single, levitated particle using EDB

400 As the experiments with single, levitated particles yield only bulk properties and not the oxidation state of iron-citrate directly, we designed a dedicated experimental procedure to indirectly determine the re-oxidation rate of Fe^{II} . We used multiple irradiation and re-oxidation repetitions as shown schematically in Fig. 9. Initially, we exposed a newly injected $\text{Fe}^{\text{III}}(\text{Cit})/\text{CA}$ aqueous particle to blue laser irradiation (473 nm , 4 W cm^{-2}) in pure N_2 for 500 s to ensure all Fe^{III} was reduced through photolysis reactions R1 and R2 (listed in Table 2). As previously described, these reactions led to CO_2 production with subsequently loss of CO_2 to the gas phase, which was observed as a shift in the Mie-resonance wavelength. This shift is shown in Fig. 2(b) and on an enlarged scale in Fig. 10. After irradiation, we switched the gas flow from N_2 to O_2 in the dark, and Fe^{II} was oxidized back to Fe^{III} over time in this period, either by ROS (R5–R8) or directly by O_2 (R9). After a desired time spent in O_2 , the gas flow was switched back to N_2 followed by irradiation to repeat the photolysis step done initially. The ratio of the Mie-resonance wavelength shift of the two photolysis steps was set proportional to the ratio of re-oxidized $\text{Fe}^{\text{II}}/\text{Fe}_{\text{tot}}$.

410 These two steps (i.e., photolysis in N_2 and re-oxidation in O_2) were repeated several times, but between each irradiation the particle was exposed to O_2 for different time periods. Following this procedure we intended to map out the characteristic time for re-oxidation at various RH .

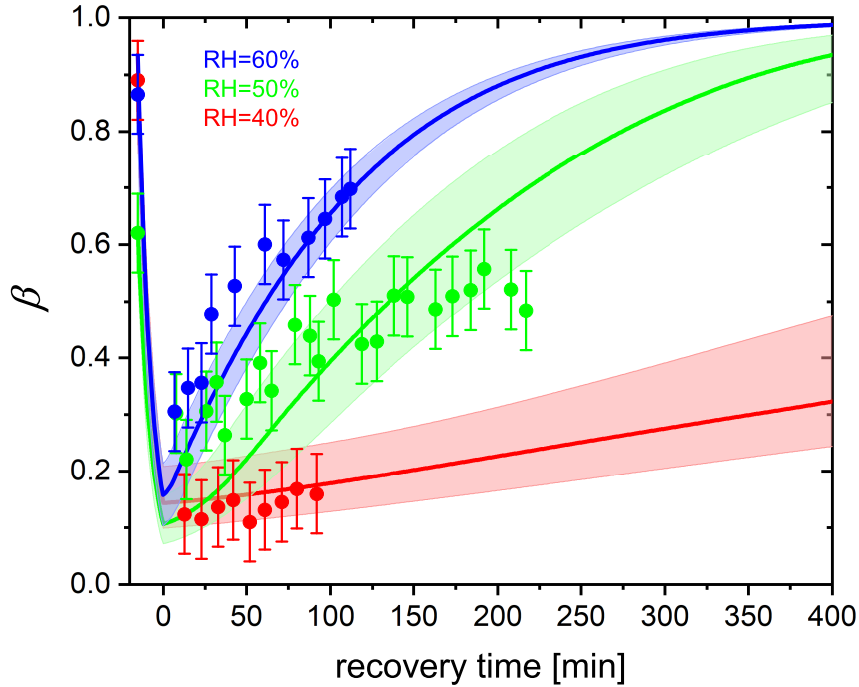


Figure 8. Re-oxidation of Fe^{III} as a function of exposure time in O_2 from STXM observations. Time before 0 represents initial 15 min irradiation procedure under He. $\text{Fe}^{\text{III}}(\text{Cit})/\text{CA}$ (molar ratio of 1) particles at 293.5 K with 40 % RH (red dots), 50 % RH (green dots), and 60 % RH (blue dots). Lines: red (40 % RH), green (48 % RH), and blue (65 % RH) are the Fe^{III} fractions predicted using the PRAD model, the shaded areas indicate model output assuming ± 2 % RH, ± 0.07 initial Fe^{III} fraction, and ± 1.8 % light intensity uncertainty in the STXM experimental conditions.

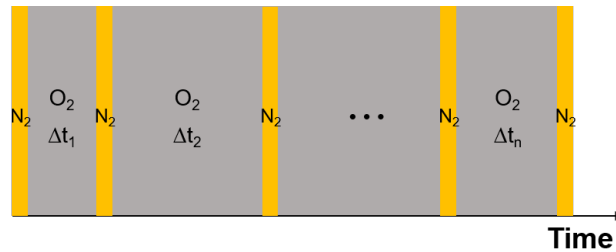


Figure 9. Schematic of the experimental procedure to investigate the re-oxidation rate of Fe^{II} . Orange columns represent laser irradiation (473 nm, 4 W cm^{-2}), each irradiation takes place in a N_2 atmosphere pure N_2 for a period of 500 s; grey columns mark the recovery process in a O_2 atmosphere pure O_2 in the dark, here the time interval is varied. For details see text.

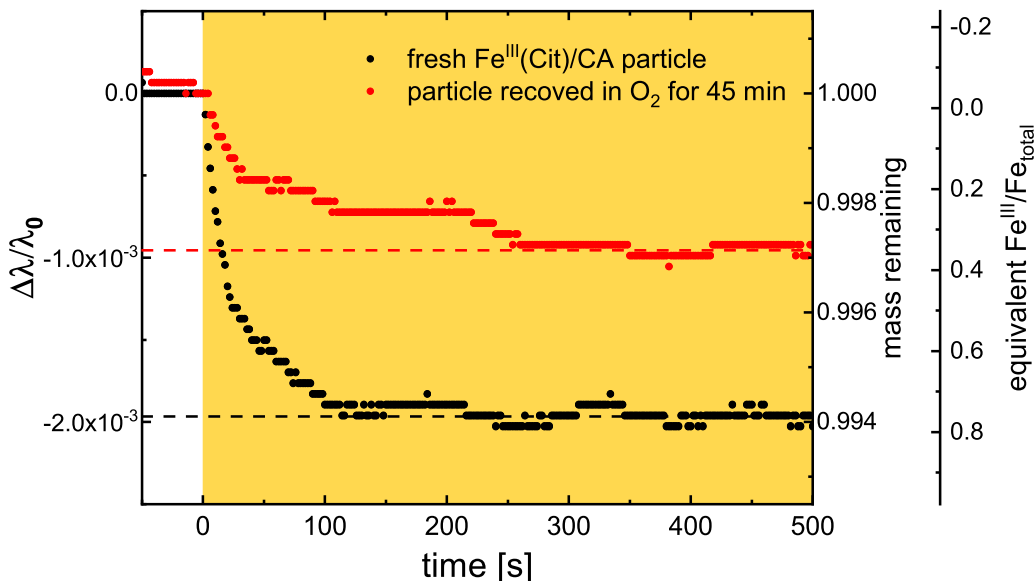
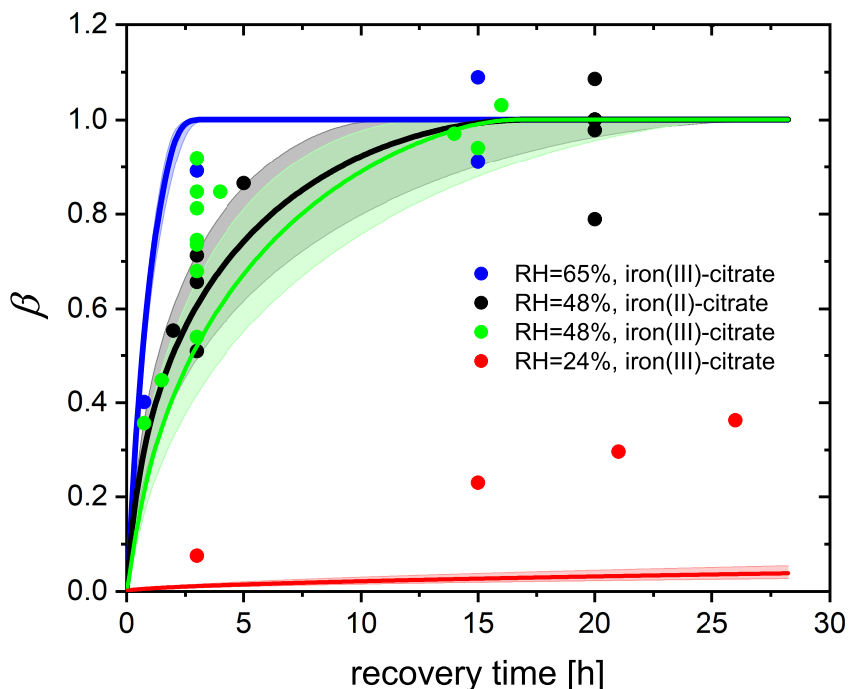


Figure 10. Temporal evolution of two Mie resonance wavelengths shifts and particle mass changes normalized to the wavelength and mass prior irradiation; the experiment was done at 48 % RH and 293.5 K. The orange area marks the time with irradiation (473 nm, 4 W cm⁻²). Black: first irradiation with a fresh Fe^{III}(Cit)/CA particle in N₂, red: irradiation in N₂ right after the particle recovered in O₂ for 45 min in the dark. Two horizontal dashed lines are indicating the final mass remaining after CO₂ loss to the gas phase. For explanation of scaling of the third axis, indicating the equivalent Fe^{III}/Fe_{tot} ratio, see text.

An example of the corresponding raw data (293.5 K and 48 % RH) and retrieved oxidation state is shown Fig. 10. Black circles indicate the first irradiation step with a fresh Fe^{III}(Cit)/CA particle, and red circles indicate the irradiation step that followed the particle after exposure to O₂ for 45 min in the dark. Clearly, the resonance wavelength decreased more during the first irradiation than the second. Therefore, we can conclude unambiguously that the Fe^{III}(Cit)/CA particle initially had more Fe^{III} than what could be re-oxidized in O₂ for 45 min. Quantitative scaling however, requires knowledge of the initial Fe^{III} fraction. Our experiments showed that long exposure (tens of hours) to O₂ yielded larger Mie-resonance shifts than those of the initial photolysis of the freshly prepared particle. This indicated that the initial Fe^{III} fraction was less than 1.0. Hence, we normalized the Fe^{III} fraction accordingly to the data at long (> 15 hours) exposure times. For the experiment included in Fig. 10 for example, the initial Fe^{III} fraction of the particle was 0.76, indicating that the particle has been partially reduced during sample preparation. After the particle has been totally photoreduced, exposure to O₂ for 45 min did not re-oxidize all reduced Fe^{II} to Fe^{III}, but only 0.36 Fe^{III} has been recovered (as shown with two horizontal dashed lines in Fig. 10).



Another set of experiments was done by starting with freshly injected $\text{Fe}^{\text{II}}(\text{HCit})/\text{CA}$ particles instead of $\text{Fe}^{\text{III}}(\text{Cit})/\text{CA}$.
 425 The only difference in experimental procedure, compared to what is described above, is that there is no first irradiation step. Instead, the particle is initially exposed to O_2 in the dark for a certain time interval, during which Fe^{II} is oxidized only directly by O_2 (reaction R9). Afterwards, the same irradiation and recovery procedures as reported above were taken. The equivalent Fe^{III} fractions of all experiments are shown in Fig. 11. Any uncertainty in the normalization of an individual experiment will cause a corresponding uncertainty in the normalized mass loss, which made estimating the uncertainty for individual data
 430 points impossible. Nevertheless, from the complete data set, it was evident that with longer time intervals in O_2 , more Fe^{III} was recovered. At 48 % and 65 % RH, about 10 hours and 3 hours exposure to O_2 , respectively, was sufficient for all Fe^{II} to be re-oxidized, while at 24 % RH, the recovery even after 25 h was not yet complete. The general trend is consistent with our observation in the STXM/NEXAFS experiments (section. 3.2) and can be attributed to molecular diffusion limitations at lower RH: it takes more time for O_2 to diffuse into the particle, and for Fe^{II} to diffuse out to the surface of the particle to react
 435 with O_2 . It was also evident from these data that Fe^{II} re-oxidized by O_2 is as important as Fe^{II} re-oxidized by radicals and peroxides as there is no significant difference between the experiments starting from $\text{Fe}^{\text{II}}(\text{HCit})/\text{CA}$ compared to those with $\text{Fe}^{\text{III}}(\text{Cit})/\text{CA}$. In addition, it indicates that both $\text{Fe}(\text{II})$ and $\text{Fe}(\text{III})$ can act as a photocatalyst as long as $\text{Fe}(\text{II})$ can be oxidized to $\text{Fe}(\text{III})$, which was also confirmed by Grgić et al. (1999).

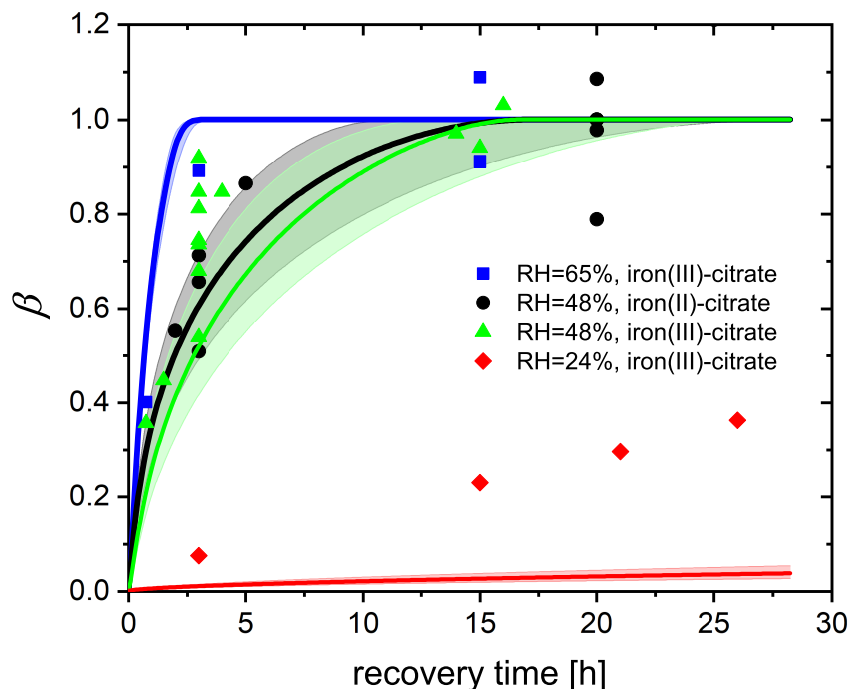
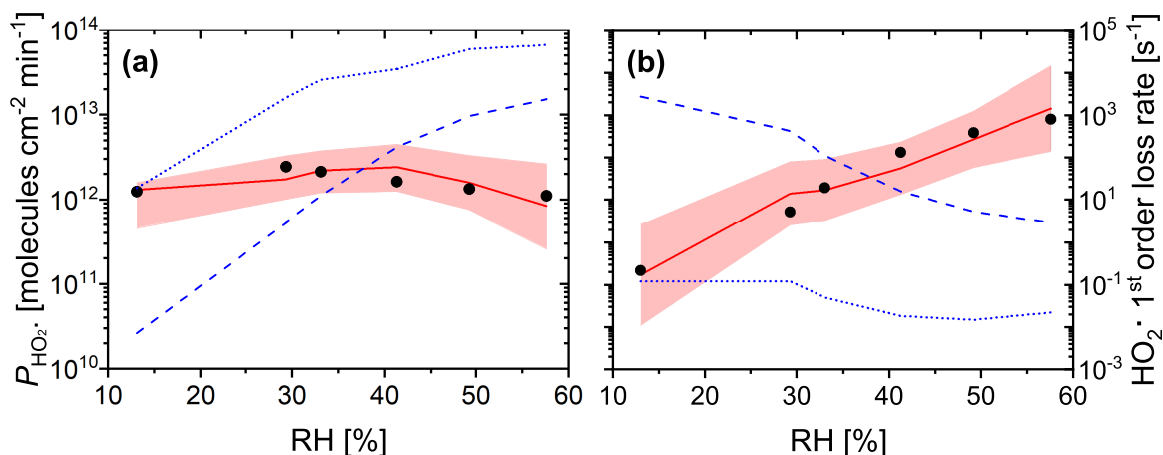


Figure 11. Fe^{III} fraction after different time intervals of recovery in O_2 from EDB observations. $\text{Fe}^{\text{III}}(\text{Cit})/\text{CA}$ (molar ratio of 0.05) particles at 293.5 K with 24 % RH (red dots diamonds), 48 % RH (green dots triangles), and 65 % RH (blue dots squares). Black dots: experiments with $\text{Fe}^{\text{II}}(\text{HCit})/\text{CA}$ particles at 48 % RH. Lines: red (24 % RH), black (48 % RH), and blue (65 % RH) are the Fe^{III} fractions predicted using the PRAD model, the shaded areas indicate model output assuming $\pm 2\%$ RH uncertainty in the EDB experimental conditions.

By tuning the direct oxidation rate of $\text{Fe}^{\text{II}}(\text{HCit})$ by O_2 (R9) and the diffusivity of O_2 , we are able to model the recovery rate
 440 at different RH using the PRAD model as shown in Fig. 11. There is satisfactory agreement for the larger RH , but significant
 underestimation of re-oxidation for the experiments at 24 % RH. Our model requires the reaction rate coefficient of R9 to be
 $0.05 \text{ M}^{-1} \text{ s}^{-1}$, which is a factor of 60 smaller than the value that Gonzalez et al. (2017) estimated from their model (3 ± 0.7
 $\text{M}^{-1} \text{ s}^{-1}$). The liquid phase diffusivity of O_2 in our model is $7.1 \times 10^{-19} \text{ m}^2 \text{ s}^{-1}$ at 24 % RH, $1.9 \times 10^{-15} \text{ m}^2 \text{ s}^{-1}$ at 48
 %, and $2.1 \times 10^{-14} \text{ m}^2 \text{ s}^{-1}$ at 65 % RH. These diffusivities of O_2 are 2 – 4 orders of magnitude smaller than those of CO_2
 445 determined in Dou et al. (2019). However, we need to stress that in the model, some of the iron related complex equilibrium
 constants and their diffusion coefficients, and the Henry's law coefficient of O_2 at different water activities are highly uncertain
 as well, yielding to a significant uncertainty in the determination of O_2 diffusivity. For example, if the solubility of O_2 would
 be less than what our parameters predict now, a larger O_2 diffusivity would be consistent with our data. In addition, with the
 total gas flow used in our experiments, it takes about 8 min for replacing the entire EDB gas volume from N_2 to O_2 , and from



450 the response of the particle to flow condition change, we estimate an interval of about 30 min to reach full equilibration to the new gas phase conditions. Therefore, the life time of organic radicals needs to be reconsidered. In the PRAD model, we do not take the radical-radical self reactions (R16) into account, which may turn out to be a significant sink for the radicals. However, it should be pointed out that the parameter set we have now is a good compromise with additional constraints from STXM/NEXAFS and CWFT experiments.

455 Another approximate approach to analyse the data of Fig. 11 is to use the analytical solutions for a reacto-diffusive kinetic regime. Here, O_2 taken up from the gas phase by a particle remains confined to a very thin layer below its surface compared to its size provided it reacts reasonably fast with the organic components. Under these conditions there are always pairs of reaction rate and diffusion constants representing the experiments equally well (Alpert et al., 2019; Steimer et al., 2014). In the reacto-diffusive framework, with constrained reaction rate and Henry's law coefficient of O_2 , the diffusion coefficient of O_2 can be estimated to be 3.6×10^{-16} and $4.4 \times 10^{-15} \text{ m}^2 \text{ s}^{-1}$ at 48 % and 65 % RH, respectively (details are given in Appendix A4). These are both one order of magnitude less than the values from PRAD model prediction, but still consistent with each other when considering all uncertainties.

3.4 HO_2 production measured by CWFT experiments

The CWFT experiment allows us to investigate another aspect of the photochemistry of the $\text{Fe}^{\text{III}}(\text{Cit})/\text{CA}$ system. According to reactions R1–R3 shown in Table 2, the HO_2 radical is produced upon irradiation and will partition to the gas phase. Figure 12(a) shows the RH dependence of HO_2 production, P_{HO_2} , from thin films in CWFT experiment. We observed that P_{HO_2} increased with RH when the RH was increased from 13 % to 29 % by a factor of about 2. This may be expected since an increase from 13 % to 29 % RH leads to increasing molecular diffusion coefficients and faster chemical cycling (Lienhard et al., 2014; Song et al., 2016). However, at RH between 30 % and 60 %, P_{HO_2} decreased with RH , with a production rate at 470 60 % similar to the one under dry conditions. This is probably due to the decreasing concentrations of donors (e.g., $\text{Fe}^{\text{III}}(\text{Cit})$)

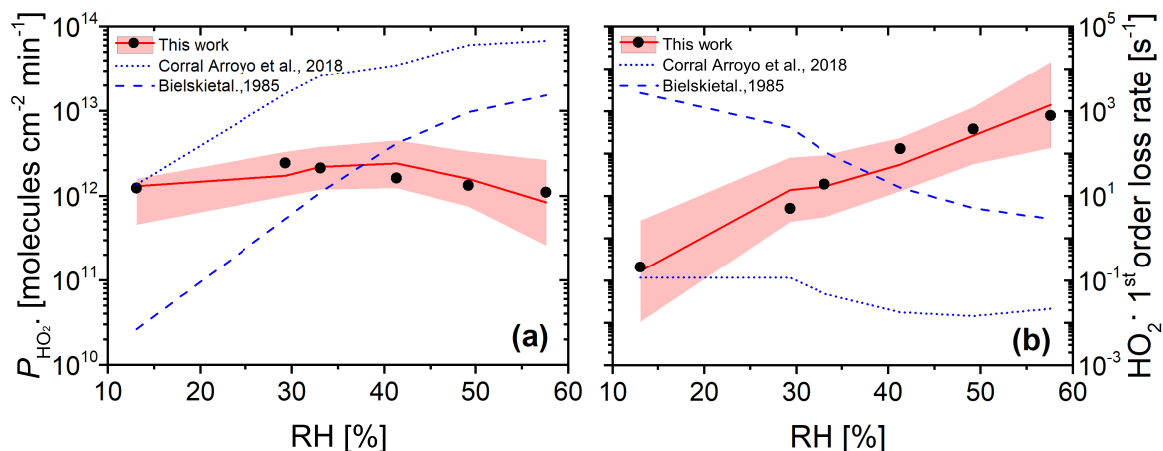


Figure 12. (a) Measured (black dots, experimental uncertainty of 3 % smaller than symbol size) and modelled (red line and shaded area) HO₂ production from continued photochemistry of Fe^{III}(Cit)/CA (molar ratio of 0.07) films as a function of RH in CWFT experiments. Dotted and dashed blue lines were determined from parameterization of k_5 as a function of RH (Corral Arroyo et al., 2018) and $k_5 = 8.3 \times 10^5 \text{ M}^{-1} \text{ s}^{-1}$ in dilute aqueous solution (Bielski et al., 1985), respectively. (b) The maximum HO₂ first order loss rate determined from the result of the maximum HO₂ concentration times HO₂ self reaction rate, k_5 , which was adjusted to match observations in panel (a) (black dots), or times k_5 parameterized as a function of RH for our PRAD model (Eq. (A11)) with confidence interval of 95 % (red line and shading), or times k_5 from Corral Arroyo et al. (2018) (dotted blue line), or $k_5 = 8.3 \times 10^5 \text{ M}^{-1} \text{ s}^{-1}$ (Bielski et al., 1985) (dashed blue line).

and Cit³⁻). But the decrease in concentrations with RH is too small compared the increase in diffusion coefficients with RH . This means that there must be a strong sink of HO₂ in the condensed phase when RH increases, which has been confirmed by an increasing HO₂ first order loss rate as shown with black dots in Figure 12(b). When predicting P_{HO_2} with the PRAD model using a constant HO₂ self reaction rate of $k_5 = 8.5 \times 10^5 \text{ M}^{-1} \text{ s}^{-1}$ (Bielski et al., 1985) or a linearly increasing P_{HO_2} with RH , as in Corral Arroyo et al. (2018), the model deviates significantly from the data and does not exhibit the observed trend of decreasing P_{HO_2} for $RH > 30 \%$. Both assumptions lead to a continuous increase P_{HO_2} with RH as indicated as dashed and dotted blue lines in Fig. 12(a), with a decrease HO₂ first order loss rate as shown in Fig. 12(b), which is opposite from our adjustment. Therefore, we argue that the effects of the increasing diffusivity and the stronger sink of HO₂ with RH compensate each other, making P_{HO_2} almost independent of RH .

480 3.5 Photochemical degradation under atmospheric conditions

The PRAD model was developed to also be used in more general particle systems. After establishing a parameter set for the PRAD model framework which satisfactorily explains the experimental data obtained with three complimentary experimental techniques over a wide parameter range, we used the model for predicting photochemical degradation of organic aerosol particles containing carboxylate complexes. For example, an aqueous organic acid particle with a dust inclusion containing

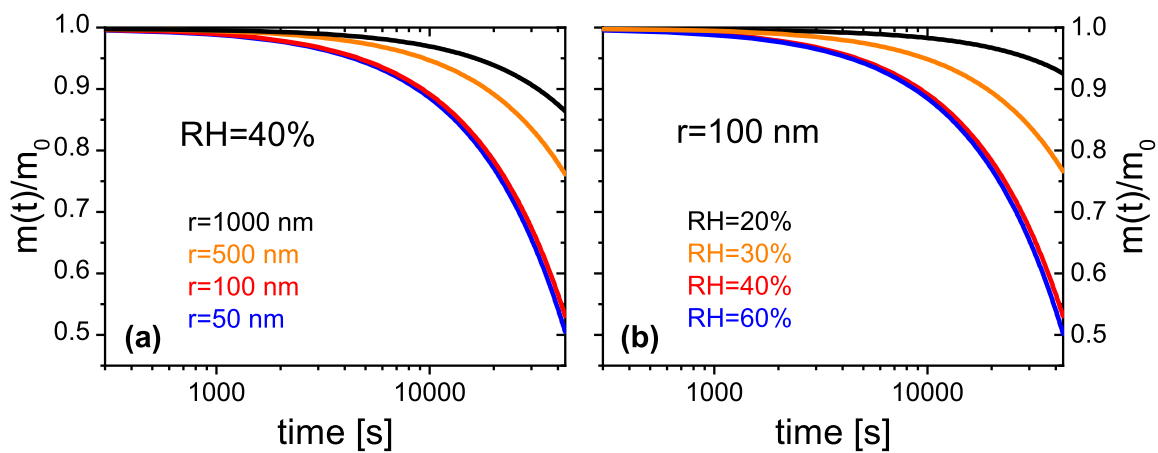
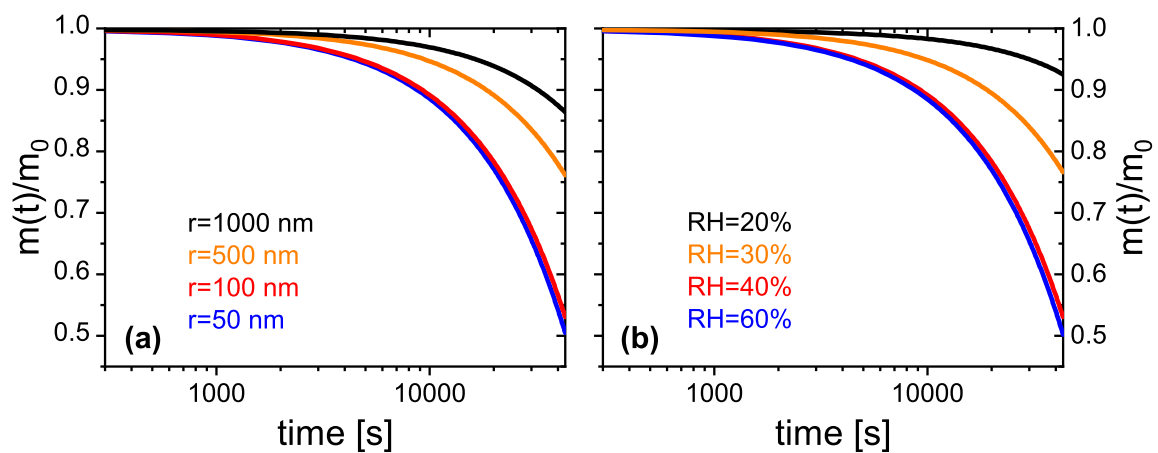


Figure 13. PRAD simulated organic mass loss of $\text{Fe}^{\text{III}}(\text{Cit})/\text{CA}$ (molar ratio of 0.01) for (a) particles of different radii at 40% RH, and (b) particles with a radius of 100 nm at different RH . All simulations for 293.5 K and 12 h solar irradiation at 30° zenith angle (Madronich et al., 1995).

485 iron, may exhibit a low enough pH to dissolve part of the iron of the dust inclusion and form photo-reactive iron carboxylate complexes (Dou et al., 2020) (George et al., 2012, 2015). If we take the PRAD model as being representative for such a class of particles, we may estimate the degradation of the organic mass by volatilization of products to the gas phase. Figure 13 show examples of such PRAD model predictions: we assume that the organic mass of the particle is composed of aqueous $\text{Fe}^{\text{III}}(\text{Cit})/\text{CA}$ with a molar ratio of the latter being 0.01. Here panel (a) illustrates size dependence and panel (b) illustrates
490 RH dependence for particles exposed to air at 293.5 K and an actinic flux at 30° zenith angle (Madronich et al., 1995). After 12 hours exposure to sunlight, the organic mass of the particle (here citric acid) has been photochemically processed to CO_2 and smaller compounds of high volatility yielding a combined mass loss to the gas phase of up to 50 % depending on size and RH.

To better understand the importance of mass loss in this generalized system, we make a simple and modest comparison of
495 mass loss in Fig. 13 on the order of 20% over 5 hours with ambient mass accumulation measured in the field. Our results are equal to a mass loss rate of about $0.4 \mu\text{g m}^{-3}(\text{air}) \text{hr}^{-1}$ assuming an aerosol population with an organic mass of $\sim 10 \mu\text{g m}^{-3}(\text{air})$ undergoing iron-carboxylate photochemistry. This is much larger than observed organic mass accumulation in ambient air masses due to photochemical aging during atmospheric transport at about $0.06 \mu\text{g m}^{-3} \text{hr}^{-1}$ or $6 \mu\text{g m}^{-3}$ over 4 days (Zaveri et al., 2012; Moffet et al., 2012). This implies, that the mass loss rates are fast enough to affect the balance between
500 aerosol mass accumulation and loss. Hence, photochemical degradation may be very significant in iron containing organic aerosol, perhaps even more important than degradation through reactions with gas phase oxidants under high particle viscosity conditions. Note, that our model does not fully capture the acceleration of degradation as discussed in Sect. 3.1. Therefore, we argue that the degradation presented in Fig. 13 represents a lower limit of the expected degradation under atmospheric conditions. Clearly, panel (a) indicates that smaller particles degrade significantly faster than larger ones. However, the size
505 dependence is more complex than a simple square law expected if reactions were purely limited by condensed phase diffusion. For particles with a radius larger than 50 nm, the time to re-partition 10 % of the mass to the gas phase depends almost linearly on size for these specific conditions. Panel (b) shows that photochemical processes are faster at higher RH corresponding to less viscous particles. The relative mass loss after 12 h irradiation between 20 % and 60 % RH is almost an order of magnitude larger for the highest RH compared to dry conditions, because of transport limitations at low RH. However, it should be
510 noted that the relative mass loss at higher humidities (between 40 % and 60 % RH) is quite similar. Here, the photochemical degradation is barely limited by condensed phase diffusivity, but by iron availability in the particle. These simulations show the potential of photochemical degradation under atmospheric conditions, a systematic study exploring the whole range of atmospheric conditions is beyond the scope to this work.

4 Conclusions

515 We used three complimentary experimental techniques to characterize the impact of reduced mobility of aerosol constituents on photochemical degradation in highly viscous particles. As an atmospherically relevant model system, we chose aqueous $\text{Fe}^{\text{III}}(\text{Cit})/\text{CA}$ particles. These three experimental techniques investigated specific aspects of this photochemical reaction

system. In EDB experiments, we measured the mass loss relating to the continual production and loss of CO₂ and other volatile products. We observed very significant condensed phase degradation and strong acceleration of the degradation rate with time. Further studies are needed to quantify all atmospheric implications, but our study suggests that photochemistry in iron containing organic aerosol will lead to a significant re-partitioning of condensed phase mass to the gas phase. We used STXM/NEXAFS to directly measure iron oxidation state in-situ with an environmental microreactor. These experiments yielded valuable information about where iron photochemical reduction and re-oxidation reactions took place, namely only very close to the surface, and it allowed to characterize to which degree iron compounds diffused inside single particles. We show that O₂ uptake and diffusion into a particle is a limiting factor considering the reactions required to produce species with an oxidative potential. In addition, we found that the direct O₂ reaction with iron(II)-organic complexes does occur and generate radicals inside the particle. Flow tube experiments performed on thin Fe^{III}(Cit) films showed continuous production of HO₂, revealing a radical source inside the particles driven by photochemistry.

All data were used to constrain equilibrium and kinetic parameters as well as reaction rate coefficients in a new photochemical reaction and diffusion (PRAD) model with sufficient complexity to allow comparison with data of all experiments simultaneously. In particular, we were able to constrain the photolysis rate of Fe^{III} due to the use of various light sources with various spectral intensities, while capturing the photochemical reduction. In addition, we determined the HO₂ production rate and its first order loss rate, and the diffusivity of O₂ in aqueous Fe^{III}(Cit)/CA system as a function of *RH* and Fe^{III}(Cit)/CA molar ratio with a choice of O₂ related reaction rate coefficient and O₂ Henry's law coefficient.

Although a systematic study exploring the whole range of atmospheric conditions was beyond the scope to this work, there are some aspects of the PRAD model and certain parameters that we argue are reliable and pertainate to atmospheric aerosol photochemistry. First, coefficients in the PRAD model framework can be changed to predict mass loss rates of a different iron-carboxylate complex system. We are fairly confident that diffusion coefficients of CO₂ and H₂O can be used for atmospheric aerosol particles as these were obtained in a more targeted study (Dou et al., 2019). Mass loss rates in general are fairly reliable to be used in atmospheric particles as these are linked to photochemical reaction rates which have been characterized (Weller et al., 2013, 2014). Finally, reoxidation rates and production of radicals are also reliable, as the system is largely reacto-diffusion limited (see appendix A4) and these rates occur on the same scales as observed mass loss rates. In our companion paper (Alpert et al., 2020, under review), we show a detailed analysis of radical concentrations in ambient aerosol particles for a range of atmospheric conditions and iron content. However, our model still needs major improvements, such as including peroxy radical chemistry and better constraints on individual parameters such as diffusion coefficients and reaction rate constants. The overall rate may be well-constrained by our experimental studies, however more targeted observations may be necessary for an accurate representation of O₂ chemistry, solubility and molecular transport independently of each other within aerosol particles.

As illustrated in the preceding sections, the PRAD model was able to simulate the experiments generally with satisfactory agreement. Our results and use of the PRAD model also highlight the need for future study to better constrain aspects of the iron carboxylate photochemical system. The chemical evolution of the organic species resulting from the continual photochemical oxidation was not the scope of the present study. A separate study focusing on individual OVOCs and condensed phase products

is currently underway that will allow to better constrain the chemical regimes and the evolution of the oxidation state of the organic fraction with time. This will also allow to assess more details of organic peroxy radical chemistry that help to explain the observed 'missing' HO₂ sink in this system. Furthermore, testing the PRAD model with different organic carboxylate ligands is desirable to broaden its applicability.

Using the PRAD model for predicting photochemical degradation for iron containing organic aerosol under atmospheric conditions let us conclude that this pathway of re-partitioning condensed phase mass to the gas phase is important and its regional and global impact should be investigated in further modelling studies. The PRAD model may serve as a basic framework for the chemistry and transport of compounds in single particles for such studies.

Code and data availability. The data that support the findings of this study and the PRAD model code are publicly available and accessible, and from the corresponding author upon request.

Video supplement. The video supplement related to this article is available online at: <https://doi.org/10.5446/47955>.

Appendix A

565 A1 Parameterization of $D_1^j(x, T, a_w)$

The liquid phase diffusion coefficients, $D_1^j(x, T, a_w)$, where j is an index for all species, depend on RH , T and the molar ratio, x , between $\text{Fe}^{\text{III}}(\text{Cit})$ and CA. $D_1^j(x, T, a_w)$ was scaled with the diffusion coefficient of water in $\text{Fe}^{\text{III}}(\text{Cit})/\text{CA}$ aqueous system, $D_1^{\text{H}_2\text{O}}(x, T, a_w)$ using a scaling factor, l_f^j , following

$$l_f^j = \frac{D_1^j(x, T, a_w)}{D_1^{\text{H}_2\text{O}}(x, T, a_w)}. \quad (\text{A1})$$

570 $D_1^j(x, T, a_w)$ has not been previously determined for aqueous $\text{Fe}^{\text{III}}(\text{Cit})/\text{CA}$ although, solution viscosity has and was found to be higher than aqueous CA solutions when $x > 0.05$ (Alpert et al., 2020, under review), implying slower molecular transport. Lienhard et al. (2014) reported the diffusion coefficient of water in aqueous CA without iron (i.e. $x = 0$), $D_{\text{CA}(\text{aq})}^{\text{H}_2\text{O}}(T, a_w)$. In order to determine $D_1^j(x, T, a_w)$ in the PRAD model for a single experiment with a fixed value of x , $D_1^{\text{H}_2\text{O}}$ was scaled with $D_{\text{CA}(\text{aq})}^{\text{H}_2\text{O}}(T, a_w)$ using another factor, f_s , following

$$575 D_1^{\text{H}_2\text{O}}(x, T, a_w) = D_{\text{CA}(\text{aq})}^{\text{H}_2\text{O}}(T, a_w) f_s(x), \quad (\text{A2})$$

where

$$\log f_s(x) = -0.7106e^{-\frac{1}{4x}}. \quad (\text{A3})$$

The diffusion coefficient of CO_2 at $T = 20^\circ\text{C}$ and $x = 0.05$, $D_{\circ}^{\text{CO}_2}$, has been independently measured by Dou et al. (2019) as a function of a_w . We parameterized $D_{\circ}^{\text{CO}_2}$ as

$$580 D_{\circ}^{\text{CO}_2} = \left(D_{\circ}^{\text{CO}_2}(a_w = 1)\right)^{\alpha \cdot a_w} \cdot \left(D_{\circ}^{\text{CO}_2}(a_w = 0)\right)^{1 - \alpha \cdot a_w}, \quad (\text{A4})$$

where $D_{\circ}^{\text{CO}_2}(a_w = 0) = 1.19 \times 10^{-16} \text{ m}^2 \text{ s}^{-1}$ is the diffusion coefficient of CO_2 at $T = 20^\circ\text{C}$, $x = 0.05$ and $a_w = 0$. The T dependent diffusion coefficient of CO_2 in water in Eq. (A4) is

$$D_{\circ}^{\text{CO}_2}(a_w = 1) = D_0 \left(\frac{T}{T_s} - 1\right)^m, \quad (\text{A5})$$

where $D_0 = 1.39 \times 10^{-8} \text{ m}^2 \text{ s}^{-1}$, $T_s = 227.0 \text{ K}$ and $m = 1.7094$. In the exponent terms of Eq. (A4),

$$585 \alpha = e^{(1-a_w)^2(A+B \cdot a_w)}, \quad (\text{A6})$$

where $A = 0.2824$, and $B = -1.8086$. In order to introduce a x dependence of $D_1^{\text{CO}_2}$ for various experiments reported here, f_s from Eq. (A3) for water was applied, following

$$D_1^{\text{CO}_2}(x, T, a_w) = D_{\circ}^{\text{CO}_2}(T, a_w) f_s(x). \quad (\text{A7})$$

For all other species (excluding H_2O and CO_2), $D_1^j(x, T, a_w)$ was determined using Eq. (A1) with

$$590 \log l_f^j = -0.7710M_j^{\frac{1}{3}} - 1.4732, \quad (\text{A8})$$

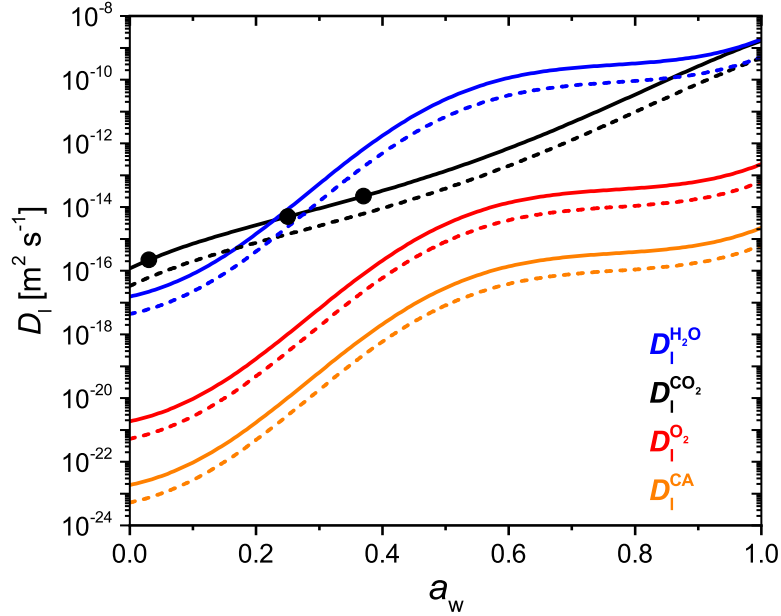


Figure A1. Parameterized liquid phase diffusion coefficients of H₂O (blue), CO₂ (black), O₂ (red), and CA (orange) as a function of water activity at Fe^{III}(Cit)/CA molar ratio of 0.05 (solid lines) and 1.0 (dashed lines). Three black dots are measured CO₂ diffusivity in Fe^{III}(Cit)/CA particle with a molar ratio of 0.05 (Dou et al., 2019). The temperature is all at 293.5 K.

where, M_j , is molar mass. Diffusion coefficients of H₂O, CO₂, O₂, and CA as a function of a_w at $x = 0.05$ and 1.0 are plotted in Fig. A1. Generally, $D_1^j(x, T, a_w)$ always decreases when RH or T is lowered. $D_1^j(x, T, a_w)$ decreases when x increases beyond 0.05, but remains relatively constant otherwise. One caveat to using Eqs. (A1)–(A8) to calculate D_1^j is that mass loss will ultimately lead to an increase in x , however, the PRAD model keeps D_1^j fixed throughout the course of a model run. Since we observed increasing mass loss rates over time, any decrease in D_1^j leading to slower chemical cycling due to increasing x was likely a minor effect. Moreover, the product distribution and any effect on diffusion coefficients was unknown, and so further time-resolved adjustments to D_1^j were not considered. We suggest future studies investigate how molecular transport changes over the photochemical lifetime of iron-carboxylate complexes.

A2 Parameterization of D_g^j

The gas phase diffusivity of each species j , D_g^j , was approximated via its molar mass (M_j) compared to that of water ($M_{\text{H}_2\text{O}}$),

$$D_g^j = D_g^{\text{H}_2\text{O}} \sqrt{\frac{M_{\text{H}_2\text{O}}}{M_j}}, \quad (\text{A9})$$

with

$$D_g^{\text{H}_2\text{O}} = 0.211 \left(\frac{T}{T_0} \right)^{1.94} \left(\frac{p_0}{p} \right), \quad (\text{A10})$$

605 where $T_0 = 273.15$ K, $p_0 = 1013.25$ mb, and $D_g^{\text{H}_2\text{O}}$ is in $\text{cm}^2 \text{s}^{-1}$ (Pruppacher and Klett, 2010).

A3 Parameterization of k_5

Based on the measurement of HO_2 production as a function of RH using CWFT experiments, the HO_2 self reaction rate (R4 in Table 2), k_5 , was adjusted so the PRAD model would exactly reproduce the data. We parameterized k_5 as a third degree polynomial function of RH (%):

$$610 \log k_5 = -2.854 \times 10^{-5} RH^3 + 0.0024 RH^2 + 0.1087 RH - 0.05018, \quad (\text{A11})$$

as shown in Fig. A2.

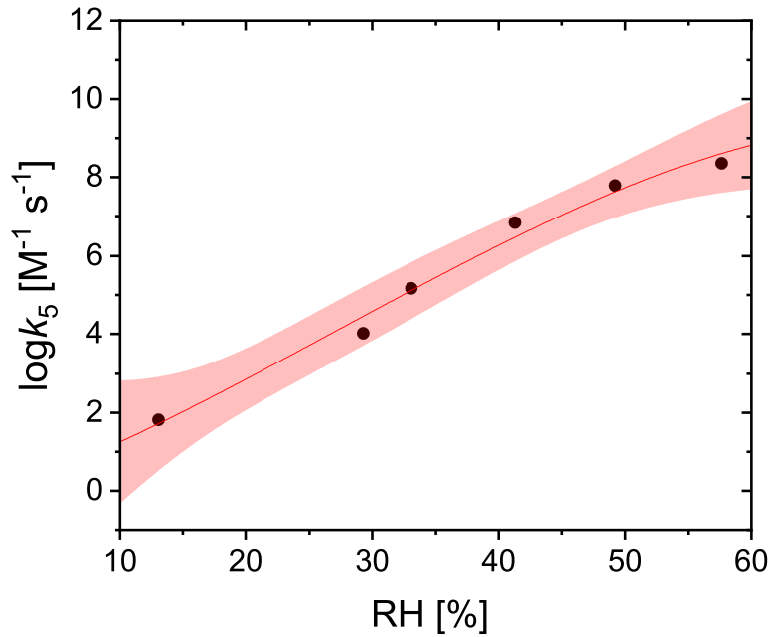


Figure A2. Adjusted values of HO_2 self reaction rate used in the PRAD model to exactly reproduce measured P_{HO_2} for CWFT experiments are shown as black dots. The red line and shading is the new parameterization (Eq. (A11)) and confidence intervals at 95 % for the HO_2 self reaction rate as a function of RH .

A4 β estimated by a reacto-diffusive framework

It is well known that multi-phase reactions can follow a reacto-diffusive kinetic regime (Alpert et al., 2019; Steimer et al., 2014). For reacto-diffusive limitations as observed in Fig. 11, the Fe^{III} fraction as a function of time was calculated as

$$615 \quad \beta(t) = 1 - (1 - Kt)^2, \quad (\text{A12})$$

with the assumption that $\beta_0 = 0$, i.e. there was no Fe^{III} at $t = 0$.

$$K = \frac{3(H_{\text{O}_2} \sqrt{D_1^{\text{O}_2}}) p_{\text{O}_2} \sqrt{k_{\text{O}_2}}}{\sqrt{[\text{Fe}_{\text{tot}}]} d_p}, \quad (\text{A13})$$

where H_{O_2} and $D_1^{\text{O}_2}$ are Henry's law coefficient and diffusion coefficient for O_2 in the $\text{Fe}^{\text{III}}(\text{Cit})/\text{CA}$ matrix, p_{O_2} is the pressure of O_2 , k_{O_2} is the total reaction rate of O_2 , and d_p is diameter of the single particle. $\beta = \frac{1}{e}$ when

$$620 \quad t_{\frac{1}{e}} = \frac{1 - \sqrt{1 - \frac{1}{e}}}{K} = \frac{\left(1 - \sqrt{1 - \frac{1}{e}}\right) \sqrt{[\text{Fe}_{\text{tot}}]} d_p}{3(H_{\text{O}_2} \sqrt{D_1^{\text{O}_2}}) p_{\text{O}_2} \sqrt{k_{\text{O}_2}}}. \quad (\text{A14})$$

In a typical EDB experiment, $d_p = 20 \mu\text{m}$, $H_{\text{O}_2} = 3.5 \times 10^{-2} \text{ M atm}^{-1}$, $p_{\text{O}_2} = 8 \times 10^4 \text{ Pa} = 0.789 \text{ atm}$, and $k_{\text{O}_2} = 0.05 \text{ M}^{-1} \text{ s}^{-1}$. $[\text{Fe}_{\text{tot}}]$ is 0.3192, 0.2763, and 0.2345 M at 24 %, 48 %, and 65 % RH, respectively. From EDB data points in Fig. 11, we estimated that $\frac{1}{e}$ of Fe^{III} can be fully recovered after around 1.7 h at 48 % RH and 0.45 h at 65 % RH. Thus the diffusion coefficient of O_2 can be estimated to be 3.6×10^{-16} and $4.4 \times 10^{-15} \text{ m}^2 \text{ s}^{-1}$ at 48 % and 65 % RH, respectively, which are both
625 one order of magnitude less than the values from PRAD model prediction, but still consistent with each other when considering all uncertainties. It should be noted that in Eq. (A14), actually $H_{\text{O}_2} \sqrt{D_1^{\text{O}_2} k_{\text{O}_2}}$ is the constraint, thus any uncertainty in H_{O_2} or k_{O_2} can change $D_1^{\text{O}_2}$.

A5 Sensitivity of the PRAD model to various model parameters

630 As discussed in section 2.5 we performed manual tuning of the PRAD model parameters to reach satisfactory agreement with all experimental data simultaneously. To show the sensitivity of the PRAD model results to a few of its parameters Fig. A3 shows again the data of the photocatalytic degradation experiment at 46 % RH described in section 3.1. In addition we show the output of the model as well as model outputs obtained by varying one of the parameters by the indicated factors while keeping all other parameters constant. Clearly, the sensitivities of the model output to varying these parameters are very different: while
635 the model output is quite sensitive to varying the rate constant of for the oxidation of $\text{Fe}^{\text{II}}(\text{HCit})$ (R9 in Table 2) as well as to oxygen diffusivity, the sensitivity to the equilibrium constant E8: $\text{Fe}^{2+} + \text{HCit}^{2-} \rightleftharpoons \text{Fe}^{\text{II}}(\text{HCit})$ is significantly smaller and the model is basically insensitive to the equilibrium constant E5: $\text{Fe}^{3+} + \text{Cit}^{3-} \rightleftharpoons \text{Fe}^{\text{III}}(\text{Cit})$. In other words, this experiment alone allows to constrain R9 or oxygen diffusivity as long as the other parameter is known, but does not allow constraining the constants for the two equilibria.

640

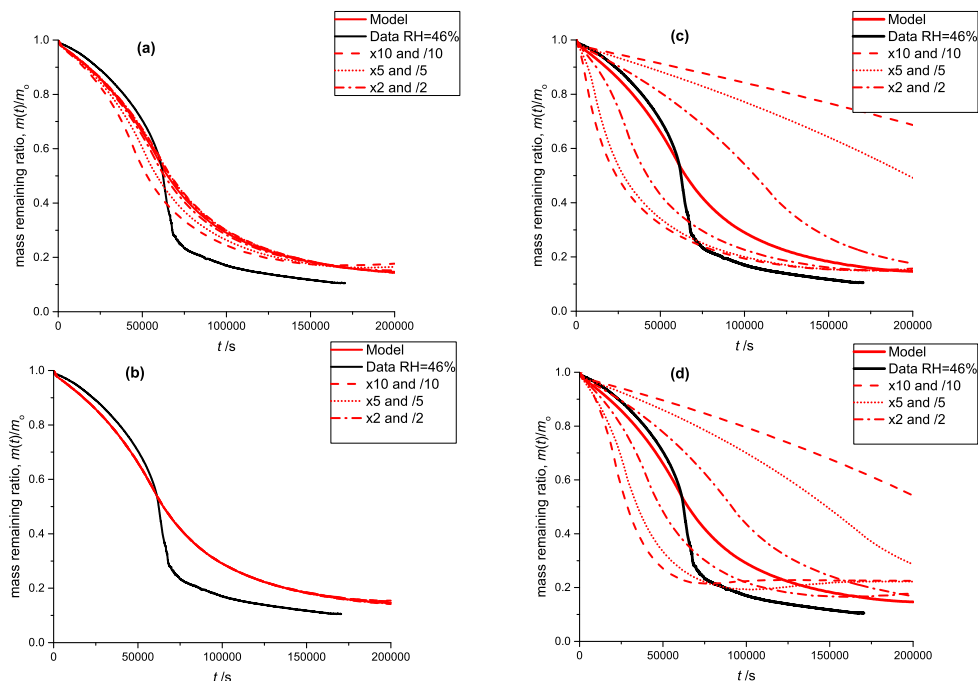


Figure A3. Black: mass remaining data versus time of the photo-degradation experiment discussed in section 3.1; RH 46 %. Red lines: model outputs obtained by varying a single parameter with factors: 10 and 0.1 (dashed), 5 and 0.2 (dotted), 2 and 0.5 (dash-dotted), 1 (solid). In panel (a) equilibrium constant of E8 is varied, in panel (b) equilibrium constant of E5 is varied, panel (c) shows the sensitivity to reaction constant R9 (see Table 2) and panel (d) the sensitivity to oxygen diffusivity (Table 1).

A6 The full EDB data set showing the *RH* effect on photocatalytic degradation efficiency

645 Figure 6 in the main text shows the photochemical degradation up to a mass remaining ratio of 0.6 and compares its temporal evolution with the PRAD model output. Here, we show in Fig. A4 for completeness the full experimental data set. Clearly seen is the shift to longer time scales with decreasing RH and that the PRAD model is no longer capable of capturing accurately the mass loss once about 20% of the initial mass is lost. However, we may conclude that even for mass remaining ratios lower than 0.5, the experimental data show a very significant shift of the degradation time scales with RH, but the total photochemical mass loss remains of the same order of magnitude, independent of RH.

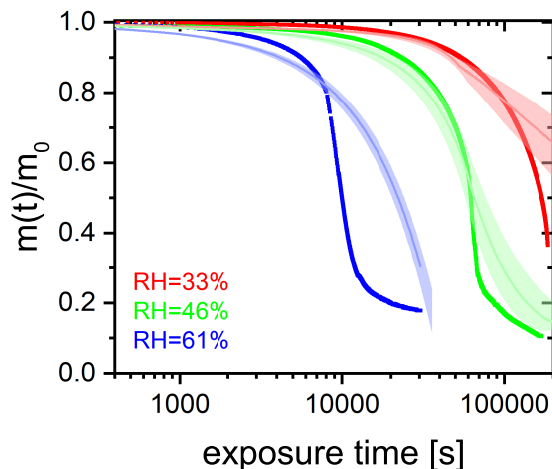


Figure A4. $\text{Fe}^{\text{III}}(\text{Cit})/\text{CA}$ (molar ratio 0.05) particle mass change with irradiation time (log scale) at different RH: 33 % (red), 46 % (green), and 61 % (blue). The irradiation wavelength was 375 nm, its intensity was 0.25 W cm^{-2} , and the experimental temperature was 293.5 K. Thick lines are EDB experimental data. Thin lines are PRAD model outputs (with ± 2 % RH uncertainty shown as shaded area).

Author contributions. J.D. wrote the manuscript. M.A. and U.K.K. conceptualized and planned the study. J.D. conducted EDB experiments, water activity measurements, and data analysis and interpretation supervised by U.K.K. P.A.A. planned and conducted STXM/NEXAFS experiments supervised by B.W. and M.A. J.D., P.C.A., J.X., T.H., C.N.B. and K.D.H. also conducted STXM/NEXAFS experiments. B.W., J.R. and P.A.A. conducted STXM/NEXAFS data analysis and interpretation. P.C.A. conducted CWFT experiments and data analysis and interpretation supervised by M.A. F.S. conducted viscosity experiments and data analysis and interpretation supervised by P.A.A. B.L. wrote and developed the PRAD model with the assistance of J.D. and P.A.A. H.H. advised on the photochemical reaction mechanisms. All co-authors discussed the results and commented on the manuscript.

Competing interests. The authors declare that they have no conflict of interest.

Acknowledgements. We thank Nir Bluvshstein for helpful discussions. We acknowledge funding by the Swiss National Science Foundation (grant no. 200021 163074/1). The PolLux end station was financed by the German Ministerium für Bildung und Forschung (BMBF) through contracts 05K16WED and 05K19WE2.

660 **References**

- Abel, B., Assmann, J., Buback, M., Grimm, C., Kling, M., Schmatz, S., Schroeder, J., and Witte, T.: Ultrafast decarboxylation of carbonyloxy radicals: Influence of molecular structure, *J. Phys. Chem. A*, 107, 9499–9510, <https://doi.org/10.1021/jp0350823>, 2003.
- Abida, O., Kolar, M., Jirkovsky, J., and Mailhot, G.: Degradation of 4-chlorophenol in aqueous solution photoinduced by Fe(III)–citrate complex, *Photochem. Photobiol. Sci.*, 11, 794–802, <https://doi.org/10.1039/c2pp05358f>, 2012.
- 665 Abrahamson, H. B., Rezvani, A. B., and Brushmiller, J.: Photochemical and spectroscopic studies of complexes, of iron(III) with citric acid and other carboxylic acids, *Inorganica Chimica Acta*, 226, 117–127, [https://doi.org/10.1016/0020-1693\(94\)04077-X](https://doi.org/10.1016/0020-1693(94)04077-X), 1994.
- Alpert, P. A., Corral Arroyo, P., Dou, J., Krieger, U. K., Steimer, S. S., Förster, J. D., Ditas, F., Pöhlker, C., Rossignol, S., Passananti, M., Perrier, S., George, C., Shiraiwa, M., Berkemeier, T., Watts, B., and Ammann, M.: Visualizing reaction and diffusion in xanthan gum aerosol particles exposed to ozone, *Phys. Chem. Chem. Phys.*, 21, 20613–20627, <https://doi.org/10.1039/c9cp03731d>, 2019.
- 670 Alpert, P. A., Dou, J., Corral Arroyo, P., Schneider, F., Xto, J., Luo, B., Peter, T., Huthwelker, T., Borca, C. N., Henzler, K. D., Herrmann, H., Raabe, J., Watts, B., Krieger, U. K., and Ammann, M.: ~~Anoxic aerosol particles leads to preserved radicals~~ **Photolytic radical persistence due to anoxia in viscous Aerosol particles**, in preparation for *Nature Nat. Commun.*, 2020, under review.
- Battino, R., Rettich, T. R., and Tominaga, T.: The Solubility of Oxygen and Ozone in Liquids, *Journal of Physical and Chemical Reference Data*, 12, 163–178, <https://doi.org/10.1063/1.555680>, <https://doi.org/10.1063/1.555680>, 1983.
- 675 Berkemeier, T., Steimer, S. S., Krieger, U. K., Peter, T., Pöschl, U., Ammann, M., and Shiraiwa, M.: Ozone uptake on glassy, semi-solid and liquid organic matter and the role of reactive oxygen intermediates in atmospheric aerosol chemistry, *Phys. Chem. Chem. Phys.*, 18, 12662–12674, <https://doi.org/10.1039/C6CP00634E>, 2016.
- Berkemeier, T., Ammann, M., Krieger, U. K., Peter, T., Spichtinger, P., Pöschl, U., Shiraiwa, M., and Huisman, A. J.: Technical note: Monte Carlo genetic algorithm (MCGA) for model analysis of multiphase chemical kinetics to determine transport and reaction rate coefficients using multiple experimental data sets, *Atmospheric Chemistry and Physics*, 17, 8021–8029, <https://doi.org/10.5194/acp-17-8021-2017>, <https://acp.copernicus.org/articles/17/8021/2017/>, 2017.
- Bianco, A., Passananti, M., Brigante, M., and Mailhot, G.: Photochemistry of the Cloud Aqueous Phase: A Review, *Molecules*, 25, 423, <https://doi.org/10.3390/molecules25020423>, 2020.
- Bielski, B. H. J., Cabelli, D. E., Arudi, R. L., and Ross, A. B.: Reactivity of HO₂/O₂⁻ radicals in aqueous solution, *J. Phys. Chem. Ref. Data*, 685 14, 1041–1100, <https://doi.org/10.1063/1.555739>, 1985.
- Bockman, T. M., Hubig, S. M., and Kochi, J. K.: Direct observation of ultrafast decarboxylation of acyloxy radicals via photoinduced electron transfer in carboxylate ion pairs, *J. Org. Chem.*, 62, 2210–2221, <https://doi.org/10.1021/JO9617833>, 1997.
- Brandt, C. and van Eldik, R.: Transition metal-catalyzed oxidation of sulfur(IV) oxides. Atmospheric-relevant processes and mechanisms, *Chem. Rev.*, 95, 119–190, <https://doi.org/10.1021/cr00033a006>, 1995.
- 690 Burden, R. L. and Faires, J. D.: *Numerical Analysis*, Brooks/Cole, Boston, MA, USA, ninth edn., 2011.
- Chebbi, A. and Carlier, P.: Carboxylic acids in the troposphere, occurrence, sources, and sinks: A review, *Atmos. Environ.*, 30, 4233–4249, [https://doi.org/10.1016/1352-2310\(96\)00102-1](https://doi.org/10.1016/1352-2310(96)00102-1), 1996.
- Christensen, H. and Sehested, K.: Pulse radiolysis at high temperatures and high pressures, *Radiat. Phys. Chem.*, 18, 723–731, [https://doi.org/10.1016/0146-5724\(81\)90195-3](https://doi.org/10.1016/0146-5724(81)90195-3), 1981.
- 695 Cieřla, P., Kocot, P., Mytych, P., and Stasicka, Z.: Homogeneous photocatalysis by transition metal complexes in the environment, *J. Mol. Catal. A-Chem.*, 224, 17–33, <https://doi.org/10.1016/j.molcata.2004.08.043>, 2004.

- Corral Arroyo, P., Bartels-Rausch, T., Alpert, P. A., Dumas, S., Perrier, S., George, C., and Ammann, M.: Particle-phase photosensitized radical production and aerosol aging, *Environ. Sci. Technol.*, 52, 7680–7688, <https://doi.org/10.1021/acs.est.8b00329>, 2018.
- Davis, E. J., Buehler, M. F., and Ward, T. L.: The double-ring electrodynamic balance for microparticle characterization, *Rev. Sci. Instrum.*, 61, 1281–1288, <https://doi.org/10.1063/1.1141227>, 1990.
- 700
- Deguillaume, L., Leriche, M., Desboeufs, K., Mailhot, G., George, C., and Chaumerliac, N.: Transition metals in atmospheric liquid phases: Sources, reactivity, and sensitive parameters, *Chem. Rev.*, 105, 3388–3431, <https://doi.org/10.1021/cr040649c>, 2005.
- Dou, J., Lin, P., Kuang, B. Y., and Yu, J. Z.: Reactive oxygen species production mediated by humic-like substances in atmospheric aerosols: Enhancement effects by pyridine, imidazole, and their derivatives, *Environ. Sci. Technol.*, 49, 6457–6465, <https://doi.org/10.1021/es5059378>, 2015.
- 705
- Dou, J., Luo, B., Peter, T., Alpert, P. A., Corral Arroyo, P., Ammann, M., and Krieger, U. K.: Carbon dioxide diffusivity in single, levitated organic aerosol particles, *J. Phys. Chem. Lett.*, 10, 4484–4489, <https://doi.org/10.1021/acs.jpcclett.9b01389>, 2019.
- Faust, B. C. and Hoigné, J.: Photolysis of Fe(III)-hydroxy complexes as sources of OH radicals in clouds, fog and rain, *Atmospheric Environment. Part A. General Topics*, 24, 79–89, [https://doi.org/10.1016/0960-1686\(90\)90443-Q](https://doi.org/10.1016/0960-1686(90)90443-Q), 1990.
- 710
- Faust, B. C. and Zepp, R. G.: Photochemistry of aqueous iron(III)-polycarboxylate complexes: roles in the chemistry of atmospheric and surface waters, *Environ. Sci. Technol.*, 27, 2517–2522, <https://doi.org/10.1021/es00048a032>, 1993.
- Feng, W., Nansheng, D., Glebov, E. M., Pozdnyakov, I. P., Grivin, V. P., Plyusnin, V. F., and Bazhin, N. M.: Kinetics and mechanism of photolysis of the iron(III) complex with tartaric acid, *Russ. Chem. Bull.*, 56, 900–903, <https://doi.org/10.1007/s11172-007-0136-7>, 2007.
- Fenton, H. J. H.: LXXIII.—Oxidation of tartaric acid in presence of iron, *J. Chem. Soc., Trans.*, 65, 899–910, <https://doi.org/10.1039/CT8946500899>, 1894.
- 715
- Flechsig, U., Quitmann, C., Raabe, J., Böge, M., Fink, R., and Ade, H.: The PolLux Microspectroscopy Beam line at the Swiss Light Source, *AIP Conference Proceedings*, 879, 505–508, <https://doi.org/10.1063/1.2436109>, 2007.
- Fogg, P. G. T., ed.: *Carbon Dioxide in Non-Aqueous Solvents At Pressures Less Than 200 KPa*, vol. 50, Pergamon Press, Oxford, <https://doi.org/10.1016/C2009-0-00247-5>, 1992.
- 720
- Frommherz, U., Raabe, J., Watts, B., Stefani, R., Ellenberger, U., Garrett, R., Gentle, I., Nugent, K., and Wilkins, S.: Higher Order Suppressor (HOS) for the PolLux Microspectroscopy Beamline at the Swiss Light Source SLS, *AIP Conference Proceedings*, 1234, 429–432, <https://doi.org/10.1063/1.3463232>, 2010.
- Garvie, L. A., Craven, A. J., and Brydson, R.: Use of electron-energy loss near-edge fine structure in the study of minerals, *American Mineralogist*, 79, 411–425, 1994.
- 725
- George, C., D’Anna, B., Herrmann, H., Weller, C., Vaida, V., Donaldson, D. J., Bartels-Rausch, T., and Ammann, M.: Emerging areas in atmospheric photochemistry, in: *Topics in Current Chemistry*, vol. 339, pp. 1–53, Springer, Berlin, Heidelberg, https://doi.org/10.1007/128_2012_393, 2012.
- George, C., Ammann, M., D’Anna, B., Donaldson, D. J., and Nizkorodov, S. A.: Heterogeneous photochemistry in the atmosphere, *Chem. Rev.*, 115, 4218–4258, <https://doi.org/10.1021/cr500648z>, 2015.
- 730
- Glebov, E. M., Pozdnyakov, I. P., Grivin, V. P., Plyusnin, V. F., Zhang, X., Wu, F., and Deng, N.: Intermediates in photochemistry of Fe(III) complexes with carboxylic acids in aqueous solutions, *Photochem. Photobiol. Sci.*, 10, 425–430, <https://doi.org/10.1039/C0PP00151A>, 2011.

- Gonzalez, D. H., Cala, C. K., Peng, Q., and Paulson, S. E.: HULIS enhancement of hydroxyl radical formation from Fe(II): kinetics of fulvic acid-Fe(II) complexes in the presence of lung antioxidants, *Environ. Sci. Technol.*, 51, 7676–7685, <https://doi.org/10.1021/acs.est.7b01299>, 2017.
- 735 González Palacios, L., Corral Arroyo, P., Aregahegn, K. Z., Steimer, S. S., Bartels-Rausch, T., Nozière, B., George, C., Ammann, M., and Volkamer, R.: Heterogeneous photochemistry of imidazole-2-carboxaldehyde: HO₂ radical formation and aerosol growth, *Atmos. Chem. Phys.*, 16, 11 823–11 836, <https://doi.org/10.5194/acp-16-11823-2016>, 2016.
- Grgič, I.: *Metals in Aerosols*, chap. 5, pp. 117–139, John Wiley & Sons, Ltd, <https://doi.org/10.1002/9781444305388.ch5>, 2009.
- 740 Grgič, I., Dovžan, A., Berčič, G., and Hudnik, V.: The effect of atmospheric organic compounds on the Fe-catalyzed S(IV) autoxidation in aqueous solution, *J. Atmos. Chem.*, 29, 315–337, <https://doi.org/10.1023/A:1005918912994>, 1998.
- Grgič, I., Poznič, M., and Bizjak, M.: S(IV) autoxidation in atmospheric liquid water: The role of Fe(II) and the effect of oxalate, *J. Atmos. Chem.*, 33, 89–102, <https://doi.org/10.1023/A:1006141913681>, 1999.
- Hamilton, D. S., Scanza, R. A., Feng, Y., Guinness, J., Kok, J. F., Li, L., Liu, X., Rathod, S. D., Wan, J. S., Wu, M., and Mahowald, N. M.: Improved methodologies for Earth system modelling of atmospheric soluble iron and observation comparisons using the Mechanism of Intermediate complexity for Modelling Iron (MIMI v1.0), *Geosci. Model Dev.*, 12, 383–3862, <https://doi.org/10.5194/gmd-12-3835-2019>, 2019.
- 745 Herrmann, H., Schaefer, T., Tilgner, A., Styler, S. A., Weller, C., Teich, M., and Otto, T.: Tropospheric Aqueous-Phase Chemistry: Kinetics, Mechanisms, and Its Coupling to a Changing Gas Phase, *Chem. Rev.*, 115, 4259–4334, <https://doi.org/10.1021/cr500447k>, 2015.
- 750 Hilborn, J. W. and Pincock, J. A.: Rates of decarboxylation of acyloxy radicals formed in the photocleavage of substituted 1-naphthylmethyl alkanooates, *J. Am. Chem. Soc.*, 113, 2683–2686, <https://doi.org/10.1021/ja00007a049>, 1991.
- Hofmann, H., Hoffmann, P., and Lieser, K. H.: Transition metals in atmospheric aqueous samples, analytical determination and speciation, *Fresenius J. Anal. Chem.*, 340, 591–597, <https://doi.org/10.1007/BF00322435>, 1991.
- Houle, F. A., Hinsberg, W. D., and Wilson, K. R.: Oxidation of a model alkane aerosol by OH radical: the emergent nature of reactive uptake, *Phys. Chem. Chem. Phys.*, 17, 4412–4423, <https://doi.org/10.1039/C4CP05093B>, 2015.
- 755 Hug, S. J., Canonica, L., Wegelin, M., Gechter, D., and von Gunten, U.: Solar oxidation and removal of arsenic at circumneutral pH in iron containing waters, *Environ. Sci. Technol.*, 35, 2114–2121, <https://doi.org/10.1021/es001551s>, 2001.
- Huthwelker, T., Zelenay, V., Birrer, M., Krepelova, A., Raabe, J., Tzvetkov, G., Vernooij, M. G., and Ammann, M.: An in situ cell to study phase transitions in individual aerosol particles on a substrate using scanning transmission x-ray microspectroscopy, *Rev. Sci. Instrum.*, 81, 113 706, <https://doi.org/10.1063/1.3494604>, 2010.
- 760 Kahnt, A., Iinuma, Y., Blockhuys, F., Mutzel, A., Vermeylen, R., Kleindienst, T. E., Jaoui, M., Offenberg, J. H., Lewandowski, M., Böge, O., Herrmann, H., Maenhaut, W., and Claeys, M.: 2-Hydroxyterpenylic acid: An oxygenated marker compound for α -pinene secondary organic aerosol in ambient fine aerosol, *Environ. Sci. Technol.*, 48, 4901–4908, <https://doi.org/10.1021/es500377d>, 2014.
- Kanakidou, M., Myriokefalitakis, S., and Tsigaridis, K.: Aerosols in atmospheric chemistry and biogeochemical cycles of nutrients, *Environ. Res. Lett.*, 13, 063 004, <https://doi.org/10.1088/1748-9326/aabddb>, 2018.
- 765 Kawamura, K., Ng, L. L., and Kaplan, I. R.: Determination of organic acids (C₁–C₁₀) in the atmosphere, motor exhausts, and engine oils, *Environ. Sci. Technol.*, 19, 1082–1086, <https://doi.org/10.1021/es00141a010>, 1985.
- Kieber, R. J., Hardison, D. R., Whitehead, R. F., and Willey, J. D.: Photochemical production of Fe(II) in rainwater, *Environ. Sci. Technol.*, 37, 4610–4616, <https://doi.org/10.1021/es030345s>, 2003.

- 770 Kieber, R. J., Skrabal, S. A., Smith, B. J., and Willey, J. D.: Organic complexation of Fe(II) and its impact on the redox cycling of iron in rain, *Environ. Sci. Technol.*, 39, 1576–1583, <https://doi.org/10.1021/es040439h>, 2005.
- Koop, T., Bookhold, J., Shiraiwa, M., and Pöschl, U.: Glass transition and phase state of organic compounds: dependency on molecular properties and implications for secondary organic aerosols in the atmosphere, *Phys. Chem. Chem. Phys.*, 13, 19238–19255, <https://doi.org/10.1039/c1cp22617g>, 2011.
- 775 Lienhard, D. M., Bones, D. L., Zuend, A., Krieger, U. K., Reid, J. P., and Peter, T.: Measurements of thermodynamic and optical properties of selected aqueous organic and organic-inorganic mixtures of atmospheric relevance, *J. Phys. Chem. A*, 116, 9954–9968, <https://doi.org/10.1021/jp3055872>, 2012.
- Lienhard, D. M., Huisman, A. J., Bones, D. L., Te, Y.-F., Luo, B. P., Krieger, U. K., and Reid, J. P.: Retrieving the translational diffusion coefficient of water from experiments on single levitated aerosol droplets, *Phys. Chem. Chem. Phys.*, 16, 16677–16683, <https://doi.org/10.1039/C4CP01939C>, 2014.
- 780 Madronich, S., McKenzie, R. L., Caldwell, M., and Björn, L. O.: Changes in ultraviolet-radiation reaching the earth's surface, *Ambio*, 24, 143–152, <http://lup.lub.lu.se/record/134508>, 1995.
- Martell, A. E. and Smith, R. M.: *Critical stability constants*, vol. 5, Springer US, Boston, MA, USA, 1982.
- Moffet, R. C., Furutani, H., Rödel, T. C., Henn, T. R., Sprau, P. O., Laskin, A., Uematsu, M., and Gilles, M. K.: Iron speciation and mixing in single aerosol particles from the Asian continental outflow, *J. Geophys. Res.*, 117, D07204, <https://doi.org/10.1029/2011JD016746>, 2012.
- 785 Okochi, H. and Brimblecombe, P.: Potential trace metal–organic complexation in the atmosphere, *The Scientific World JOURNAL*, 2, 767–786, <https://doi.org/10.1100/tsw.2002.132>, 2002.
- Pöschl, U., Rudich, Y., and Ammann, M.: Kinetic model framework for aerosol and cloud surface chemistry and gas-particle interactions - Part 1: General equations, parameters, and terminology, *Atmospheric Chemistry and Physics*, 7, 5989–6023, <https://doi.org/10.5194/acp-7-5989-2007>, <https://acp.copernicus.org/articles/7/5989/2007/>, 2007.
- 790 Pozdnyakov, I. P., Kel, O. V., Plyusnin, V. F., Grivin, V. P., and Bazhin, N. M.: New insight into photochemistry of ferrioxalate, *J. Phys. Chem. A*, 112, 8316–8322, <https://doi.org/10.1021/jp8040583>, 2008.
- Pozdnyakov, I. P., Glebov, E. M., Plyusnin, V. F., Grivin, V. P., Bunduki, E., Goryacheva, N. V., Gladki, V., and Duka, G. G.: Photochemistry of Fe(III) complex with glyoxalic acid in aqueous solution, *High Energy Chemistry*, 43, 406–409, <https://doi.org/10.1134/S0018143909050129>, 2009.
- 795 Pozdnyakov, I. P., Kolomeets, A. V., Plyusnin, V. F., Melnikov, A. A., Kompanets, V. O., Chekalin, S. V., Tkachenko, N., and Lemmetynen, H.: Photophysics of Fe(III)–tartrate and Fe(III)–citrate complexes in aqueous solutions, *Chemical Physics Letters*, 530, 45–48, <https://doi.org/10.1016/j.cplett.2012.01.051>, 2012.
- Pruppacher, H. and Klett, J.: Microstructure of atmospheric clouds and precipitation, in: *Microphysics of Clouds and Precipitation*, vol. 18, pp. 10–73, Springer Netherlands, Dordrecht, https://doi.org/10.1007/978-0-306-48100-0_2, 2010.
- 800 Raabe, J., Tzvetkov, G., Flechsig, U., Böge, M., Jaggi, A., Sarafimov, B., Vernooij, M. G., Huthwelker, T., Ade, H., Kilcoyne, D., Tylliszczak, T., Fink, R. H., and Quitmann, C.: PolLux: A new facility for soft x-ray spectromicroscopy at the Swiss light source, *Rev. Sci. Instrum.*, 79, 113704, <https://doi.org/10.1063/1.3021472>, 2008.
- Rush, J. D. and Bielski, B. H. J.: Pulse radiolytic studies of the reaction of HO_2/O_2^- with Fe(II)/Fe(III) ions. The reactivity of HO_2/O_2^- with ferric ions and its implication on the occurrence of the Haber-Weiss reaction, *J. Phys. Chem.*, 89, 5062–5066, <https://doi.org/10.1021/j100269a035>, 1985.
- 805

- Sander, R.: Compilation of Henry's law constants (version 4.0) for water as solvent, *Atmos. Chem. Phys.*, 15, 4399–4981, <https://doi.org/10.5194/acp-15-4399-2015>, 2015.
- Shiraiwa, M. and Seinfeld, J. H.: Equilibration timescale of atmospheric secondary organic aerosol partitioning, *Geophys. Res. Lett.*, 39, L24 801, <https://doi.org/10.1029/2012GL054008>, 2012.
- Shiraiwa, M., Ammann, M., Koop, T., and Poschl, U.: Gas uptake and chemical aging of semisolid organic aerosol particles, *Proc. Natl. Acad. Sci.*, 108, 11 003–11 008, <https://doi.org/10.1073/pnas.1103045108>, 2011.
- Shiraiwa, M., Pfrang, C., Koop, T., and Pöschl, U.: Kinetic multi-layer model of gas-particle interactions in aerosols and clouds (KM-GAP): linking condensation, evaporation and chemical reactions of organics, oxidants and water, *Atmospheric Chemistry and Physics*, 12, 2777–2794, <https://doi.org/10.5194/acp-12-2777-2012>, <https://acp.copernicus.org/articles/12/2777/2012/>, 2012.
- Smith, R. M. and Martell, A. E.: *Critical Stability Constants*, vol. 4, Springer US, Boston, MA, USA, <https://doi.org/10.1007/978-1-4757-5506-0>, 1976.
- Song, Y. C., Haddrell, A. E., Bzdek, B. R., Reid, J. P., Bannan, T., Topping, D. O., Percival, C., and Cai, C.: Measurements and predictions of binary component aerosol particle viscosity, *J. Phys. Chem. A*, 120, 8123–8137, <https://doi.org/10.1021/acs.jpca.6b07835>, 2016.
- Steimer, S. S., Lampimäki, M., Coz, E., Grzanic, G., and Ammann, M.: The influence of physical state on shikimic acid ozonolysis: a case for in situ microspectroscopy, *Atmos. Chem. Phys.*, 14, 10 761–10 772, <https://doi.org/10.5194/acp-14-10761-2014>, 2014.
- Steimer, S. S., Berkemeier, T., Gilgen, A., Krieger, U. K., Peter, T., Shiraiwa, M., and Ammann, M.: Shikimic acid ozonolysis kinetics of the transition from liquid aqueous solution to highly viscous glass, *Phys. Chem. Chem. Phys.*, 17, 31 101–31 109, <https://doi.org/10.1039/C5CP04544D>, 2015a.
- Steimer, S. S., Krieger, U. K., Te, Y. F., Lienhard, D. M., Huisman, A. J., Luo, B. P., Ammann, M., and Peter, T.: Electrodynamic balance measurements of thermodynamic, kinetic, and optical aerosol properties inaccessible to bulk methods, *Atmos. Meas. Tech.*, 8, 2397–2408, <https://doi.org/10.5194/amt-8-2397-2015>, 2015b.
- Tao, Y. and Murphy, J. G.: The Mechanisms Responsible for the Interactions among Oxalate, pH, and Fe Dissolution in PM_{2.5}, *ACS Earth Space Chem.*, 3, 2259–2265, <https://doi.org/10.1021/acsearthspacechem.9b00172>, 2019.
- Tapparo, A., Di Marco, V., Badocco, D., D'Aronco, S., Soldà, L., Pastore, P., Mahon, B. M., Kalberer, M., and Giorio, C.: Formation of metal-organic ligand complexes affects solubility of metals in airborne particles at an urban site in the Po valley, *Chemosphere*, 241, 125 025, <https://doi.org/10.1016/j.chemosphere.2019.125025>, 2020.
- von Sonntag, C. and Schuchmann, H.-P.: Aufklärung von Peroxyl-Radikalreaktionen in wäßriger Lösung mit strahlenchemischen Techniken, *Angew. Chem.*, 103, 1255–1279, <https://doi.org/10.1002/ange.19911031006>, 1991.
- Walling, C.: Fenton's reagent revisited, *Acc. Chem. Res.*, 8, 125–131, <https://doi.org/10.1021/ar50088a003>, 1975.
- Wang, Z., Chen, C., Ma, W., and Zhao, J.: Photochemical coupling of iron redox reactions and transformation of low-molecular-weight organic matter, *J. Phys. Chem. Lett.*, 3, 2044–2051, <https://doi.org/10.1021/jz3005333>, 2012.
- Weller, C., Horn, S., and Herrmann, H.: Photolysis of Fe(III) carboxylato complexes: Fe(II) quantum yields and reaction mechanisms, *J. Photochem. Photobiol. A Chem.*, 268, 24–36, <https://doi.org/10.1016/j.jphotochem.2013.06.022>, 2013.
- Weller, C., Tilgner, A., Bräuer, P., and Herrmann, H.: Modeling the impact of iron-carboxylate photochemistry on radical budget and carboxylate degradation in cloud droplets and particles, *Environ. Sci. Technol.*, 48, 5652–5659, <https://doi.org/10.1021/es4056643>, 2014.
- Weschler, C. J., Mandich, M. L., and Graedel, T. E.: Speciation, photosensitivity, and reactions of transition metal ions in atmospheric droplets, *J. Geophys. Res.*, 91, 5189, <https://doi.org/10.1029/JD091iD04p05189>, 1986.

- 845 Willey, J. D., Kieber, R. J., Williams, K. H., Crozier, J. S., Skrabal, S. A., and Avery, G. B.: Temporal variability of iron speciation in coastal rainwater, *J. Atmos. Chem.*, 37, 185–205, <https://doi.org/10.1023/A:1006421624865>, 2000.
- Zardini, A. A., Krieger, U. K., and Marcolli, C.: White light Mie resonance spectroscopy used to measure very low vapor pressures of substances in aqueous solution aerosol particles, *Optics Express*, 14, 6951–6962, <https://doi.org/10.1364/OE.14.006951>, 2006.
- 850 Zaveri, R. A., Shaw, W. J., Cziczo, D. J., Schmid, B., Ferrare, R. A., Alexander, M. L., Alexandrov, M., Alvarez, R. J., Arnott, W. P., Atkinson, D. B., Baidar, S., Banta, R. M., Barnard, J. C., Beranek, J., Berg, L. K., Brechtel, F., Brewer, W. A., Cahill, J. F., Cairns, B., Cappa, C. D., Chand, D., China, S., Comstock, J. M., Dubey, M. K., Easter, R. C., Erickson, M. H., Fast, J. D., Floerchinger, C., Flowers, B. A., Fortner, E., Gaffney, J. S., Gilles, M. K., Gorkowski, K., Gustafson, W. I., Gyawali, M., Hair, J., Hardesty, R. M., Harworth, J. W., Herndon, S., Hiranuma, N., Hostetler, C., Hubbe, J. M., Jayne, J. T., Jeong, H., Jobson, B. T., Kassianov, E. I., Kleinman, L. I., Kluzek, C., Knighton, B., Kolesar, K. R., Kuang, C., Kubátová, A., Langford, A. O., Laskin, A., Laulainen, N., Marchbanks, R. D., Mazzoleni, C., Mei, F., Moffet, R. C., Nelson, D., Obland, M. D., Oetjen, H., Onasch, T. B., Ortega, I., Ottaviani, M., Pekour, M., Prather, K. A., Radney, J. G., 855 Rogers, R. R., Sandberg, S. P., Sedlacek, A., Senff, C. J., Senum, G., Setyan, A., Shilling, J. E., Shrivastava, M., Song, C., Springston, S. R., Subramanian, R., Suski, K., Tomlinson, J., Volkamer, R., Wallace, H. W., Wang, J., Weickmann, A. M., Worsnop, D. R., Yu, X.-Y., Zelenyuk, A., and Zhang, Q.: Overview of the 2010 Carbonaceous Aerosols and Radiative Effects Study (CARES), *Atmos. Chem. Phys.*, 12, 7647–7687, <https://doi.org/10.5194/acp-12-7647-2012>, 2012.
- 860 Zhang, X., Gong, Y., Wu, F., Deng, N., Pozdnyakov, I. P., Glebov, E. M., Grivin, V. P., Plyusnin, V. F., and Bazhinb, N. M.: Photochemistry of the iron(III) complex with pyruvic acid in aqueous solutions, *Russ. Chem. Bull*, 58, 1828–1836, <https://doi.org/10.1007/s11172-009-0249-2>, 2009.